MINISTRY OF EDUCATION   VIETNAM ACADEMY OF SCIENCE

AND TRAINING   AND TECHNOLOGY

GRADUATION UNIVERSITY OF SCIENCE AND TECHNOLOGY
————————o0o————————

Tran Van Ngoc

TESTING CP AND CPT INVARIANCES WITH NEUTRINO OSCILLATION MEASUREMENTS IN T2K EXPERIMENT

Doctor of Philosophy Dissertation in Physics

Hanoi, 2023

Tran Van Ngoc

TESTING CP AND CPT INVARIANCES WITH NEUTRINO OSCILLATION MEASUREMENTS IN T2K EXPERIMENT

Major: **Mathematical Physics and Theoretical Physics**

Code: **9440103**

Doctor of Philosophy Dissertation in Physics

Supervisor 1: **Assoc. Prof. Nguyen Thi Hong Van**

Supervisor 2: **Prof. Tsuyoshi Nakaya**

Hanoi, 2023

Declaration of Authorship

I hereby declare that the thesis titled "Testing CP and CPT invariances with neutrino oscillation measurements in T2K experiment" and the work presented in it are my own. I confirm that this work does not contain my previous work as well as other people's work without being clearly stated. The bibliography contains all the references that I used in writing the thesis.

I declare that this is a true copy of my thesis, which is approved by my thesis supervisors, and that this thesis has not been submitted for a doctoral degree to any other university or institution.

I certify that any republication of materials presented in this thesis has been approved by the relevant publishers and coauthors.

Signature of the Author

Tran Van Ngoc

Acknowledgements

Abstract

CP and CPT are among the most fundamental symmetries of Nature. Testing CP and CPT invariances is of prime importance for fundamental physics. T2K is a long-baseline neutrino oscillation experiment. It uses an intense muon neutrino (antineutrino) beam to study neutrino oscillation phenomenon. By operating in both neutrino mode and antineutrino mode, T2K is able to test CP symmetry in lepton sector. In addition, the disappearance channels of muon neutrino and antineutrino at long-baseline experiments such as T2K are the "golden channels" to test CPT invariance.

The on-axis near detector INGRID provides information about neutrino event rate and beam profile. The measurements at INGRID are in good agreement with MC predictions. The neutrino event rate and beam profile are stable within the physics requirements in T2K run 10.

Testing CP and CPT symmetries with T2K and with a combined analysis of T2K-II, NOνA extension, and JUNO experiments are presented. T2K ruled out CP conserving values ($\delta_{CP} = 0$; π) at more than 95% C. L. using data collected from run 1 to run 9 with a total exposure of 3.13×10^{21} POT. The value of CP violating phase (δ_{CP}) was measured to be $-2.14^{+0.90}_{-0.69}$ for normal mass ordering (NO) and $-1.26^{+0.61}_{-0.69}$ for inverted mass ordering (IO). With constraint from short baseline reactor experiments, the best fit values of δ_{CP} with $\pm 1\sigma$ uncertainties are $-1.89^{+0.70}_{-0.58}$ for NO and $-1.38^{+0.48}_{-0.55}$ for IO. We also show that by 2028, the joint fit of T2K-II, NOνA extension, and JUNO will be able to exclude CP conservation at $\sim 5\sigma$ C. L.

The analysis of the T2K data with 3.13×10^{21} POT exposure is consistent with CPT conservation hypothesis. The joint analysis of T2K-II, NOνA extension, and JUNO will be able to exclude CPT conservation at 1.7σ (4σ) and 3σ (4.6σ) C. L. if the best-fit values of T2K (NOνA) in the mass squared splittings (Δm^2_{31}, $\Delta \overline{m}^2_{31}$) and mixing angles ($\theta_{23}$, $\overline{\theta}_{23}$) are presumed to be true values. In addition, the synergy can improve the bound on $|\Delta m^2_{31} - \Delta \overline{m}^2_{31}|$ to the world's best value ever made, $5.3 \times 10^{-5} eV^2$ at 3σ C. L., which is slightly better than DUNE and about one order of magnitude better than the value analysed by current neutrino oscillation experiments.

Contents

List of Abbreviations

AEDL Abstract Experiment Definition Language

AGS Alternating Gradient Synchrotron

CC charged current

DIS deep inelastic scattering

DONUT Direct observation of the nu tau, E872

GeV giga-electron-volt

INGRID Interactive Neutrino GRID

J-PARC Japan Proton Accelerator Research Complex

JUNO Jiangmen Underground Neutrino Observatory

GLoBES General Long Baseline Experiment Simulator

MPPC Multi-Pixel Photon Counter

MSW Mikheyev–Smirnov–Wolfenstein

MRD muon range detector

NC neutral current

NOvA NuMI Off-axis ν_e Appearance

PCAC partially conserved axial vector current

PMNS Pontecorvo–Maki–Nakagawa–Sakata

PMT Photo-Multiplier Tube

QED Quantum Electrodynamics

QCD Quantum Chromodynamics

SM Standard Model

T2K Tokai to Kamioka

WAGASCI BabyMIND WAter Grid SCIntillator Detector – prototype Magnetized Iron Neutrino Detector

List of Tables

List of Figures

Introduction

From ancient times to the present, symmetry has played a crucial role, being considered as one of the most important factors in judging beauty. For human beings, the harmony and balance of a body, an object, or an architectural structure lie behind the standard of beauty. In mathematics, a geometric shape or an object is said to be symmetric if it is invariant under a specific group of transformations such as translation, reflection, or rotation. Although symmetry underpins conservation laws in physics, its importance was not recognized until the early 20th century. It was Emmy Noether who first apparently pointed out in 1918 the profound connection between the continuous symmetries of a physics system and conservation laws. In the later part of the 20th century, with the developments of quantum mechanics and field theory, symmetry emerged as one of the most important concepts in physics. Its role is like a lighthouse, guiding scientists in searching for the fundamental laws of nature.

"I do not know what I may appear to the world, but to myself I seem to have been only like a boy playing on the seashore, and diverting myself in now and then finding a smoother pebble or a prettier shell than ordinary, whilst the great ocean of truth lay all undiscovered before me". The humble quote of Newton well describes our knowledge before the vastness of the universe. Nature has its own intriguing beauty that will always be mysterious to us. Throughout its history, humanity has been "like a boy playing on the seashore" of the universe, trying to find some "smooth pebbles and pretty shells" before "the undiscovered ocean of truth". Among those secrets, the asymmetry between matter and antimatter is one of the biggest puzzles waiting for humanity to discover. Once again, symmetry is placed at the center of that journey. And this time, the historical role is entrusted to discrete symmetry. Discrete symmetries, including charge conjugation C, parity inversion P, and time reversal T play a vital role in particle physics. Their conservation or violation, individual or in combination, may be the key to unveil the secrets of the universe. For a long time, one has believed that C, P, and T and their combinations are conserved in physics processes. Developments in theory and experiment in the last 66 years, however, have gradually proved the opposition. Parity violation was theoretically predicted by Tsung Dao Lee and Chen Ning Yang in 1956 [13], then experimentally confirmed by Chien Shiung Wu *et. al.* [14] one year later, resulting in the formation of the V-A structure in weak interaction. Next, CP violation in the quark sector was experimentally found in the neutral kaon system in 1964 [15], in B-meson decay at the BaBar experiment [16], and the Belle experiment [17] in 2001. Recently, the long baseline neutrino oscillation experiment T2K has announced an indication of CP violation in the lepton sector by ruling out a large amount of CP-violating phase δ_{CP} at 3σ C. L. [18]. Searching for CP violation in the lepton sector is one of the most important goals of the current and future neutrino oscillation experiments.

Most of the models in modern physics are based on the framework of quantum field theory. CPT is a fundamental symmetry in quantum field theory. Once the symmetry is tested, it consequently tests the fundamental physics also. If CPT symmetry is proved to be not conserved, the impact on the fundamental physics is therefore enormous: at least one of the three assumptions of the quantum field theories must be abandoned: (1) Lorentz invariance, (2) locality or (3) hermiticity of Hamiltonian. In addition, the CPT combination contains the charge conjugation operator C, which transforms particles into antiparticles and vice versa. Therefore, CPT violation can be a candidate to explain matter-antimatter asymmetry of the universe [19]. The CPT symmetry has been tested by different types of experiments with different methods. The Standard Model Extension provides a formalism to test CPT by measuring and deriving the Lorentz and CPT violating coefficients [20], [21], [22]. Ref. [23] summarizes the latest results on Lorentz and CPT violation searches in the context of Standard Model Extension. The CPT can also be tested based on the consequences of CPT theorem which says that the particle and its antiparticle must have the same energy spectra, implying identical mass and lifetime, and opposite in charge and magnetic (electric) dipole moment [24]. Testing CPT invariance by comparing the masses, charges, magnetic moments, and hyperfine spectroscopy has been done on several systems of particle and its antiparticle [25], [12]. The measurement on neutral kaon system has provided the best limit on the CPT violation so far [12]. In terms of mass squared difference, the bound reads $|m^2(K^\circ) - m^2(\overline{K}^\circ)| < 0.3 \ eV^2$. Comparing this to the two mass-squared differences of the three neutrino mass eigenstates [12], $m_{\nu 2}^2 - m_{\nu 1}^2 \approx 7.39 \times 10^{-5} \ \text{eV}^2$ and $|m_{\nu 3}^2 - m_{\nu 2}^2| \approx 2.45 \times 10^{-3} \ \text{eV}^2$, it becomes clear that neutrino measurements, rather than neutral kaons, provide the best constraint on the CPT test in terms of the mass-squared difference [26,27]. The aforementioned neutrino mass-squared differences come from measurements in neutrino oscillation. Therefore, testing CPT with neutrino oscillation has recently become of interest in the physics community.

The purpose of this thesis is to investigate the current status and future prospects of testing the CP and CPT invariances from neutrino oscillation experiments. In which we focus on the analysis of recent T2K data and the sensitivity with the synergy of T2K-II, NOvA extension (denoted as NOvA-II from now on), and JUNO experiments. In addition to the introduction and conclusion sections, the thesis consists of three chapters and is organized as follows. In Chapter 1, we introduce a general overview of neutrino oscillation phenomenon and relevant experiments. Chapter 2 presents basic results on neutrino flux and beam profile at T2K near detector INGRID which we had directly done the measurement and simulation during the time at J-PARC in 2019. Recently, we have also involved in measuring neutrino interactions at WAGASCI Baby-MIND which preliminary result is shown in the Appendix A. The subject of Chapter 3 is about CP and CPT testing in the T2K and with the joint fit of the T2K-II, NOvA-II, and JUNO experiments.

Chapter 1. Neutrino oscillation phenomenon and experiments

1.1 Neutrino oscillation

Neutrino oscillation is a quantum mechanical phenomenon in which one type of neutrino "oscillates" or transforms into another type during propagation in space-time. The first idea was suggested by B. Pontecorvo in 1957, describing the neutrino-antineutrino transition [28]. In 1962, Z. Maki, M. Nakagawa and S. Sakata developed the Pontecorvo's idea to describe flavor oscillation [29]. Neutrino oscillation theory can explain the solar neutrino anomaly [30], [31] and the atmospheric neutrino anomaly [32]. The phenomenon was observed for the first time by the Super-Kamiokande experiment [33], SNO experiment [34] and later by many other neutrino experiments. The discovery of neutrino oscillation indicates that neutrinos must have masses. This is the only experimental evidence for the physics beyond Standard Model (SM) of elementary particles so far, because in SM, neutrinos are massless. In this section, we will briefly introduce the history of neutrinos, how neutrinos are described in SM and the neutrino oscillation phenomenon.

1.1.1 Neutrino history

The study of beta decay in the early 20th century provided the first indirect evidence of the existence of neutrinos. In the 1920s, the spectra of alpha and gamma decays were apparently known to be mono-energetic or discrete. The physicists at first expected that beta decay would have similar behavior to alpha and gamma decays because they only detected two particles in the final state

$$X_Z^A \to Y_{Z-1}^A + e^-. \tag{1.1}$$

The electron kinetic energy was expected to be mono-energetic $K_e = (m_X - m_Y - m_e)c^2$. A series of studies carried out by Lise Meitner and Otto Hahn in 1911 and Jean Danysz in 1913, however, pointed out that the beta spectrum is continuous. Moreover, the energy spectral of emitted beta particles was observed to be smaller than predicted by the law of energy conservation. This fact made scientists confused. More and more evidence on the long tail spectrum of the beta decay even led some of them, including Niels Bohr, to doubt about the correctness of the conservation law of energy. In 1930, physicist Wolfgang Pauli suggested a hypothesis to explain the continuous spectrum behavior in the beta decay. He proposed the existence of a very light neutral particle (denoted by ν) emitted along with the beta particle.

$$X_Z^A \to Y_{Z-1}^A + e^- + \overline{\nu}_e. \tag{1.2}$$

The electron kinetic energy now also depends on the kinetic energy of the invisible particle $K_e = (m_X - m_Y - m_e)c^2 - K_\nu$. The continuous spectrum of the electron is therefore explained. The new particle is "undetectable" according to Pauli, and he first named it *neutron*. The neutron, found by James Chadwick later in 1932, is also a neutral particle but has the same mass as the proton. In July 1932, Enrico Fermi called Pauli's hypothesis particle *neutrino*, in Italian means "little neutral one". Since then, neutrino has had a name, and an amazing journey has started.

Pauli sighed after suggesting the existence of neutrino: "I have done a terrible thing: I have postulated a particle that cannot be detected". Neutrino has no electric charge, it does not have electromagnetic interaction; its very tiny mass makes it invisible to gravity. Extremely weak interactions with matter allow neutrino to pass through our bodies, the Earth, and the Sun without any deviation. Is there any chance to detect neutrino experimentally? The answer is yes. Twenty four years after Pauli's postulation, the first experimental evidence of neutrino was carried out by Clyde Cowan, Frederick Reines and their colleagues [35]. In this experiment, neutrinos were created by the Savannah River Plant near Augusta, Georgia state and detected by inverse beta decay

$$\overline{\nu}_e + p \rightarrow n + e^+. \tag{1.3}$$

After being created, the positron quickly annihilates with environmental electron to produce two gamma rays with prompt signals of 0.5 MeV energy. Neutron is captured by Cadmium nucleus to produce delayed gamma signal after 5 μs (Eq. 1.4)

$$n + {}^{108}Cd \rightarrow {}^{109}Cd^* \rightarrow {}^{109}Cd + \gamma. \tag{1.4}$$

These gamma rays were detected by 110 5-inch Photo-Multiplier Tube (PMT). Cowan and Reines's detector was placed at 11m from the reactor core, 12m underground, contained total of about 200 liters of water with about 40 kg dissolved cadmium chloride ($CdCl_2$). With intense flux of 5×10^{13} neutrinos per second, their detector could detect about three neutrinos per hour. This breakthrough result was recognized by the 1995 Nobel Prize in physics for Frederick Reines (Clyde Cowan died in 1974 at 54).

The one discovered by Cowan and Reines's experiment is electron anti-neutrino ($\overline{\nu}_e$). In 1962, Leon M. Lederman, Melvin Schwartz and Jack Steinberger discovered that there exists more than one type of neutrino [36]. This is the first time an intense neutrino beam was created from an accelerator, which had been independently proposed since the 1950s by Bruno Pontecorvo (Dubna, Soviet Union) and Melvin Schwartz (Colombia University and Brookhaven National Laboratory, USA). Leon Lederman, Jack Steinberger, and others from Columbia University together with Melvin Schwartz used Alternating Gradient Synchrotron (AGS) at Brookhaven to produce a 15 giga-electron-volt (GeV) proton beam. The proton beam was projected to a beryllium (Be) target, producing charged pions ($\pi^{\pm}$). Finally, charged pions decay into muons (μ) and neutrinos. At the detector, neutrinos interact with medium protons to produce associated leptons, almost muons. They claimed that there exists another

type of neutrino which is different from the one emitted along with electron in the beta decay. This type of neutrino is associated with muon, namely muon neutrino (ν_μ). Schwartz, Lederman, and Steinberger were honored by the 1988 Nobel Prize in physics for their discovery of the second type of neutrino.

In the SM, there are three leptons including electron, muon and tau. The existence of tau neutrino (ν_τ) was predicted right after the tau particle found in 1975. First efforts in searching for tau neutrino in 1980s at Fermilab was unsuccessful. In 1994, a group of about 40 scientists from USA, Japan, Korea and Greece initiated Direct observation of the nu tau, E872 (DONUT) experiment to directly detect tau neutrino. It is really difficult to detect neutrino in general, now it is even much harder to detect tau neutrino because its partner, tau lepton is more massive than muon or electron. After produced by interaction between tau neutrino and target nucleus, tau quickly decays into lighter leptons such as muon or electron. With a lifetime of about 30 pico-seconds ($30 \times 10^{-12} s$), tau only leaves a 1mm-track in the detector. In DONUT, proton beam was accelerated by Tevatron at Fermilab up to 800 GeV and projected to tunsten target to produce charm meson D_s (charm meson consists of one charm quark and one strange quark). Charm meson D_s then decays into tau lepton and tau anti-neutrino in beam dump. The DONUT detector was filled with nuclear emulsion with a total mass of 260 kg and situated after a 36-meter system of magnets and bulk matter to eliminate unwanted backgrounds. In July 2000, the DONUT collaboration announced the direct observation of tau neutrino for the first time [37]. So until the late 20th century, three types of neutrino flavor were experimentally discovered, including electron neutrino ν_e, muon neutrino ν_μ, and tau neutrino ν_τ.

1.1.2   Neutrino in Standard Model

In the SM, neutrinos only participate in weak interaction. Wu's 1957 experiment on cobalt-60 proved that parity is not conserved in the weak interaction. This experimental evidence confirms that weak interaction current is different from Quantum Electrodynamics (QED) and Quantum Chromodynamics (QCD) that have four-vector current of the form $j^\mu = \overline{\psi}\gamma^\mu\psi$ (ψ is Dirac spinor field). The other difference is that the weak interaction is mediated by massive $W^\pm$ and Z° bosons, while QED and QCD are mediated by massless bosons (photon for QED and eight gluons for QCD).

The requirement of Lorentz invariance on interaction matrix element restricts the form of weak interaction. The interaction current must be of the form $j^\mu = \overline{\psi}\Gamma\phi$, where Γ is a combination of Dirac γ matrices. There are only five of such combination [38]: scalar ($\overline{\psi}\phi$), pseudoscalar ($\overline{\psi}\gamma^5\phi$), vector ($\overline{\psi}\gamma^\mu\phi$), axial vector ($\overline{\psi}\gamma^\mu\gamma^5\phi$) and tensor ($\overline{\psi}(\gamma^\mu\gamma^\nu - \gamma^\nu\gamma^\mu)\phi$). It is known from experiment that charged current (CC) weak interaction must has a form of $V - A$ (vector minus axial vector). The $V - A$ structure of the weak interaction is characterized by a charged vertex factor

$$\frac{-ig_W}{\sqrt{2}}\gamma^\mu\frac{1}{2}(1 - \gamma^5), \tag{1.5}$$

and a neutral vertex factor

$$-ig_Z\gamma^\mu\frac{1}{2}(g_V - g_A\gamma^5),\tag{1.6}$$

where g_W and g_Z are strength couplings, g_V and g_A respectively are vector and axial-vector coupling constants, γ^μ are Dirac gamma matrices, and $\gamma^5 = i\gamma^0\gamma^1\gamma^2\gamma^3$. The corresponding four-vector CC and neutral current (NC) are

$$j_{CC}^\mu = \frac{g_W}{\sqrt{2}}\bar\psi\gamma^\mu\frac{1}{2}(1 - \gamma^5)\phi,\tag{1.7}$$

$$j_{NC}^\mu = g_Z\bar\psi\gamma^\mu\frac{1}{2}(g_V - g_A\gamma^5)\psi.\tag{1.8}$$

Left-handed and right-handed chiral projection operators are defined as

$$P_L = \frac{1}{2}(1 - \gamma^5), \qquad P_R = \frac{1}{2}(1 + \gamma^5),\tag{1.9}$$

with properties

$$P_L P_L = P_L, \quad P_R P_R = P_R, \quad P_L P_R = P_R P_L = 0, \quad P_L + P_R = 1,\tag{1.10}$$

and

$$P_L^\dagger = P_L, \quad P_R^\dagger = P_R, \quad P_L\gamma^0 = \gamma^0 P_R, \quad P_R\gamma^0 = \gamma^0 P_L.\tag{1.11}$$

In terms of left-handed and right-handed chiral projection operators, any Dirac field ψ can be decomposed into left-handed and right-handed chiral components as follows

$$\psi = \frac{1}{2}(1 - \gamma^5)\psi + \frac{1}{2}(1 + \gamma^5)\psi = P_L\psi + P_R\psi \equiv \psi_L + \psi_R.\tag{1.12}$$

We see that

$$\overline{\psi_L} = \overline{P_L\psi} = (P_L\psi)^\dagger\gamma^0 = \psi^\dagger P_L\gamma^0 = \psi^\dagger\gamma^0 P_R = \bar\psi P_R,\tag{1.13}$$

and

$$\overline{\psi_R} = \overline{P_R\psi} = (P_R\psi)^\dagger\gamma^0 = \psi^\dagger P_R\gamma^0 = \psi^\dagger\gamma^0 P_L = \bar\psi P_L.\tag{1.14}$$

Under charge conjugation, the Dirac spinor field and its adjoint transform as follows:

$$\psi \to \psi^C = C\overline{\psi}^T,\tag{1.15}$$

and

$$\overline{\psi} \to \overline{\psi}^C = -\psi^T C^{-1}.\tag{1.16}$$

In Dirac representation, charge conjugation operator C has an explicit form

$$C = i\gamma^0\gamma^2 = \begin{pmatrix} 0 & i\sigma_2 \\ i\sigma_2 & 0 \end{pmatrix}.\tag{1.17}$$

It is straightforward to verify that

$$P_L\psi_L = \psi_L,\tag{1.18}$$

$$P_L\psi_R = 0,\tag{1.19}$$

$$P_L\psi_L^C = 0,\tag{1.20}$$

$$P_L\psi_R^C = \psi_R^C.\tag{1.21}$$

The $V - A$ nature of CC weak interaction consequently leads to the fact that the currents associated to right-handed field and left-handed conjugate field are zero

$$j_{RR}^{\mu} = \frac{g_W}{\sqrt{2}}\overline{\psi}_R\gamma^{\mu}\frac{1}{2}(1 - \gamma^5)\phi_R = \frac{g_W}{\sqrt{2}}\overline{\psi}_R\gamma^{\mu}P_L\phi_R = 0, \qquad (1.22)$$

$$\overline{j}_{LL}^{\mu} = \frac{g_W}{\sqrt{2}}\overline{\psi}_L^C\gamma^{\mu}\frac{1}{2}(1 - \gamma^5)\phi_L^C = \frac{g_W}{\sqrt{2}}\overline{\psi}_L^C\gamma^{\mu}P_L\phi_L^C = 0, \qquad (1.23)$$

and only the currents associated with left-handed and right-handed conjugate fields are non-zero. This means that in the SM, only left-handed particles and right-handed anti-particles participate in the CC weak interaction.

In the case of neutrinos in the SM, where $m = 0$, the chiral and helicity states are the same. Hence, the $V - A$ nature allows only left-handed neutrinos and right-handed anti-neutrinos participate in the CC weak interaction.

1.1.3 Neutrino mass and seesaw mechanism

The neutrino oscillation phenomenon indicates that neutrinos do have masses. Therefore, we must have the mass term for neutrino in Lagrangian. The simplest way is to add right-handed neutrino into the SM and construct a Dirac mass term as follows

$$\mathcal{L}_D = -m_D\overline{\nu}_L\nu_R - m_D^T\overline{\nu}_R\nu_L. \qquad (1.24)$$

Since $\overline{\nu}_L\nu_R$ is equivalent to $\overline{\nu}_R^c\nu_L^c$ and $m_D^T\overline{\nu}_R\nu_L$ is the Hermitian conjugate (h.c) of $m_D\overline{\nu}_L\nu_R$, we can rewrite the above equation as follows

$$\mathcal{L}_D = -\frac{1}{2}m_D(\overline{\nu}_L\nu_R + \overline{\nu}_R^c\nu_L^c) + h.c. \qquad (1.25)$$

This way, however, is unnatural since neutrino masses are much smaller than other fermion masses. We then need to look for another mechanism to generate masses for neutrinos.

We already know that in the SM, right-handed neutrinos and left-handed antineutrinos transform as singlets under gauge transformation. As a result, any combination of them can be incorporated into the Lagrangian without disrupting gauge symmetry. Let ν_R to be right-handed neutrino and its CP conjugate field ν_R^c to be left-handed antineutrino. A gauge invariant Majorana mass term can be constructed as follows

$$\mathcal{L}_M = -\frac{1}{2}M\overline{\nu}_R^c\nu_R + h.c. \qquad (1.26)$$

This mass term however allows a direct coupling between a particle and an antiparticle which violates lepton number by two units ($\Delta L = \pm 2$). Since neutrinos are neutral particles, they can be their own anti-particles. If so, neutrino-less double beta decay can be experimentally found.

The most general mass term for neutrinos that can be incorporated into the SM

Lagrangian contains both Dirac (1.25) and Majorana (1.26) mass terms

$$
\begin{aligned}
\mathcal{L} &= \mathcal{L}_D + \mathcal{L}_M \\
&= -\frac{1}{2}m_D(\bar{\nu}_L\nu_R + \bar{\nu}_R^c\nu_L^c) - \frac{1}{2}M\bar{\nu}_R^c\nu_R + h.c \\
&= -\frac{1}{2}(m_D\bar{\nu}_L\nu_R + m_D\bar{\nu}_R^c\nu_L^c + M\bar{\nu}_R^c\nu_R) + h.c \\
&= -\frac{1}{2}\begin{pmatrix} \bar{\nu}_L & \bar{\nu}_R^c \end{pmatrix}\begin{pmatrix} 0 & m_D \\ m_D & M \end{pmatrix}\begin{pmatrix} \nu_L^c \\ \nu_R \end{pmatrix} + h.c.
\end{aligned}
\tag{1.27}
$$

The masses of physical states are eigenvalues of mass matrix

$$
\mathbf{M} = \begin{pmatrix} 0 & m_D \\ m_D & M \end{pmatrix}.
\tag{1.28}
$$

In order to find eigenvalues of the mass matrix, we solve the characteristic equation

$$
\begin{aligned}
&det(\mathbf{M} - \lambda I) = 0 \\
\Rightarrow\quad &\lambda^2 - M\lambda - m_D^2 = 0 \\
\Rightarrow\quad &m_\pm \equiv \lambda_\pm = \frac{M \pm \sqrt{M^2 + 4m_D^2}}{2}.
\end{aligned}
\tag{1.29}
$$

If the Majorana mass is taken to much larger than the Dirac mass, we obtain one light neutrino state

$$
|m_\nu| \approx \frac{m_D^2}{M},
\tag{1.30}
$$

and one heavy neutrino state

$$
m_N \approx M.
\tag{1.31}
$$

It is supposed that the Dirac mass term m_D should be at the order of other fermion masses (~ 1 GeV). In order for a light neutrino to have mass at order of 0.1 eV, the Majorana mass must be at the order of 10^{10} GeV!

1.1.4 Neutrino oscillation in vacuum

The neutrino oscillation can be well described by Pontecorvo–Maki–Nakagawa–Sakata (PMNS) framework. In this framework, the flavor eigenstates are related to the mass eigenstates by a 3×3 uniraty mixing matrix, so-called PMNS

$$
|\nu_\alpha\rangle = \sum_{i=1}^{3} U_{\alpha i}^*|\nu_i\rangle,
\tag{1.32}
$$

where $\nu_\alpha = (\nu_e,\ \nu_\mu,\ \nu_\tau)$ represent the flavor eigenstates and $\nu_i = (\nu_1,\ \nu_2,\ \nu_3)$ represent the mass eigenstates with corresponding masses $m_i = (m_1,\ m_2,\ m_3)$. The PMNS matrix can be parameterized by three mixing angles $(\theta_{12}, \theta_{13}, \theta_{23})$ and one Dirac phase

δ_{CP} as expressed in equation (1.33)

$$U_{PMNS} = \begin{pmatrix} U_{e1} & U_{e2} & U_{e3} \\ U_{\mu 1} & U_{\mu 2} & U_{\mu 3} \\ U_{\tau 1} & U_{\tau 2} & U_{\tau 3} \end{pmatrix}$$

$$= \begin{pmatrix} 1 & 0 & 0 \\ 0 & c_{23} & s_{23} \\ 0 & -s_{23} & c_{23} \end{pmatrix} \begin{pmatrix} c_{13} & 0 & s_{13}e^{-i\delta} \\ 0 & 1 & 0 \\ -s_{13}e^{i\delta} & 0 & c_{13} \end{pmatrix} \begin{pmatrix} c_{12} & s_{12} & 0 \\ -s_{12} & c_{12} & 0 \\ 0 & 0 & 1 \end{pmatrix}$$

$$= \begin{pmatrix} c_{12}c_{13} & s_{12}c_{13} & s_{13}e^{-i\delta} \\ -s_{12}c_{23} - c_{12}s_{23}s_{13}e^{i\delta} & c_{12}c_{23} - s_{12}s_{23}s_{13}e^{i\delta} & s_{23}c_{13} \\ s_{12}s_{23} - c_{12}c_{23}s_{13}e^{i\delta} & -c_{12}s_{23} - s_{12}c_{23}s_{13}e^{i\delta} & c_{23}c_{13} \end{pmatrix}, \quad (1.33)$$

where $s_{ij} = \sin\theta_{ij}$, $c_{ij} = \cos\theta_{ij}$ and δ_{CP} is the CP violating Dirac phase. If neutrinos are Majorana particles, the mixing matrix includes two additional phases which do not appear in the expression of oscillation probabilities. The unitarity of PMNS matrix implies $U^{-1} = U^\dagger \equiv (U^*)^T$. Then condition $UU^\dagger = I$ leaves nine equations:

$$\sum_{i=1}^{3} U_{\alpha i}U_{\beta i}^* = \delta_{\alpha\beta}, \quad (1.34)$$

where α and β can be e, μ, or τ. The mass eigenstates therefore can also be performed via flavor eigenstates as

$$|\nu_i\rangle = \sum_{\alpha}^{e,\nu,\tau} U_{\alpha i}|\nu_\alpha\rangle. \quad (1.35)$$

Time evolution of the wave function at the time t later is

$$|\nu_\alpha\rangle = \sum_{i=1}^{3} U_{\alpha i}^* e^{-i\phi_i}|\nu_i\rangle, \quad (1.36)$$

where $\phi_i = p_i.x_i = E_i t - \vec{p}_i.\vec{x}_i$. Taking into account the equation (1.35), we can rewrite the equation (1.36) as follows

$$|\nu_\alpha\rangle = \sum_{\beta}^{e,\mu,\tau}\sum_{i=1}^{3} U_{\alpha i}^* U_{\beta i} e^{-i\phi_i}|\nu_\beta\rangle. \quad (1.37)$$

Neutrino experiments often measure the oscillation probability from flavor ν_α to flavor ν_β after traveling some distance. The oscillation probability is defined as the square of the sum of the amplitudes as follows

$$P(\nu_\alpha \to \nu_\beta) = \left|\langle\nu_\beta|\nu_\alpha\rangle\right|^2 = \left|\sum_{i=1}^{3} U_{\alpha i}^* U_{\beta i} e^{-i\phi_i}\right|^2. \quad (1.38)$$

The neutrino masses are extremely small ($m_i \approx 0$), and their speeds are near the speed of light in vacuum ($v_\nu \approx c$), in natural unit ($c = 1$) we have $t \approx L$. Also from relativity relation $E^2 = p^2 + m^2$ we deduce $E - p = \frac{m^2}{E+p} \approx \frac{m^2}{2E}$. Therefore at distance $x = L$ from the neutrino source, we can express the phase factor in terms of the neutrino mass m_i, energy E and distance traveled L as

$$\phi_i = p_i.x_i = E_i t - \vec{p}_i.\vec{x}_i = (E_i - p_i)L \approx \frac{m_i^2 L}{2E}. \tag{1.39}$$

If $\phi_1 = \phi_2 = \phi_3$ ($\approx \frac{m^2 L}{2E}$), from unitary condition (1.34) we can see that the oscillation probability is now simplified to

$$P(\nu_\alpha \to \nu_\beta) = \left| \sum_{i=1}^{3} U_{\alpha i}^* U_{\beta i} \right|^2 e^{i\frac{m^2 L}{2E}} e^{-i\frac{m^2 L}{2E}} = \delta_{\alpha\beta}. \tag{1.40}$$

If $\alpha \neq \beta$, then $P(\nu_\alpha \to \nu_\beta) = 0$, there is no oscillation at all. Equivalently, the oscillation occurs only if the neutrinos have masses ($m_i \neq 0$) and the masses are not the same ($m_1 \neq m_2 \neq m_3$).

The equation (1.38) can be rewritten in the most common form :

$$P(\nu_\alpha \to \nu_\beta) = \delta_{\alpha\beta} \quad - \quad 4 \sum_{i>j} Re \left[U_{\alpha i}^* U_{\beta i} U_{\alpha j} U_{\beta j}^* \right] \sin^2 \left(\frac{\Delta m_{ij}^2}{4E} L \right)$$

$$+ \quad 2 \sum_{i>j} Im \left[U_{\alpha i}^* U_{\beta i} U_{\alpha j} U_{\beta j}^* \right] \sin \left(\frac{\Delta m_{ij}^2}{2E} L \right), \tag{1.41}$$

where $\Delta m_{ij}^2 = m_i^2 - m_j^2$. The formula for antineutrino can be achieved by taking the complex conjugate of the product matrix

$$P(\bar{\nu}_\alpha \to \bar{\nu}_\beta) = \delta_{\alpha\beta} \quad - \quad 4 \sum_{i>j} Re \left[U_{\alpha i}^* U_{\beta i} U_{\alpha j} U_{\beta j}^* \right] \sin^2 \left(\frac{\Delta m_{ij}^2}{4E} L \right)$$

$$- \quad 2 \sum_{i>j} Im \left[U_{\alpha i}^* U_{\beta i} U_{\alpha j} U_{\beta j}^* \right] \sin \left(\frac{\Delta m_{ij}^2}{2E} L \right). \tag{1.42}$$

The probabilities (1.41) and (1.42) are called *transition probabilities* or *appearance channels* at experiments. The *survival probabilities* or *disappearance channels* for a flavor α is

$$P(\nu_\alpha \to \nu_\alpha) = P(\bar{\nu}_\alpha \to \bar{\nu}_\alpha) = 1 - 4 \sum_{i>j} |U_{\alpha i}|^2 |U_{\alpha j}|^2 \sin^2 \left(\frac{\Delta m_{ij}^2}{4E} L \right). \tag{1.43}$$

By restoring $\hbar$ and c into the phases of (1.41), (1.42) and (1.43), we can express them in a practical form

$$\frac{\Delta m_{ij}^2 [kg]^2 L[m]}{4E[J]} \frac{c^3}{\hbar} = \frac{\Delta m_{ij}^2 [eV]^2}{(5.61 \times 10^{35})^2} \cdot \frac{L[km]}{10^{-3}} \cdot \frac{6.25 \times 10^9}{4E[GeV]} \frac{(2.998 \times 10^8)^3}{1.055 \times 10^{-34}}$$

$$= 1.269 \frac{\Delta m_{ij}^2 [eV^2] L[km]}{E[GeV]}. \tag{1.44}$$

In accelerator-based experiments, muon (anti-)neutrino $\nu_\mu(\bar{\nu}_\mu)$ is produced at the source by shooting a proton beam to a graphite target. At low energy of few GeVs, muon (anti-)neutrino transforms into electron (anti-)neutrino $\nu_e(\bar{\nu}_e)$ and be detected at the detector. The reactor-based experiments study the disappearance of electron anti-neutrino $\bar{\nu}_e$ created by nuclear reactions. Now we will derive the specific oscillation formulae for the channels studied in a given experiment.

Survival probability $P(\nu_\mu \to \nu_\mu)$ in vacuum

In the scope of PMNS model, the survival probability $P(\nu_\mu \to \nu_\mu)$ in vacuum can be written down from equation (1.43) as follows.

$$
\begin{aligned}
P(\nu_\mu \to \nu_\mu) = P(\bar{\nu}_\mu \to \bar{\nu}_\mu) = 1 \quad &- \quad 4|U_{\mu 1}|^2|U_{\mu 2}|^2 \sin^2 \Delta_{21} \\
&- \quad 4|U_{\mu 1}|^2|U_{\mu 3}|^2 \sin^2 \Delta_{31} \\
&- \quad 4|U_{\mu 2}|^2|U_{\mu 3}|^2 \sin^2 \Delta_{32},
\end{aligned}
\tag{1.45}
$$

in which $\Delta_{ij} = \frac{\Delta m_{ij}^2 L}{4E}$. In order to calculate a complete formula, we first write down the explicit form of PMNS matrix elements

$$
\begin{aligned}
U_{\mu 1} &= -(s_{12}c_{23} + c_{12}s_{23}s_{13}\cos\delta) - ic_{12}s_{23}s_{13}\sin\delta, & (1.46) \\
U_{\mu 1}^* &= -(s_{12}c_{23} + c_{12}s_{23}s_{13}\cos\delta) + ic_{12}s_{23}s_{13}\sin\delta, & (1.47) \\
U_{\mu 2} &= (c_{12}c_{23} - s_{12}s_{23}s_{13}\cos\delta) - is_{12}s_{23}s_{13}\sin\delta, & (1.48) \\
U_{\mu 2}^* &= (c_{12}c_{23} - s_{12}s_{23}s_{13}\cos\delta) + is_{12}s_{23}s_{13}\sin\delta, & (1.49) \\
U_{\mu 3} &= U_{\mu 3}^* = s_{23}c_{13}. & (1.50)
\end{aligned}
$$

Then we can calculate the relevant terms in equation (1.45)

$$
\begin{aligned}
|U_{\mu 1}|^2 &= (s_{12}c_{23} + c_{12}s_{23}s_{13}\cos\delta)^2 + (c_{12}s_{23}s_{13}\sin\delta)^2, & (1.51) \\
|U_{\mu 2}|^2 &= (c_{12}c_{23} - s_{12}s_{23}s_{13}\cos\delta)^2 + (s_{12}s_{23}s_{13}\sin\delta)^2, & (1.52) \\
|U_{\mu 3}|^2 &= s_{23}^2 c_{13}^2. & (1.53)
\end{aligned}
$$

Inserting the expressions (1.51) - (1.53) into equation (1.45) and rearrange the common terms, we get the complete form of survival probability in vacuum

$$
\begin{aligned}
P(\nu_\mu \to \nu_\mu) = {}& 1 - \sin 2\theta_{12} \sin 2\theta_{13} \sin 2\theta_{23} s_{23}^2 c_{13} \cos\delta(\sin^2 \Delta_{31} - \sin^2 \Delta_{32}) \\
& - \big[\sin^2 2\theta_{12}(c_{23}^4 + s_{23}^4 s_{13}^4) + \sin^2 2\theta_{23}(s_{12}^4 + c_{12}^4)s_{13}^2 \\
& + \sin 4\theta_{12} \sin 2\theta_{23}(c_{23}^2 - s_{23}^2 s_{13}^2)s_{13}\cos\delta \\
& - \sin^2 2\theta_{12} \sin^2 2\theta_{23}s_{13}^2 \cos^2\delta\big]\sin^2 \Delta_{21} \\
& - c_{13}^2 \sin^2 2\theta_{23}(s_{12}^2 \sin^2 \Delta_{31} + c_{12}^2 \sin^2 \Delta_{32}) \\
& - s_{23}^4 \sin^2 2\theta_{13}(c_{12}^2 \sin^2 \Delta_{31} + s_{12}^2 \sin^2 \Delta_{32}).
\end{aligned}
\tag{1.54}
$$

We have known that $\Delta m_{21}^2 \approx 7.5 \times 10^{-5} eV^2$ is much smaller than $\Delta m_{31}^2 \approx \Delta m_{32}^2 \approx 2.55 \times 10^{-3} eV^2$. Hence, for long-baseline neutrino oscillation experiments like T2K and
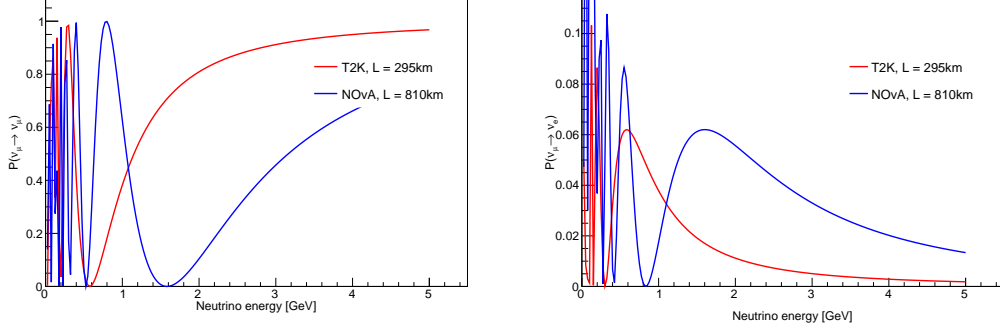
Figure 1.1: Survival probabilities $P(\nu_\mu \to \nu_\mu)$ (left) and transition probabilities $P(\nu_\mu \to \nu_e)$ (right) at T2K (red line) and NOνA (blue line).
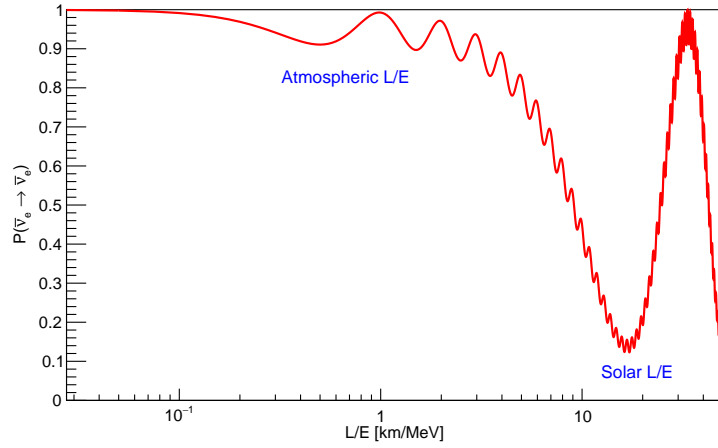
Figure 1.2: The $\overline{\nu}_e$ survival probability as a function of L/E.

NOνA, we can ignore the second order terms of Δ_{21}. Also the mixing angle $\theta_{13} \approx 8.5°$, so the approximations $c_{13} \approx 1, s_{13} \approx 0$ hold. The equation (1.54) can be rewritten in approximation form as

$$P(\nu_\mu \to \nu_\mu) \approx 1 - \sin^2 2\theta_{23} \sin^2 \left(\frac{\Delta m_{31}^2 L}{4E} \right). \tag{1.55}$$

With the help of (1.44), we can rewrite eq. (1.55) in a practical form

$$P(\nu_\mu \to \nu_\mu) \approx 1 - \sin^2 2\theta_{23} \sin^2 \left(1.27 \frac{\Delta m_{31}^2 [eV]^2 L[km]}{E[GeV]} \right). \tag{1.56}$$

We can see from the equation (1.56) that the disappearance channel at long baseline experiments like T2K and NOνA are sensitive to atmospheric parameters θ_{23} and Δm_{31}^2. Fig. 1.1 (left) demonstrates the probability (1.56) as a function of neutrino energy for different baselines: The red line is for T2K with a baseline of $L = 295 km$ and the blue line is for NOνA with a baseline of $L = 810 km$.

Transition probability $P(\nu_\mu \to \nu_e)$ in vacuum

From the general equation (1.41), we rewrite the transition probability in a convenient form

$$
\begin{aligned}
P(\nu_\mu \to \nu_e) = \; & -4Re\left[U_{\mu1}^* U_{e1} U_{\mu2} U_{e2}^*\right] \sin^2 \Delta_{21} \\
& -4Re\left[U_{\mu1}^* U_{e1} U_{\mu3} U_{e3}^*\right] \sin^2 \Delta_{31} \\
& -4Re\left[U_{\mu2}^* U_{e2} U_{\mu3} U_{e3}^*\right] \sin^2 \Delta_{32} \\
& +8Im\left[U_{\mu1}^* U_{e1} U_{\mu3} U_{e3}^*\right] \sin \Delta_{21} \sin \Delta_{31} \sin \Delta_{32}.
\end{aligned}
\tag{1.57}
$$

By referring to the PMNS matrix, we now can calculate the terms in (1.57) as follows:

$$
\begin{aligned}
Re[U_{\mu1}^* U_{e1} U_{\mu2} U_{e2}^*] = \; & -\left[s_{12}^2 c_{12}^2 c_{13}^2 c_{23}^2 - s_{12}^2 c_{12}^2 s_{13}^2 c_{13}^2 s_{23}^2 \right. \\
& \left. +(c_{12}^2 - s_{12}^2)s_{12}c_{12}s_{13}c_{13}^2 s_{23}c_{23} \cos \delta\right],
\end{aligned}
\tag{1.58}
$$

$$
Re[U_{\mu1}^* U_{e1} U_{\mu3} U_{e3}^*] = -c_{12}c_{13}^2 s_{23}(c_{12}s_{13}^2 s_{23} + s_{12}s_{13}c_{23} \cos \delta),
\tag{1.59}
$$

$$
Re[U_{\mu2}^* U_{e2} U_{\mu3} U_{e3}^*] = s_{12}c_{13}^2 s_{23}(c_{12}s_{13}c_{23} \cos \delta - s_{12}s_{13}^2 s_{23}),
\tag{1.60}
$$

$$
Im[U_{\mu1}^* U_{e1} U_{\mu3} U_{e3}^*] = -s_{12}c_{12}s_{13}c_{13}^2 s_{23}c_{23} \sin \delta.
\tag{1.61}
$$

Substituting the above expressions into (1.57), we get the complete formula of transition probability in vacuum

$$
\begin{aligned}
P(\nu_\mu \to \nu_e) = \; & \frac{1}{4}\left[4\sin^2 2\theta_{12}c_{13}^2 c_{23}^2 - \sin^2 2\theta_{12}\sin^2 2\theta_{13}s_{23}^2\right] \sin^2 \Delta_{21} \\
& +\frac{1}{4}\sin 4\theta_{12}\sin 2\theta_{13}\sin 2\theta_{23}c_{13}\cos \delta \sin^2 \Delta_{21} \\
& +\sin^2 2\theta_{13}s_{23}^2(c_{12}^2 \sin^2 \Delta_{31} + s_{12}^2 \sin^2 \Delta_{32}) \\
& +\frac{1}{2}\sin 2\theta_{12}\sin 2\theta_{13}\sin 2\theta_{23}c_{13}\cos \delta(\sin^2 \Delta_{31} - \sin^2 \Delta_{32}) \\
& -\sin 2\theta_{12}\sin 2\theta_{13}\sin 2\theta_{23}c_{13}\sin \delta \sin \Delta_{21}\sin \Delta_{31}\sin \Delta_{32}.
\end{aligned}
\tag{1.62}
$$

By dropping out the second order terms of Δ_{21} and making approximation $\Delta_{31} \approx \Delta_{32}$, we can get the approximation form of the transition probability

$$
\begin{aligned}
P(\nu_\mu \to \nu_e) \approx \; & \sin^2 2\theta_{13}s_{23}^2 \sin^2 \Delta_{31} \\
& -\sin 2\theta_{12}\sin 2\theta_{13}\sin 2\theta_{23}c_{13}\sin \delta \sin \Delta_{21}\sin^2 \Delta_{31}.
\end{aligned}
\tag{1.63}
$$

The equation (1.63) says that the appearance channel in long baseline experiments like T2K and NOνA is sensitive to mixing angles θ_{13}, θ_{23}, CP violating phase $\delta_{CP} \equiv \delta$ and mass squared difference Δm_{31}^2. Fig. 1.1 (right) demonstrates the probability (1.63) as a function of neutrino energy for different baselines: The red line is for T2K and the blue line is for NOνA.

Survival probability $P(\bar{\nu}_e \to \bar{\nu}_e)$ in vacuum

From equation (1.43) we can write down the probability of $\bar{\nu}_e$ disappearance as

bellows:

$$P(\bar{\nu}_e \to \bar{\nu}_e) = 1 \quad - \quad 4|U_{e1}|^2|U_{e2}|^2 \sin^2 \Delta_{21}$$
$$- \quad 4|U_{e1}|^2|U_{e3}|^2 \sin^2 \Delta_{31}$$
$$- \quad 4|U_{e2}|^2|U_{e3}|^2 \sin^2 \Delta_{32}. \tag{1.64}$$

By using $|U_{e1}|^2 = c_{12}^2 c_{13}^2$, $|U_{e2}|^2 = s_{12}^2 c_{13}^2$, $|U_{e3}|^2 = s_{13}^2$, we can explicitly write down the equation (1.64)

$$P(\bar{\nu}_e \to \bar{\nu}_e) = 1 \quad - \quad 4s_{12}^2 c_{12}^2 c_{13}^4 \sin^2 \Delta_{21}$$
$$- \quad 4c_{12}^2 s_{13}^2 c_{13}^2 \sin^2 \Delta_{31}$$
$$- \quad 4s_{12}^2 s_{13}^2 c_{13}^2 \sin^2 \Delta_{32}. \tag{1.65}$$

For reactor experiments at solar L/E which is around 16 km/MeV (see Fig. 1.2) such as KamLAND and JUNO where the solar term dominates ($\Delta_{21} = \pi/2$), we can rewrite the equation (1.65) as

$$P(\bar{\nu}_e \to \bar{\nu}_e) \approx 1 - \sin^2 2\theta_{12} c_{13}^4 \sin^2 \Delta_{21}. \tag{1.66}$$

These experiments are sensitive to θ_{12}, θ_{13} and Δm_{21}^2. For reactor experiments at atmospheric L/E which is around 0.5 km/MeV (see Fig. 1.2) such as Double-Chooz and Daya Bay, the atmospheric terms dominate ($\Delta_{31} \approx \Delta_{32} = \pi/2$). The equation (1.65) can be rewritten as

$$P(\bar{\nu}_e \to \bar{\nu}_e) \approx 1 - \sin^2 2\theta_{13} \sin^2 \Delta_{31}. \tag{1.67}$$

These experiments are sensitive to θ_{13} and Δm_{31}^2. Fig. 1.2 demonstrates the $\bar{\nu}_e$ survival probability as a function of L/E.

1.1.5 Neutrino oscillation in matter

In this section, we will revisit the derivation of the oscillation probability of neutrinos in matter. We mainly follow the notations and steps mentioned in Ref. [39]. When passing through ordinary matter such as in the Sun or the Earth, neutrinos may be affected by the matter effect or Mikheyev–Smirnov–Wolfenstein (MSW) effect [40], [41]. Matter may enhance the oscillation probability of neutrinos while depressing the one of antineutrinos. This consequently causes a fake CP violation effect. It is therefore important to study matter effect in searching for CP violation in neutrino oscillation experiments. In matter, neutrinos may undergo incoherent or coherent forward scatterings. For normal matter with number density $N \sim 10^{24}/cm^3$ and low energy neutrino ($< 10^5$ GeV), the probability of incoherent scattering is very small and can be neglected [42]. At low momentum transfer, the coherent forward elastic scattering is significant and responsible for the matter effect in neutrino oscillation [42] [43].
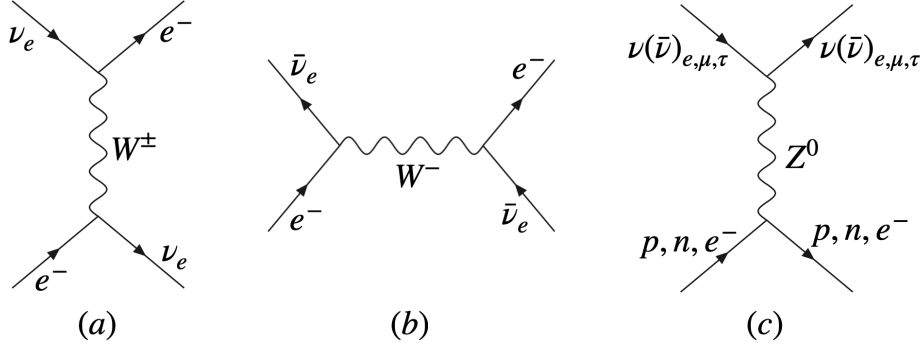
Figure 1.3: Feynman diagrams for CC and NC coherent forward scatterings of neutrinos.

We will first derive the matter-induced potentials of neutrinos. The forward scatterings can be CC or NC. For NC which produces NC potential V_{NC}, all three flavors of (anti-)neutrino $\nu_e(\bar{\nu}_e)$, $\nu_\mu(\bar{\nu}_\mu)$, $\nu_\tau(\bar{\nu}_\tau)$ can interact with electron, proton or neutron of matter by exchange of Z^0 boson. For CC which creates CC potential V_{CC}, electron neutrino can scatter off and electron antineutrino can annihilate with electrons by exchange of $W^\pm$ bosons. Let us first consider CC interactions demonstrated by the Feynman diagrams (a) and (b) in Fig. 1.3. At low neutrino energy, the effective Hamiltonian is [42]

$$
\begin{aligned}
H_{CC} &= \frac{G_F}{\sqrt{2}} \left[\bar{e}\gamma_\mu(1-\gamma^5)\nu_e\right]\left[\bar{\nu}_e\gamma^\mu(1-\gamma^5)e\right] \\
&= \frac{G_F}{\sqrt{2}} \left[\bar{e}\gamma_\mu(1-\gamma^5)e\right]\left[\bar{\nu}_e\gamma^\mu(1-\gamma^5)\nu_e\right],
\end{aligned} \tag{1.68}
$$

in which the second line can be achieved by using Fierz transformation. In a homogeneous and isotropic gas of unpolarized electrons, the Hamiltonian (1.68) is calculated to be

$$
H_{CC} = V_{CC}\bar{\nu}_e\gamma^0\nu_e, \tag{1.69}
$$

where

$$
V_{CC} = \sqrt{2}G_F N_e \tag{1.70}
$$

is the CC potential, N_e is the electron density of the medium. The effective Hamiltonian for NC interactions is

$$
H_{NC} = \frac{G_F}{\sqrt{2}} \sum_\alpha \left[\bar{\nu}_\alpha\gamma^\mu(1-\gamma^5)\nu_\alpha\right] \sum_f \left[\bar{f}\gamma_\mu(g_V^f - g_A^f\gamma^5)f\right], \tag{1.71}
$$

where $\alpha = (e, \mu, \tau)$ and $f = (e, p, n)$. As for the CC potential, we get the NC potential of the similar form

$$
V_{NC} = \sqrt{2}G_F N_f g_V^f. \tag{1.72}
$$

We note that

$$g_V^e = -\frac{1}{2} + 2\sin^2\theta_W, \tag{1.73}$$

$$g_V^p = 2g_V^u + g_V^d = \frac{1}{2} - 2\sin^2\theta_W, \tag{1.74}$$

$$g_V^n = g_V^u + 2g_V^d = -\frac{1}{2}. \tag{1.75}$$

Ordinary matter on the Earth consists of electrons, protons, and neutrons. In normal condition, the medium is electrically neutral, which implies the equality of the number of electrons and the number of protons, $N_e = N_p$. That means the NC current potentials of electrons and protons cancel out each other $(V_{NC})_e + (V_{NC})_p = 0$, leaving only contribution of the neutron NC potential

$$V_{NC} = -\frac{1}{2}\sqrt{2}G_F N_n, \tag{1.76}$$

where N_n is the neutron density of the medium. Finally, the effective Hamiltonian of neutrino interaction in matter is

$$H_{eff} = \sum_\alpha V_\alpha \bar{\nu}_{\alpha L}\gamma^0 \nu_{\alpha L}, \tag{1.77}$$

where

$$\begin{aligned} V_\alpha &= V_{CC}\delta_{\alpha e} + V_{NC} \\ &= \sqrt{2}G_F(N_e\delta_{\alpha e} - \frac{1}{2}N_n). \end{aligned} \tag{1.78}$$

For antineutrino, we replace V_α by $-V_\alpha$ in equation (1.78).

We now derive the oscillation probability of neutrinos in matter from Hamiltonian formalism. Let us recall the relation (1.32) between mass eigenstates and flavor eigenstates

$$|\nu_\alpha\rangle = \sum_{i=1}^{3} U_{\alpha i}^* |\nu_i\rangle. \tag{1.79}$$

The total Hamiltonian H of neutrino in matter consists of a vacuum part H_0 and a matter part H_I as follows

$$H = H_0 + H_I, \tag{1.80}$$

where

$$H_0|\nu_i\rangle = E_i|\nu_i\rangle \quad \text{with} \quad E_i = \sqrt{p_i^2 + m_i^2} \approx p + \frac{m_i^2}{2E}, \tag{1.81}$$

$$H_I|\nu_\alpha\rangle = V_\alpha|\nu_\alpha\rangle = (V_{CC}\delta_{\alpha e} + V_{NC})|\nu_\alpha\rangle. \tag{1.82}$$

In the previous section, we have worked with the mass eigenstate basis to derive oscillation probability formulae in vacuum. In matter, it is however more convenient to work with the flavor basis since the matter-induced potentials of neutrinos are diagonal in this basis. In terms of the flavor basis, the vacuum Hamiltonian now becomes

$$UH_0U^\dagger|\nu_\alpha\rangle = U_{\alpha i}E_i U_{\alpha i}^\dagger|\nu_\alpha\rangle = \left(p + U_{\alpha i}\frac{m_i^2}{2E}U_{\alpha i}^\dagger\right)|\nu_\alpha\rangle. \tag{1.83}$$

The Schrodinger equation for neutrino in matter in the flavor basis is

$$
\begin{aligned}
i\frac{d}{dt}|\nu_\alpha(t)\rangle &= H|\nu_\alpha(t)\rangle \\
&= (H_0 + H_I)|\nu_\alpha(t)\rangle \\
&= \left(p + U_{\alpha i}\frac{m_i^2}{2E}U_{\alpha i}^\dagger + V_\alpha\right)|\nu_\alpha(t)\rangle \\
&= \left(p + U_{\alpha i}\frac{m_i^2}{2E}U_{\alpha i}^\dagger + V_{CC}\delta_{\alpha e} + V_{NC}\right)|\nu_\alpha(t)\rangle \\
&= \left[\left(p + \frac{m_1^2}{2E} + V_{NC}\right) + \left(U_{\alpha k}\frac{\Delta m_{k1}^2}{2E}U_{\alpha k}^\dagger + V_{CC}\delta_{\alpha e}\right)\right]|\nu_\alpha(t)\rangle,
\end{aligned} \tag{1.84}
$$

$k = (2,\ 3)$. From the fourth to the last line, we have added the term $(U_{\alpha 1}\frac{m_1^2}{2E}U_{\alpha 1}^\dagger - U_{\alpha 1}\frac{m_1^2}{2E}U_{\alpha 1}^\dagger)$. We can see that $p + \frac{m_1^2}{2E} + V_{NC}$ is the same for all neutrinos. They generate a phase common to all flavors and will cancel out in transition by a phase shift

$$
|\nu_\alpha(t)\rangle \to |\nu_\alpha(t)\rangle e^{-\mathrm{diag}(X,0,0)}, \tag{1.85}
$$

where $X = p + \frac{m_1^2}{2E} + V_{NC}$ (note that $e^{\mathrm{diag}(X,0,0)} = \mathrm{diag}(X,1,1)$). Hence, we can ignore them here for simplicity. So we rewrite the above equation as

$$
i\frac{d}{dt}|\nu_\alpha(t)\rangle = \left(U_{\alpha k}\frac{\Delta m_{k1}^2}{2E}U_{\alpha k}^\dagger + V_{CC}\delta_{\alpha e}\right)|\nu_\alpha(t)\rangle. \tag{1.86}
$$

or explicitly

$$
i\frac{d}{dt}\begin{pmatrix} \nu_e \\ \nu_\mu \\ \nu_\tau \end{pmatrix} = \left[\frac{1}{2E}U\begin{pmatrix} 0 & 0 & 0 \\ 0 & \Delta m_{21}^2 & 0 \\ 0 & 0 & \Delta m_{31}^2 \end{pmatrix}U^\dagger + \begin{pmatrix} V_{CC} & 0 & 0 \\ 0 & 0 & 0 \\ 0 & 0 & 0 \end{pmatrix}\right]\begin{pmatrix} \nu_e \\ \nu_\mu \\ \nu_\tau \end{pmatrix} \tag{1.87}
$$

The total Hamiltonian now can be separated into two parts

$$
\begin{aligned}
H &= H_0 + H_I \tag{1.88} \\
&= \frac{1}{2E}U\begin{pmatrix} 0 & 0 & 0 \\ 0 & 0 & 0 \\ 0 & 0 & \Delta m_{31}^2 \end{pmatrix}U^\dagger + \frac{1}{2E}\left[U\begin{pmatrix} 0 & 0 & 0 \\ 0 & \Delta m_{21}^2 & 0 \\ 0 & 0 & 0 \end{pmatrix}U^\dagger + \begin{pmatrix} a & 0 & 0 \\ 0 & 0 & 0 \\ 0 & 0 & 0 \end{pmatrix}\right],
\end{aligned}
$$

in which $a = 2EV_{CC} = 2\sqrt{2}EG_F N_e$ represents the matter effect. Since Δm_{21}^2 and a are at the order of $\sim \mathcal{O}(10^{-5})$ which are much smaller than $\Delta m_{31}^2 \sim \mathcal{O}(10^{-3})eV^2$, we can treat H_I as a pertubation. The Schrodinger equation has a solution of Dyson series form

$$
|\nu(x)\rangle = S(x)|\nu(0)\rangle, \tag{1.89}
$$

where $S(x) \equiv Te^{\int_0^x H(s)ds}$, T is the symbol of time ordering. The oscillation probability at distance $x = L$ then can be calculated through $S(x)$

$$
P(\nu_\alpha \to \nu_\beta) = |S_{\beta\alpha}(L)|^2. \tag{1.90}
$$

We have

$$S_0(x) = e^{-iH_0 x}, \tag{1.91}$$

and

$$S_1(x) = e^{-iH_0 x}(-i) \int_0^x ds H_1(s) = e^{-iH_0 x}(-i) \int_0^x ds e^{iH_0 s} H_1 e^{-iH_0 s}. \tag{1.92}$$

We now calculate $S_0(x)$ and $S_1(x)$ as follows

$$
\begin{aligned}
(S_0(x))_{\beta\alpha} &= \left[U e^{-i\frac{x}{2E} diag(0,0,\Delta m_{31}^2)} U^\dagger \right]_{\beta\alpha} \\
&= \sum_{i,j} \left[U_{\beta i} \left(e^{-i\frac{x}{2E} diag(0,0,\Delta m_{31}^2)} \right)_{ij} U_{\alpha j}^* \right].
\end{aligned} \tag{1.93}
$$

Note that

$$
e^{-i\frac{x}{2E} diag(0,0,\Delta m_{31}^2)} = \begin{pmatrix} 1 & 0 & 0 \\ 0 & 1 & 0 \\ 0 & 0 & e^{-i\frac{\Delta m_{31}^2 x}{2E}} \end{pmatrix}. \tag{1.94}
$$

Hence

$$
\begin{aligned}
(S_0(x))_{\beta\alpha} &= U_{\beta 1} U_{\alpha 1}^* .1 + U_{\beta 1} U_{\alpha 2}^* .0 + U_{\beta 1} U_{\alpha 3}^* .0 \\
&\quad + U_{\beta 2} U_{\alpha 1}^* .0 + U_{\beta 2} U_{\alpha 2}^* .1 + U_{\beta 2} U_{\alpha 3}^* .0 \\
&\quad + U_{\beta 3} U_{\alpha 1}^* .0 + U_{\beta 3} U_{\alpha 2}^* .0 + U_{\beta 3} U_{\alpha 3}^* .e^{-i\frac{\Delta m_{31}^2 x}{2E}} \\
&= U_{\beta 1} U_{\alpha 1}^* + U_{\beta 2} U_{\alpha 2}^* + U_{\beta 3} U_{\alpha 3}^* .e^{-i\frac{\Delta m_{31}^2 x}{2E}}.
\end{aligned} \tag{1.95}
$$

By using $U_{\beta 1} U_{\alpha 1}^* + U_{\beta 2} U_{\alpha 2}^* + U_{\beta 3} U_{\alpha 3}^* = \delta_{\alpha\beta}$ we can deduce

$$(S_0(x))_{\beta\alpha} = \delta_{\alpha\beta} + U_{\beta 3} U_{\alpha 3}^* \left(e^{-i\frac{\Delta m_{31}^2 x}{2E}} - 1 \right). \tag{1.96}$$

We now can calculate $(S_1(x))_{\beta\alpha}$

$$
\begin{aligned}
(S_1(x))_{\beta\alpha} &= \left(e^{-iH_0 x}(-i) \int_0^x ds e^{iH_0 s} H_1 e^{-iH_0 s} \right)_{\beta\alpha} \\
&= -i \int_0^x ds \left(e^{-iH_0(x-s)} H_1 e^{-iH_0 s} \right)_{\beta\alpha} \\
&= -i \int_0^x ds \left(U e^{-i\frac{x-s}{2E} diag(0,0,\Delta m_{31}^2)} U^\dagger H_1 U e^{-i\frac{s}{2E} diag(0,0,\Delta m_{31}^2)} U^\dagger \right)_{\beta\alpha} \\
&= -i \int_0^x ds \sum_{i,j',i',j} \left[U_{\beta i} \left(e^{-i\frac{x-s}{2E} diag(0,0,\Delta m_{31}^2)} \right)_{ij'} \right. \\
&\qquad\qquad \left. \times U_{\gamma j'}^* (H_1)_{\gamma\sigma} U_{\sigma i'} \left(e^{-i\frac{s}{2E} diag(0,0,\Delta m_{31}^2)} \right)_{i'j} U_{\alpha j}^* \right].
\end{aligned} \tag{1.97}
$$

Since $\left(e^{-i\frac{x-s}{2E} diag(0,0,\Delta m_{31}^2)} \right)_{ij'} = 0$ for $j' \neq i$ and $\left(e^{-i\frac{s}{2E} diag(0,0,\Delta m_{31}^2)} \right)_{i'j} = 0$ for $i' \neq j$.

We deduce

$$(S_1(x))_{\beta\alpha} =$$
$$-i \int_0^x ds \sum_{i,j} \left[U_{\beta i} \left(e^{-i\frac{x-s}{2E} diag(0,0,\Delta m_{31}^2)} \right)_{ii} U_{\gamma i}^*(H_1)_{\gamma\sigma} U_{\sigma j} \left(e^{-i\frac{s}{2E} diag(0,0,\Delta m_{31}^2)} \right)_{jj} U_{\alpha j}^* \right]$$
$$= -i \sum_{i,j} U_{\beta i} U_{\gamma i}^*(H_1)_{\gamma\sigma} U_{\sigma j} U_{\alpha j}^* \int_0^x ds \left(e^{-i\frac{\Delta m_{31}^2}{2E}[(x-s)\delta_{i3}+s\delta_{j3}]} \right). \tag{1.98}$$

Let

$$X_{ij} = U_{\beta i} U_{\gamma i}^*(H_1)_{\gamma\sigma} U_{\sigma j} U_{\alpha j}^*, \tag{1.99}$$

and

$$Y_{ij} = \int_0^x ds \left(e^{-i\frac{\Delta m_{31}^2}{2E}[(x-s)\delta_{i3}+s\delta_{j3}]} \right) = \int_0^x ds \left(e^{-i\frac{\Delta m_{31}^2 x}{2E}\delta_{i3}} . e^{-i\frac{\Delta m_{31}^2 s}{2E}(\delta_{j3}-\delta_{i3})} \right). \tag{1.100}$$

We first calculate the X_{ij} term. We see that

$$U_{\gamma i}^*(H_1)_{\gamma\sigma} U_{\sigma j} = \frac{1}{2E}[U_{\gamma i}^*(V_{12})_{\gamma\sigma} U_{\sigma j} + U_{\gamma i}^*(V_a)_{\gamma\sigma} U_{\sigma j}]. \tag{1.101}$$

Since $U_{\gamma i}^*(V_{12})_{\gamma\sigma} U_{\sigma j} = \text{diag}(0, \Delta m_{21}^2, 0)$ then

$$\frac{1}{2E} U_{\gamma i}^*(V_{12})_{\gamma\sigma} U_{\sigma j} = \frac{\Delta m_{21}^2}{2E} \delta_{2i} \delta_{2j}. \tag{1.102}$$

Since $(V_a)_{11} = a$ and $(V_a)_{\gamma\sigma} = 0$ for $\gamma \neq 1$ or $\sigma \neq 1$ then

$$\frac{1}{2E} U_{\gamma i}^*(V_a)_{\gamma\sigma} U_{\sigma j} = \frac{a}{2E} U_{1i}^* U_{1j}. \tag{1.103}$$

Therefore

$$U_{\gamma i}^*(H_1)_{\gamma\sigma} U_{\sigma j} = \frac{\Delta m_{21}^2}{2E} \delta_{2i} \delta_{2j} + \frac{a}{2E} U_{1i}^* U_{1j}, \tag{1.104}$$

and

$$X_{ij} = U_{\beta i} U_{\gamma i}^*(H_1)_{\gamma\sigma} U_{\sigma j} U_{\alpha j}^*$$
$$= U_{\beta i} \left[\frac{\Delta m_{21}^2}{2E} \delta_{2i} \delta_{2j} + \frac{a}{2E} U_{1i}^* U_{1j} \right] U_{\alpha j}^*$$
$$= \frac{\Delta m_{21}^2}{2E} U_{\beta i} U_{\alpha j}^* \delta_{2i} \delta_{2j} + \frac{a}{2E} U_{\beta i} U_{1i}^* U_{1j} U_{\alpha j}^*. \tag{1.105}$$

The Y_{ij} integral is

$$Y_{11} = Y_{12} = Y_{21} = Y_{22} = x, \tag{1.106}$$

$$Y_{13} = Y_{23} = Y_{31} = Y_{32} = \left(-i\frac{\Delta m_{31}^2}{2E} \right)^{-1} \left(e^{-i\frac{\Delta m_{31}^2 x}{2E}} - 1 \right), \tag{1.107}$$

$$Y_{33} = xe^{-i\frac{\Delta m_{31}^2 x}{2E}}. \tag{1.108}$$

In general

$$Y_{ij} = (1-\delta_{i3})(1-\delta_{j3})x + \delta_{i3}\delta_{j3}xe^{-i\frac{\Delta m_{31}^2 x}{2E}} \tag{1.109}$$
$$+ [(1-\delta_{i3})\delta_{j3} + \delta_{i3}(1-\delta_{j3})] \left(-i\frac{\Delta m_{31}^2}{2E} \right)^{-1} \left(e^{-i\frac{\Delta m_{31}^2 x}{2E}} - 1 \right).$$

Inserting (1.109) and (1.105) into (1.96), we get

$$
\begin{aligned}
(S_1(x))_{\beta\alpha} &= -i\frac{ax}{2E}e^{-i\frac{\Delta m_{31}^2 x}{2E}}U_{\beta 3}U_{\alpha 3}^*|U_{13}|^2 \\
&\quad -ix\left[\frac{\Delta m_{21}^2}{2E}U_{\beta 2}U_{\alpha 2}^* + \frac{a}{2E}(U_{\beta 1}U_{11}^*U_{11}U_{\alpha 1}^* + U_{\beta 1}U_{11}^*U_{12}U_{\alpha 2}^* \right. \\
&\quad \left. +U_{\beta 2}U_{12}^*U_{11}U_{\alpha 1}^* + U_{\beta 2}U_{12}^*U_{12}U_{\alpha 2}^*)\right] \\
&\quad -i\left(-i\frac{\Delta m_{31}^2}{2E}\right)^{-1}\left(e^{-i\frac{\Delta m_{31}^2 x}{2E}} - 1\right)\frac{a}{2E}(U_{\beta 1}U_{11}^*U_{13}U_{\alpha 3}^* + U_{\beta 2}U_{12}^*U_{13}U_{\alpha 3}^* \\
&\quad +U_{\beta 3}U_{13}^*U_{11}U_{\alpha 1}^* + U_{\beta 3}U_{13}^*U_{12}U_{\alpha 2}^*). \quad (1.110)
\end{aligned}
$$

Note that $\sum_{k=1}^2 U_{\alpha k}^* U_{1k} = \delta_{\alpha 1} - U_{\alpha 3}^* U_{13}$. We now can calculate the factors that are relevant to matrix elements as follows

$$
\begin{aligned}
&U_{\beta 1}U_{11}^*U_{11}U_{\alpha 1}^* + U_{\beta 1}U_{11}^*U_{12}U_{\alpha 2}^* + U_{\beta 2}U_{12}^*U_{11}U_{\alpha 1}^* + U_{\beta 2}U_{12}^*U_{12}U_{\alpha 2}^* \\
&= (U_{\beta 1}U_{11}^* + U_{\beta 2}U_{12}^*)(U_{11}U_{\alpha 1}^* + U_{12}U_{\alpha 2}^*) \\
&= (\delta_{\beta 1} - U_{\beta 3}U_{13}^*)(\delta_{\alpha 1} - U_{13}U_{\alpha 3}^*) \\
&= \delta_{\alpha 1}\delta_{\beta 1} - \delta_{\alpha 1}U_{\beta 3}U_{13}^* - \delta_{\beta 1}U_{13}U_{\alpha 3}^* + U_{\beta 3}U_{\alpha 3}^*|U_{13}|^2 \\
&= \delta_{\alpha 1}\delta_{\beta 1} + U_{\beta 3}U_{\alpha 3}^*(|U_{13}|^2 - \delta_{\alpha 1} - \delta_{\beta 1}), \quad (1.111)
\end{aligned}
$$

and

$$
\begin{aligned}
&U_{\beta 1}U_{11}^*U_{13}U_{\alpha 3}^* + U_{\beta 2}U_{12}^*U_{13}U_{\alpha 3}^* + U_{\beta 3}U_{13}^*U_{11}U_{\alpha 1}^* + U_{\beta 3}U_{13}^*U_{12}U_{\alpha 2}^* \\
&= U_{13}U_{\alpha 3}^*(\delta_{\beta 1} - U_{\beta 3}U_{13}^*) + U_{\beta 3}U_{13}^*(\delta_{\alpha 1} - U_{13}U_{\alpha 3}^*) \\
&= \delta_{\alpha 1}U_{\beta 3}U_{13}^* + \delta_{\beta 1}U_{13}U_{\alpha 3}^* - 2U_{\beta 3}U_{\alpha 3}^*|U_{13}|^2 \\
&= U_{\beta 3}U_{\alpha 3}^*(\delta_{\alpha 1} + \delta_{\beta 1} - 2|U_{13}|^2). \quad (1.112)
\end{aligned}
$$

Therefore

$$
\begin{aligned}
(S_1(x))_{\beta\alpha} &= -i\frac{ax}{2E}e^{-i\frac{\Delta m_{31}^2 x}{2E}}U_{\beta 3}U_{\alpha 3}^*|U_{13}|^2 \\
&\quad -i\frac{x}{2E}\left[\Delta m_{21}^2 U_{\beta 2}U_{\alpha 2}^* + a(\delta_{\alpha 1}\delta_{\beta 1} + U_{\beta 3}U_{\alpha 3}^*(|U_{13}|^2 - \delta_{\alpha 1} - \delta_{\beta 1}))\right] \\
&\quad -\frac{a}{\Delta m_{31}^2}\left(e^{-i\frac{\Delta m_{31}^2 x}{2E}} - 1\right)(2|U_{13}|^2 - \delta_{\alpha 1} - \delta_{\beta 1})U_{\beta 3}U_{\alpha 3}^*. \quad (1.113)
\end{aligned}
$$

From (1.113) and (1.96) we get

$$
\begin{aligned}
&(S(x))_{\beta\alpha} = (S_0(x))_{\beta\alpha} + (S_1(x))_{\beta\alpha} \\
&= \delta_{\alpha\beta} + U_{\beta 3}U_{\alpha 3}^*\left(e^{-i\frac{\Delta m_{31}^2 x}{2E}} - 1\right) - \frac{a}{\Delta m_{31}^2}\left(e^{-i\frac{\Delta m_{31}^2 x}{2E}} - 1\right)(2|U_{13}|^2 - \delta_{\alpha 1} - \delta_{\beta 1})U_{\beta 3}U_{\alpha 3}^* \\
&\quad -i\frac{ax}{2E}e^{-i\frac{\Delta m_{31}^2 x}{2E}}U_{\beta 3}U_{\alpha 3}^*|U_{13}|^2 + \left(i\frac{ax}{2E}U_{\beta 3}U_{\alpha 3}^*|U_{13}|^2 - i\frac{ax}{2E}U_{\beta 3}U_{\alpha 3}^*|U_{13}|^2\right) \\
&\quad -i\frac{\Delta m_{31}^2 x}{2E}\left[\frac{\Delta m_{21}^2}{\Delta m_{31}^2}U_{\beta 2}U_{\alpha 2}^* + \frac{a}{\Delta m_{31}^2}(\delta_{\alpha 1}\delta_{\beta 1} + U_{\beta 3}U_{\alpha 3}^*(|U_{13}|^2 - \delta_{\alpha 1} - \delta_{\beta 1}))\right]. \quad (1.114)
\end{aligned}
$$

By rearranging the common terms and note that $\sin X/2 = \frac{e^{iX/2} - e^{-iX/2}}{2i}$ with $X = \frac{\Delta m_{31}^2}{2E}$,

the above equation becomes

$$
\begin{aligned}
(S(x))_{\beta\alpha} &= \delta_{\alpha\beta} - i2e^{-i\Delta_{31}}\sin\Delta_{31}U_{\beta3}U_{\alpha3}^*\left[(1-C) - \frac{iax}{2E}|U_{13}|^2\right]\\
&\quad - i2\Delta_{31}\left[\epsilon U_{\beta2}U_{\alpha2}^* + \frac{a}{\Delta m_{31}^2}\delta_{\alpha1}\delta_{\beta1} + CU_{\beta3}U_{\alpha3}^*\right]\\
&= \delta_{\alpha\beta} + A + B,
\end{aligned}
\tag{1.115}
$$

where $\Delta_{31} = \frac{\Delta m_{31}^2 x}{4E}$; $\epsilon = \frac{\Delta m_{21}^2}{\Delta m_{31}^2}$ and $C = \frac{a}{\Delta m_{31}^2}(2|U_{13}|^2 - \delta_{\alpha1} - \delta_{\beta1})$. The oscillation probability now can be calculated

$$
\begin{aligned}
P(\nu_\alpha \to \nu_\beta) &= |(S(x))_{\beta\alpha}|^2\\
&= \delta_{\alpha\beta}(1 + A + A^* + B + B^*) + AA^* + BB^* + A^*B + AB^* \tag{1.116}
\end{aligned}
$$

• The tearm which is relevant to $\delta_{\alpha\beta}$

$$
\begin{aligned}
&\delta_{\alpha\beta}(1 + A + A^* + B + B^*)\\
&= \delta_{\alpha\beta}\left\{1 - i2e^{-i\Delta_{31}}\sin\Delta_{31}U_{\beta3}U_{\alpha3}^*\left[(1-C) - \frac{iax}{2E}|U_{13}|^2\right]\right.\\
&\quad + i2e^{i\Delta_{31}}\sin\Delta_{31}U_{\beta3}^*U_{\alpha3}\left[(1-C) + \frac{iax}{2E}|U_{13}|^2\right]\\
&\quad - i2\Delta_{31}\left[\epsilon U_{\beta2}U_{\alpha2}^* + \frac{a}{\Delta m_{31}^2}\delta_{\alpha1}\delta_{\beta1} + CU_{\beta3}U_{\alpha3}^*\right]\\
&\quad \left. + i2\Delta_{31}\left[\epsilon U_{\beta2}^*U_{\alpha2} + \frac{a}{\Delta m_{31}^2}\delta_{\alpha1}\delta_{\beta1} + CU_{\beta3}^*U_{\alpha3}\right]\right\}\\
&= \delta_{\alpha\beta}\left[1 - 4(1-C)|U_{\alpha3}|^2\sin^2\Delta_{31} - \frac{ax}{E}|U_{\alpha3}|^2|U_{13}|^2\sin2\Delta_{31}\right] \tag{1.117}\\
&= \delta_{\alpha\beta}\left[1 - 4|U_{\alpha3}|^2\sin^2\Delta_{31}\left(1 - \frac{2a}{\Delta m_{31}^2}(|U_{13}|^2 - \delta_{\alpha1})\right) - \frac{ax}{E}|U_{\alpha3}|^2|U_{13}|^2\sin2\Delta_{31}\right].
\end{aligned}
$$

• In order to calculate the tearm which is irrelevant to $\delta_{\alpha\beta}$, we first calculate its

components

$$AA^* = 4\sin^2\Delta_{31}|U_{\beta3}|^2|U_{\alpha3}|^2\left[(1-2C+C^2)+\left(\frac{ax}{2E}\right)^2|U_{13}|^4\right] \tag{1.118}$$

$$\begin{aligned}
BB^* = {} & 4(\Delta_{31})^2\left[\epsilon^2|U_{\beta2}|^2|U_{\alpha2}|^2+\epsilon\frac{2a}{\Delta m_{31}^2}|U_{13}|^2\delta_{\alpha1}\delta_{\beta1}\right.\\
& +2\epsilon C.Re(U_{\beta3}^*U_{\alpha3}U_{\beta2}U_{\alpha2}^*)+C^2|U_{\beta3}|^2|U_{\alpha3}|^2\\
& \left.+\frac{2aC}{\Delta m_{31}^2}|U_{13}|^2\delta_{\alpha1}\delta_{\beta1}+\left(\frac{a}{\Delta m_{31}^2}\right)^2\right],
\end{aligned} \tag{1.119}$$

$$\begin{aligned}
A^*B+AB^* = {} & 2Re(AB^*)\\
= {} & 4\epsilon(1-C)\Delta_{31}\sin2\Delta_{31}Re(U_{\beta3}^*U_{\alpha3}U_{\beta2}U_{\alpha2}^*)\\
& -8\epsilon(1-C)\Delta_{31}\sin^2\Delta_{31}Im(U_{\beta3}^*U_{\alpha3}U_{\beta2}U_{\alpha2}^*)\\
& -8\epsilon\left(\frac{ax}{2E}\right)\Delta_{31}\sin^2\Delta_{31}|U_{13}|^2Re(U_{\beta3}^*U_{\alpha3}U_{\beta2}U_{\alpha2}^*)\\
& -4\epsilon\left(\frac{ax}{2E}\right)\Delta_{31}\sin^2\Delta_{31}|U_{13}|^2Im(U_{\beta3}^*U_{\alpha3}U_{\beta2}U_{\alpha2}^*)\\
& +4(1-C)\frac{a}{\Delta m_{31}^2}\Delta_{31}\sin2\Delta_{31}|U_{13}|^2\delta_{\alpha1}\delta_{\beta1}\\
& -8\frac{a^2x}{2E\Delta m_{31}^2}\Delta_{31}\sin^2\Delta_{31}|U_{13}|^2\delta_{\alpha1}\delta_{\beta1}\\
& +4(1-C)C\Delta_{31}\sin2\Delta_{31}|U_{\beta3}|^2|U_{\alpha3}|^2\\
& -8\left(\frac{axC}{2E}\right)\Delta_{31}\sin^2\Delta_{31}|U_{13}|^2|U_{\beta3}|^2|U_{\alpha3}|^2.
\end{aligned} \tag{1.120}$$

Since $C\propto a\sim\mathcal{O}(10^{-5})$, $\epsilon\Delta_{31}=\Delta_{21}=\frac{\Delta m_{21}^2}{4E}\sim\mathcal{O}(10^{-5})$, we therefore can neglect all the terms that contain $a^2,C^2,aC,\epsilon a,\epsilon C,\epsilon C\Delta_{31}$, and $\epsilon a\Delta_{31}$, leaving

$$AA^* = 4\sin^2\Delta_{31}|U_{\beta3}|^2|U_{\alpha3}|^2\left[1-2\frac{a}{\Delta m_{31}^2}(2|U_{13}|^2-\delta_{\alpha1}-\delta_{\beta1})\right] \tag{1.121}$$

$$BB^* = 4\Delta_{21}^2|U_{\beta2}|^2|U_{\alpha2}|^2, \tag{1.122}$$

$$\begin{aligned}
A^*B+AB^* = {} & 2Re(AB^*)\\
= {} & 4\Delta_{21}\sin2\Delta_{31}Re(U_{\beta3}^*U_{\alpha3}U_{\beta2}U_{\alpha2}^*)\\
& -8\Delta_{21}\sin^2\Delta_{31}Im(U_{\beta3}^*U_{\alpha3}U_{\beta2}U_{\alpha2}^*)\\
& +4\frac{ax}{4E}\sin2\Delta_{31}|U_{13}|^2\delta_{\alpha1}\delta_{\beta1}\\
& +4\frac{ax}{4E}\sin2\Delta_{31}|U_{\beta3}|^2|U_{\alpha3}|^2(2|U_{13}|^2-\delta_{\alpha1}-\delta_{\beta1}).
\end{aligned} \tag{1.123}$$

Finally, up to the first order perturbations of a and Δm_{21}^2, we get the general form of

oscillation probability

$$
\begin{aligned}
P(\nu_\alpha \to \nu_\beta) &= \delta_{\alpha\beta}(1 + A + A^* + B + B^*) + AA^* + BB^* + A^*B + AB^* \\
&\approx \delta_{\alpha\beta}\left\{ 1 - 4|U_{\alpha3}|^2 \sin^2 \Delta_{31}\left[1 - \frac{2a}{\Delta m_{31}^2}\left(|U_{13}|^2 - \delta_{\alpha1}\right)\right]\right. \\
&\quad \left. - \frac{ax}{E}|U_{\alpha3}|^2 |U_{13}|^2 \sin 2\Delta_{31}\right\} \\
&\quad + 4\sin^2 \Delta_{31}|U_{\beta3}|^2|U_{\alpha3}|^2\left[1 - 2\frac{a}{\Delta m_{31}^2}(2|U_{13}|^2 - \delta_{\alpha1} - \delta_{\beta1})\right] \\
&\quad - 8\Delta_{21}\sin^2\Delta_{31} Im(U_{\beta3}^* U_{\alpha3} U_{\beta2} U_{\alpha2}^*) \\
&\quad + 4\Delta_{21}\sin 2\Delta_{31} Re(U_{\beta3}^* U_{\alpha3} U_{\beta2} U_{\alpha2}^*) \\
&\quad + \frac{ax}{E}\sin 2\Delta_{31}\left(|U_{13}|^2\delta_{\alpha1}\delta_{\beta1} + |U_{\beta3}|^2|U_{\alpha3}|^2(2|U_{13}|^2 - \delta_{\alpha1} - \delta_{\beta1})\right).
\end{aligned}
\tag{1.124}
$$

For anti-neutrino, $P(\bar{\nu}_\alpha \to \bar{\nu}_\beta)$ can be obtained from Eq.(1.124) by taking complex conjugate of the matrix element product and replacing $a \to -a$.

Survival probability $P(\nu_\mu \to \nu_\mu)$ in matter

For $\alpha = \beta = \mu$ we have

$$
\begin{aligned}
P(\nu_\mu \to \nu_\mu) &\approx 1 + 4\sin^2 \Delta_{31}|U_{\mu3}|^2\left[(|U_{\mu3}|^2 - 1) - \frac{2a}{\Delta m_{31}^2}|U_{e3}|^2\left(2|U_{\mu3}|^2 - 1\right)\right] \\
&\quad + 4\Delta_{31}\sin 2\Delta_{31}|U_{\mu3}|^2\left[\frac{\Delta m_{21}^2}{\Delta m_{31}^2}|U_{\mu2}|^2 + \frac{a}{\Delta m_{31}^2}|U_{e3}|^2\left(2|U_{\mu3}|^2 - 1\right)\right].
\end{aligned}
\tag{1.125}
$$

Inserting the PMNS matrix elements $U_{e2} = s_{12}c_{13}$, $U_{e3} = s_{13}e^{-i\delta}$, $U_{\mu2} = c_{12}c_{23} - s_{12}s_{13}s_{23}e^{i\delta}$, $U_{\mu3} = s_{23}c_{13}$ into the above equation, we get

$$
\begin{aligned}
P(\nu_\mu \to \nu_\mu) &\approx 1 + 4s_{23}^2 c_{13}^2(s_{23}^2 c_{13}^2 - 1)\sin^2 \Delta_{31} \\
&\quad + 4s_{23}^2 c_{13}^2 s_{13}^2\left(2s_{23}^2 c_{13}^2 - 1\right)\frac{2a}{\Delta m_{31}^2}\sin^2 \Delta_{31} \\
&\quad + 4s_{23}^2 c_{13}^2 s_{13}^2\left(2s_{23}^2 c_{13}^2 - 1\right)\frac{a}{\Delta m_{31}^2}\Delta_{31}\sin 2\Delta_{31} \\
&\quad + 4s_{23}^2 c_{13}^2(c_{12}^2 c_{23}^2 + s_{12}^2 s_{13}^2 s_{23}^2 - 2s_{12}s_{13}s_{23}c_{12}c_{23}\cos\delta)\Delta_{21}\sin 2\Delta_{31}.
\end{aligned}
\tag{1.126}
$$

Transition probability $P(\nu_\mu \to \nu_e)$ in matter

For $\alpha = \mu$ and $\beta = e$ we have

$$
\begin{aligned}
P(\nu_\mu \to \nu_e) &\approx 4\sin^2 \Delta_{31}|U_{e3}|^2|U_{\mu3}|^2 \\
&\quad - 8\sin^2 \Delta_{31}|U_{e3}|^2|U_{\mu3}|^2\frac{a}{\Delta m_{31}^2}(2|U_{e3}|^2 - 1) \\
&\quad + 4\sin 2\Delta_{31}\frac{ax}{4E}|U_{e3}|^2|U_{\mu3}|^2(2|U_{e3}|^2 - 1) \\
&\quad - 8\Delta_{21}\sin^2 \Delta_{31} Im(U_{e3}^* U_{\mu3} U_{e2} U_{\mu2}^*) \\
&\quad + 4\Delta_{21}\sin 2\Delta_{31} Re(U_{e3}^* U_{\mu3} U_{e2} U_{\mu2}^*).
\end{aligned}
\tag{1.127}
$$

Substituting the PMNS matrix elements $U_{e2} = s_{12}c_{13}$, $U_{e3} = s_{13}e^{-i\delta}$, $U_{\mu2} = c_{12}c_{23} - s_{12}s_{13}s_{23}e^{i\delta}$, $U_{\mu3} = s_{23}c_{13}$ into the above equation and making an approximation $\Delta_{21} \approx \sin\Delta_{21}$ for $\Delta_{21} \ll 1$, we get the approximation transition probability as follows

$$
\begin{aligned}
P(\nu_\mu \to \nu_e) \approx\ & 4s_{13}^2 s_{23}^2 c_{13}^2 \sin^2\Delta_{31} \\
& -8s_{13}^2 s_{23}^2 c_{13}^2 \frac{a}{\Delta m_{31}^2}(2s_{13}^2 - 1)\sin^2\Delta_{31} \\
& +4s_{13}^2 s_{23}^2 c_{13}^2 \frac{ax}{4E}(2s_{13}^2 - 1)\sin 2\Delta_{31} \\
& -8s_{12}s_{13}s_{23}c_{12}c_{13}^2 c_{23}\sin\delta\sin\Delta_{21}\sin^2\Delta_{31} \\
& +4s_{12}s_{13}s_{23}c_{13}^2(c_{12}c_{23}\cos\delta - s_{12}s_{13}s_{23})\sin\Delta_{21}\sin 2\Delta_{31}.
\end{aligned}
\tag{1.128}
$$

where $\Delta_{ij} = \frac{\Delta m_{ij}^2 L}{4E}$, and $a = 2\sqrt{2}EG_F N_e = 7.56 \times 10^{-5}[eV^2](\frac{\rho}{g/cm^3})(\frac{E}{GeV})$, N_e is the electron density of the matter, and ρ is the density of the matter. For antineutrino, $P(\bar{\nu}_\mu \to \bar{\nu}_e)$ can be obtained from Eq.(1.128) by replacing $\delta \to -\delta$ and $a \to -a$. In Eqs. (1.126) and (1.128), the first term dominates. The terms which contain a constant present matter effect. The terms proportional to $\sin\delta$ are called *CP-violating* since their contributions for total probability are opposite for neutrino and antineutrino. And finally, the ones contain $\cos\delta$ are called *CP-conserving term* since their contributions are the same for neutrino and antineutrino. Fig. 1.4 shows the oscillation probabilities of $\nu_\mu \to \nu_e$ and $\bar{\nu}_\mu \to \bar{\nu}_e$ as functions of neutrino energy at different true values of δ for T2K baseline $L = 295$ km (left) and NOνA baseline $L = 810$ km (right), respectively. In the figure, the differences between solid and dashed blue lines indicate the matter effect, and the differences between solid and dashed red lines show the combined effects of both matter and CP-violation. For more intuitively illustrating of the matter effect, it is convenient to express CP asymmetry in terms of relative difference between $P(\nu_\mu \to \nu_e)$ and $P(\bar{\nu}_\mu \to \bar{\nu}_e)$ near the oscillation maximum $\left(\frac{|\Delta m_{31}^2|L}{4E_\nu} = \pi/2\right)$ [43]

$$
\begin{aligned}
A_{\text{CP}}\left(\frac{|\Delta m_{31}^2|L}{4E_\nu} = \pi/2\right) &= \frac{P(\nu_\mu \to \nu_e) - P(\bar{\nu}_\mu \to \bar{\nu}_e)}{P(\nu_\mu \to \nu_e) + P(\bar{\nu}_\mu \to \bar{\nu}_e)} \\
&\sim -\frac{\pi\sin 2\theta_{12}}{\tan\theta_{23}\sin 2\theta_{13}}\frac{\Delta m_{21}^2}{|\Delta m_{31}^2|}\sin\delta_{\text{CP}} \pm \frac{L}{2800km},
\end{aligned}
\tag{1.129}
$$

where $+(-)$ sign is taken for the *neutrino (antineutrino)*, respectively. With the values listed in Table 3.1, we find that the δ_{CP}-dependent true CP asymmetry is $\frac{\pi\sin 2\theta_{12}}{\tan\theta_{23}\sin 2\theta_{13}}\frac{\Delta m_{21}^2}{|\Delta m_{31}^2|}\sin\delta_{\text{CP}} \sim 0.256\sin\delta_{\text{CP}}$, which means the CP violation effect can be observed somewhat between -25.6% and $+25.6\%$. For a 295km baseline of the T2K experiment, the matter effect which causes fake CP asymmetry is subdominant with $\sim 10.5\%$. For NOνA with a baseline of 810km, the effect is even larger, $\sim 28.9\%$. Fig. 1.5 shows CP asymmetry versus δ_{CP} with contribution of matter effect. We can see that $A_{\text{CP}} \neq 0$ even at CP conserving values $\delta_{\text{CP}} = (0, \pi)$.
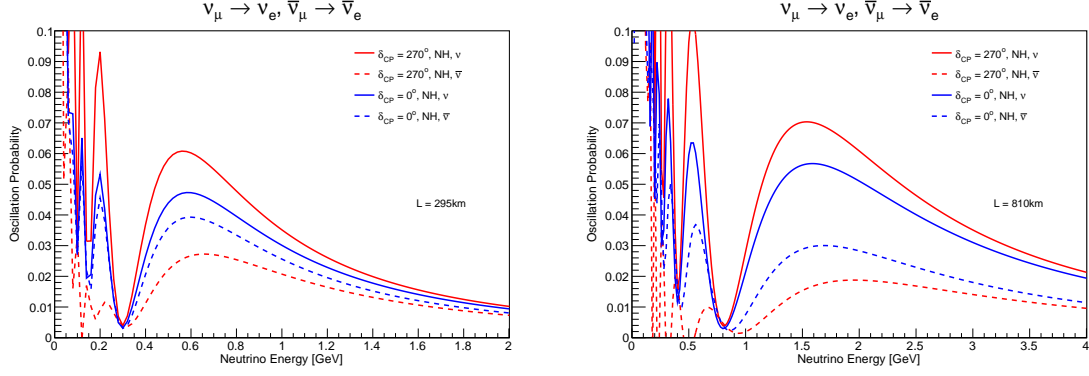
Figure 1.4:   The transition probabilities $\nu_\mu \to \nu_e$ and $\bar{\nu}_\mu \to \bar{\nu}_e$ for T2K baseline (left) and NOνA baseline (right).
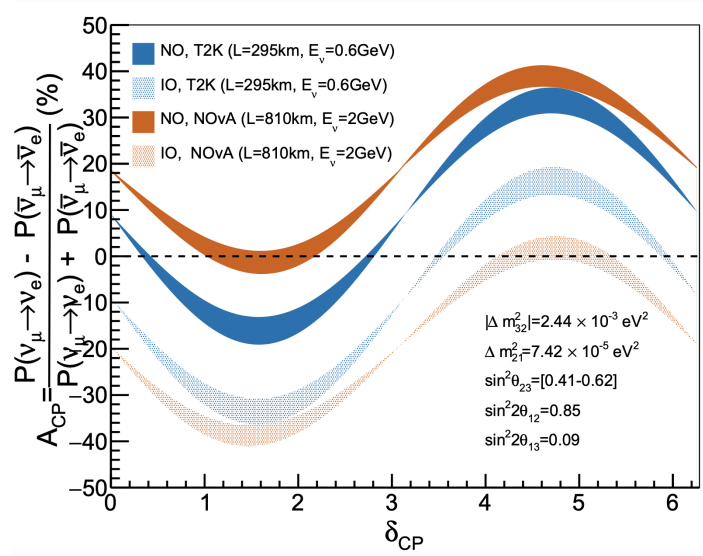
Figure 1.5:   The relative CP asymmetry as a function of δ_{CP}, the solid band indicates the uncertainty of θ_{23}. The plot is taken from Ref. [7].

1.2 Introduction to some neutrino oscillation experiments

Accelerator-based long baseline and reactor-based neutrino experiments have played a crucial role in oscillation studies. The accelerator-based experiments normally consist of three main parts: accelerator complex, near detector(s), and far detector(s). Because neutrinos interact weakly with matter, to have enough statistics for oscillation study, the accelerator complex is used to generate very intense neutrino beams. Unoscillated neutrinos are measured by the near detector(s) to monitor component, fraction and direction of the beam before sending to the far detector(s). During the propagation, a specific flavor of neutrino may oscillate into the others and will be detected at the far detector(s). The oscillation parameters are extracted by comparing information between the near(s) and far detector(s).

The reactor-based experiments use electron antineutrino ($\overline{\nu}_e$) flux from nuclear power plants to study neutrino oscillation. The $\overline{\nu}_e$ flux mainly comes from four isotopes ^{235}U, ^{238}U, ^{239}Pu, and ^{241}Pu.

In this section, we will describe the Tokai to Kamioka (T2K), NuMI Off-axis ν_e Appearance (NOvA), and Jiangmen Underground Neutrino Observatory (JUNO) experiments. T2K and NOνA are the two on-going off-axis accelerator-based long baseline neutrino oscillation experiments, while JUNO is a reactor-based experiment.

1.2.1 The T2K experiment

T2K is located in Japan. Its muon (anti-)neutrino beam is produced by 500 kW Japan Proton Accelerator Research Complex (J-PARC). T2K has three near detectors placed at 280 m downstream from the target including INGRID, ND280, and WAGASCI BabyMIND. The on-axis near detector Interactive Neutrino GRID (INGRID) controls direction, stability and profile of the neutrino beam. The ND280, which is placed at 2.5° off-axis, will measure muon (anti-)neutrino flux, cross section and intrinsic electron (anti-)neutrino backgrounds. The WAter Grid SCIntillator Detector – prototype Magnetized Iron Neutrino Detector (WAGASCI BabyMIND) is located at 1.5° off-axis in the near detector hall inside J-PARC. The main goal of the WAGASCI BabyMIND is to precisely measure neutrino interactions with water (H_2O) and hydrocarbon (CH). T2K has one far detector, Super-K, which is situated in Kamioka, 295 km from the neutrino source. The off-axis angle of 2.5° of the Super-K position is to expose a narrow band beam of neutrinos at a 0.6 GeV maximum peak. A schematic of the T2K experiment is described in Fig. 1.6. In the first phase of the operation from 2010 to 2021, T2K observed for the first time the appearance of electron neutrino from the muon neutrino beam $\nu_\mu \rightarrow \nu_e$ [44] [45] and gave the first hint on CP violation in the lepton sector [18].

T2K-II: T2K-II [46] is a proposal to extend the T2K run until 2027 before Hyper-Kamiokande (HK) [47] starts operation. T2K originally planned to take data
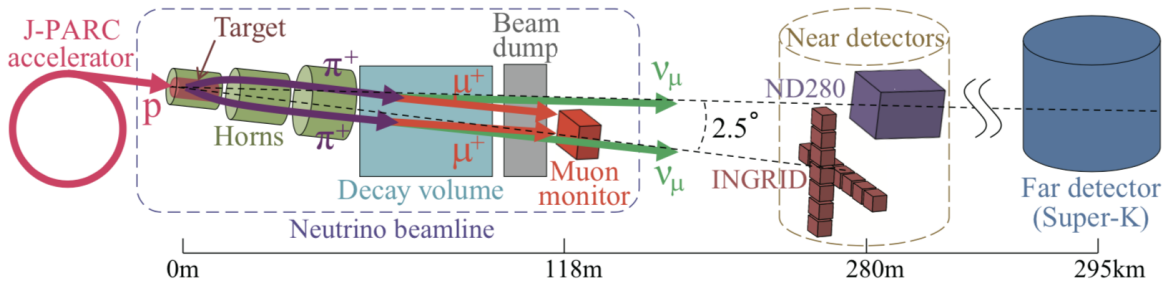
Figure 1.6: Schematic diagram of the T2K experiment.

equivalent to 7.8×10^{21} protons-on-target (POT) exposure. In Neutrino 2020 conference, T2K reported a collected data sample from 3.6×10^{21} POT exposure [48]. T2K-II proposes to collect 20×10^{21} POT, allowing it to explore CP violation with a confidence level of 3σ or higher if δ_{CP} is close to $-\pi/2$ [46]. The main goals of T2K-II are:

- Searching for CP violation in the lepton sector.
- Searching for sterile neutrino.
- Precise measurement of the oscillation parameters Δm^2_{31} and θ_{23}.
- Precise measurement of the neutrino-nucleus interactions on water, hydrocarbon and iron.

1.2.2 The NOvA experiment

Ongoing NOvA [49] is also the 2nd generation of accelerator-based long baseline neutrino experiments placed in the US with a baseline of 810 km between the production source and the far detector. Such a long baseline allows NOvA to explore the neutrino mass hierarchy (MH) with high sensitivity via the matter effect [50] on the (anti-)neutrino interactions. From Eq. 1.129, it can be estimated that the matter effect in NOvA is $\sim 28.9\%$, which is slightly higher than the CP violation effect. Similar to T2K, NOvA adopts the off-axis technique such that the far detector is placed at an angle of 14 mrad to the averaged direction of the neutrino beam. NOvA uses a near detector, located 1 km away from the production target, to characterize the unoscillated neutrino flux. The NOvA far detector is filled with liquid scintillator contained in PVC cells, totally weighted up to 14 ktons with 63% active materials. NOvA takes advantage of machine learning for particle classification to enhance the event selection performance. In 2018, NOvA provided more than 4σ C.L. evidence of electron anti-neutrino appearance from a beam of muon anti-neutrinos [51]. At the Neutrino 2020 conference, NOvA reported a collected data sample of 2.6×10^{21} POT exposure [52]. In Ref. [53], NOvA gives a prospect of extending the run through 2024 (NOvA-II), in order to get 3σ C.L. or higher sensitivity to the MH in case the MH is *normal* and δ_{CP} is close to $-\pi/2$, and more than 2σ C.L. sensitivity to CP violation.

1.2.3 The JUNO experiment

JUNO [11] is a reactor-based medium-baseline neutrino experiment located in China. JUNO houses a 20 kton large liquid scintillator detector for detecting the electron anti-neutrinos ($\overline{\nu}_e$) from the Yangjiang (YJ) and Taishan (TS) nuclear power plants (NPPs) with an average baseline of 52.5 km. Each of the six cores at YJ nuclear plant will produce a power of 2.9 GW and the four cores at TS NPP will generate 4.6 GW each. They are combined to give 36 GW thermal power. JUNO primarily aims to determine the MH by measuring the surviving $\overline{\nu}_e$ spectrum, which uniquely displays the oscillation patterns driven by both solar and atmospheric neutrino mass-squared splittings [54]. This feature can be understood via the $\bar{\nu}_e$ disappearance probability in vacuum expressed in equation (1.65).

An averaged 52 km baseline of the JUNO experiment is to obtain the maximum oscillation corresponding to $\Delta_{21} = \pi/2$ around 3 MeV, and relatively enhances the oscillation patterns driven by Δ_{31} and Δ_{32} terms. The relatively small difference between Δm_{31}^2 and Δm_{32}^2 make oscillation patterns in the *normal* and *inverted* MH scenarios distinguishable. To realize practically the capability of mass hierarchy resolution, JUNO must achieve a very good neutrino energy resolution, which has been demonstrated recently in Ref. [55], and collect a huge amount of data. With six years of operation, JUNO can reach 3σ C. L. or higher sensitivity to the MH and achieve better than 1% precision on the solar neutrino parameters and the atmospheric neutrino mass-squared splitting $|\Delta m_{31}^2|$.

Chapter 2. Measurements at INGRID - the T2K on-axis near detector

The INGRID is an on-axis near detector of the T2K experiment. The detector consists of 14 identical modules arranged in a cross section of $10m \times 10m$ as shown in Fig. 2.1. This configuration is to ensure that the neutrino beam profile at IN-GRID is fully covered within 1σ spatial width. Each basic module is made from nine $124cm \times 124cm \times 6.5cm$ iron plates and eleven $120cm \times 120cm \times 1.0cm$ scintillator trackers of sandwich structure. The scintillator tracker has two scintillator layers placed perpendicular to each other. Each layer includes 24 scintillator bars. In order to prevent the wrong signal of charged particles coming from outside of the module, every basic module is covered by six VETO scintillator planes, which consist of 22 scintillator bars.

Light coming from neutrino interaction inside the detector module is collected by scintillators and transported by wavelength shifting fibers. The light is then read out by Multi-Pixel Photon Counter (MPPC) which are attached at the end of the wavelength shifting fibers.

The INGRID detector has an important role in the T2K experiment. It has monitored the neutrino beam direction, stability, and profile. Currently, the magnetic horn current is being upgraded from 250 kA to 320 kA. The more current is applied to the horns, the more intense the neutrino beam will be. In this section, we will present some results of our simulation and basic measurements at the INGRID detector. The simulation programs are described as shown in Fig. 2.2. In which, we use JNUBEAM [56] (version 13a v1.1) to predict neutrino flux, NEUT [57–59] (version 3.5.2) to study neutrino interaction with matter, and GEANT4 [60] (version 9.2.01.00, physics list: QGSP_BERT) to simulate detector response.

2.1 Neutrino flux prediction

The T2K experiment has a plan to run up to 2027 with a total exposure of 10^{22} protons-on-target (POT). Base on the fact that statistical uncertainty of the flux is about 10% [8], for further study we generate 1100 MC files with 10^{21} POT in each file. We investigate both neutrino mode (FHC) and anti-neutrino mode (RHC) to produce fluxes at different configurations of horn operation:

- On-axis, 0kA.
- On-axis, $\pm$ 250kA.
- On-axis, $\pm$ 320kA.
- Off-axis, $\pm$ 320kA.

The simulation process is as follows. First, we create 1100 MC files which
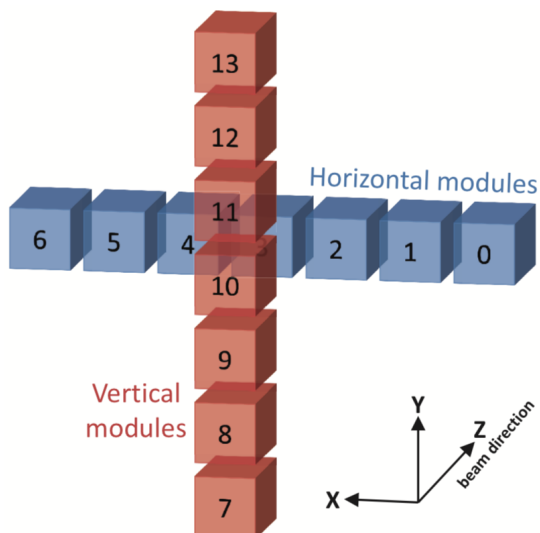
Figure 2.1: The schematic view of INGRID detector.
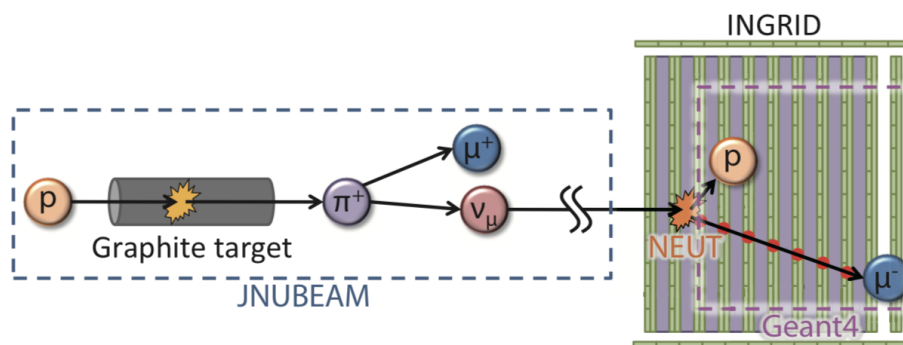
Figure 2.2: INGRID MC simulation programs, taken from Ref. [8].
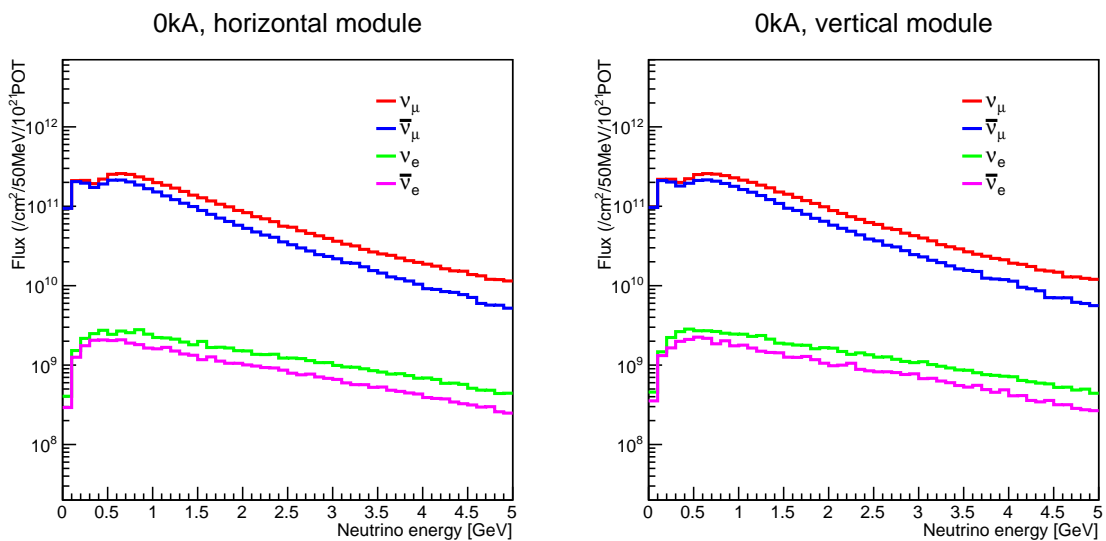
Figure 2.3: Neutrino fluxes at INGRID without horn current applied.

contain information about the interaction of a 30 GeV proton beam with a graphite target by FLUKA 2011.2 [61–63]. Then the products, including neutrino parents and their decays, are simulated by JNUBEAM. The flux is finally provided after tuning based on hadronic production data from the NA61/SHINE experiment [64–66].

JNUBEAM [56] is a neutrino beam Monte Carlo simulation package based on the GEANT3 tool [60]. It allows us to replicate the second beamline geometry, including the baffle, target, three horn magnets, decay volume, beam dump, and muon monitor. The near detectors (NDs) are positioned according to the latest survey results. The neutrino parents ($\pi^{\pm}$, $K^{\pm}$, K^o_L and $\mu^{\pm}$) after proton-target collision are focused by horn magnetic fields and tracked into decay volume. These particles then decay into neutrinos or are absorbed into the material. All the information about neutrinos and their parents is recorded in the direction of ND and Super-K, including flavor, energy, and tracking.

The fluxes of different configurations of horn operation are shown from Fig. 2.3 to Fig. 2.8. Our study shows that without horn current applied (see Fig. 2.3), the neutrinos and anti-neutrinos are approximately equally produced. This means that the backgrounds are too high, leading to a large uncertainty in measurements. From the Fig. 2.4 - 2.8, we clearly see the separations between neutrino channels. Therefore, by applying the current to the horns, we can effectively reduce the statistical uncertainty. The study also shows that the higher the current applied, the higher fluxes will be achieved. For the present operation at 250 kA and future setup at 320 kA horn configurations, the signal neutrino fluxes increase about 13-14 times and 14-15 times at neutrino peak energy (about 1GeV at INGRID location) compared to without horn current applied, respectively. Our investigation shows that when the horn current is increased from 250 kA to 320 kA, the fluxes at neutrino peak energy are increased by 10% for both neutrino mode and anti-neutrino mode (see Fig. 2.6 and 2.7). Fig. 2.8 shows the fluxes at 2.5^o off-axis from the neutrino beam center which is in direction of ND280 and Super-K detectors.

2.2 Event rate measurement

2.2.1 Simulation of neutrino interactions with NEUT

In accelerator-based long baseline neutrino oscillation experiments, precise measurements of oscillation parameters require a precise understanding of neutrino interaction with the target at the detectors. Oscillation parameters are extracted from oscillation probabilities between flavors by analyzing the event rates at near detector and far detector. The oscillation probabilities , says $P(\nu_\mu \to \nu_\mu), P(\nu_\mu \to \nu_e), P(\bar{\nu}_\mu \to \bar{\nu}_\mu)$ and $P(\bar{\nu}_\mu \to \bar{\nu}_e)$ at T2K for example are functions of baseline and neutrino energy. Unfortunately, we don't know much about the neutrino energy in accelerator-based experiments like T2K since neutrinos are produced from the decay of products of the
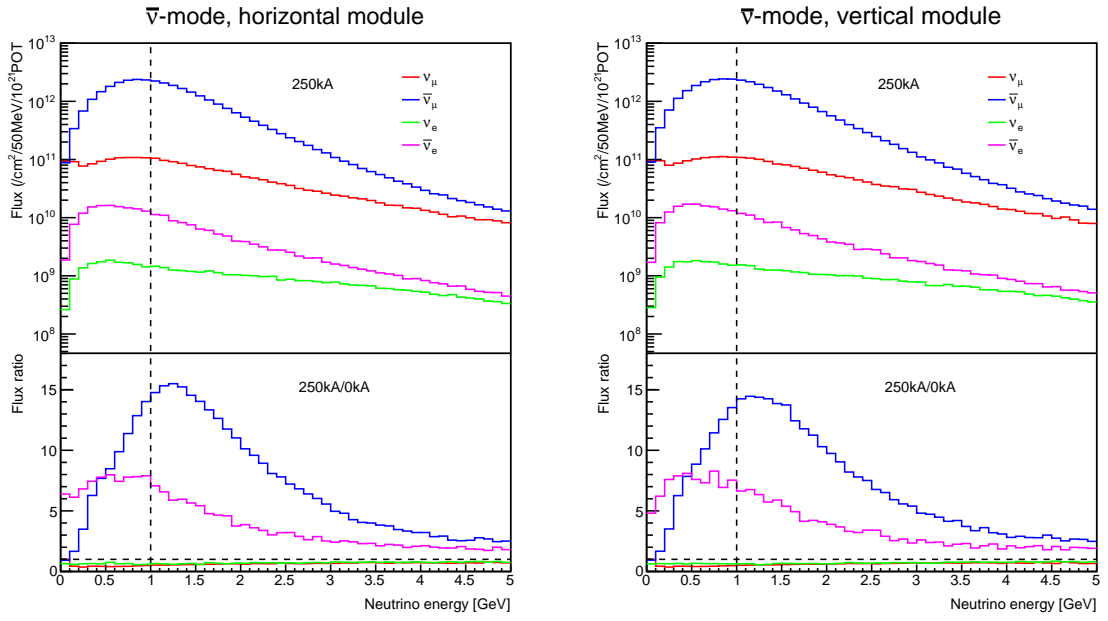
Figure 2.4: Neutrino fluxes at INGRID with -250 kA horn current applied.
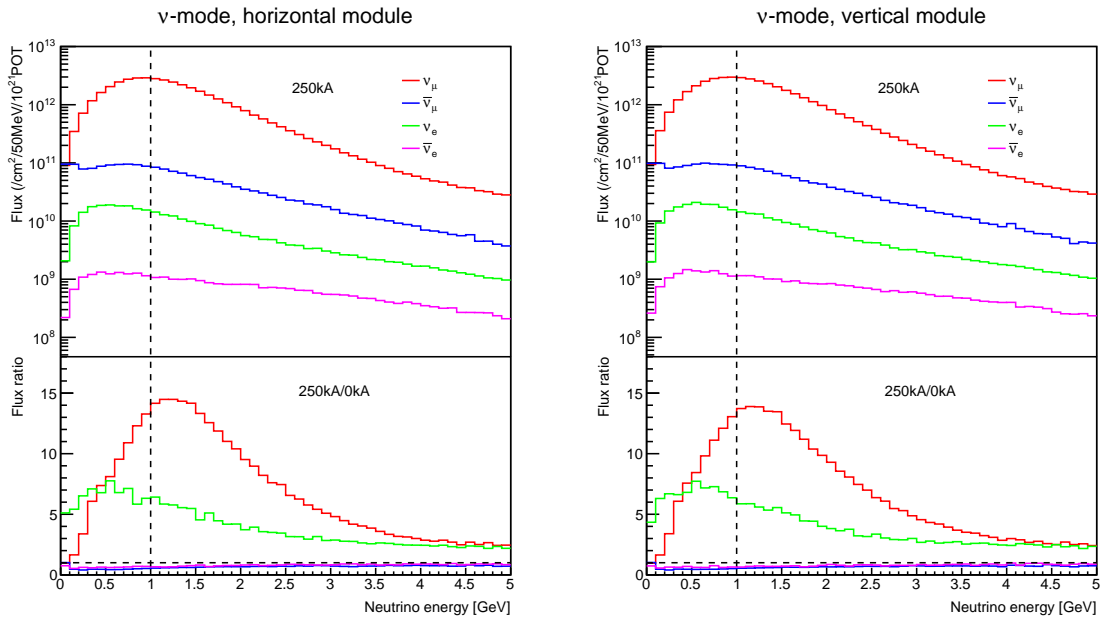
Figure 2.5: Neutrino fluxes at INGRID with +250 kA horn current applied.
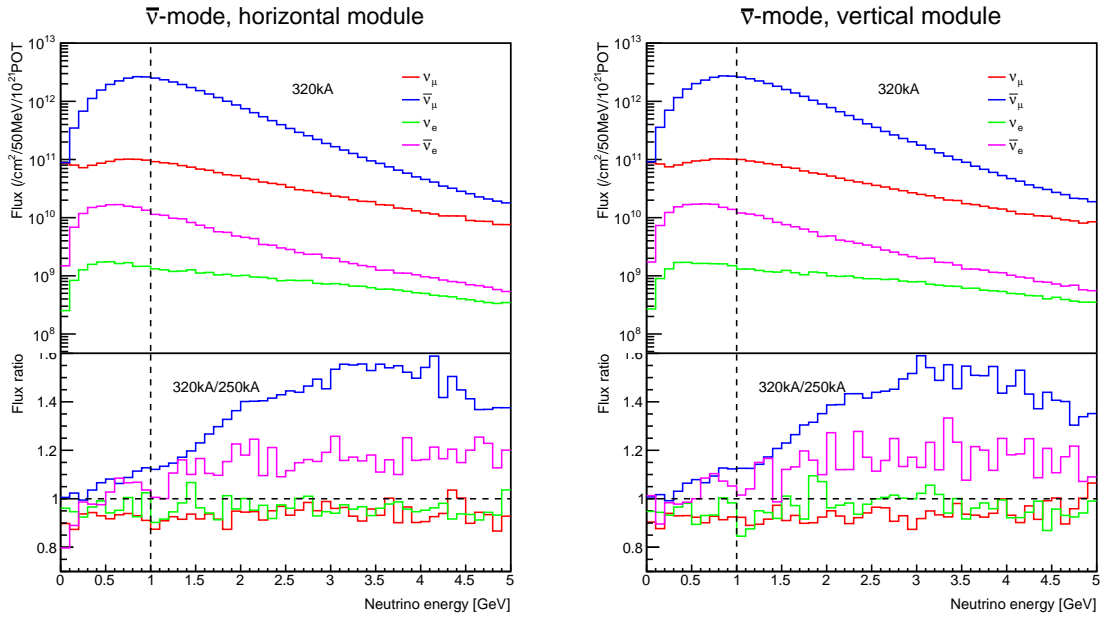
Figure 2.6: Neutrino fluxes at INGRID with -320 kA horn current applied.
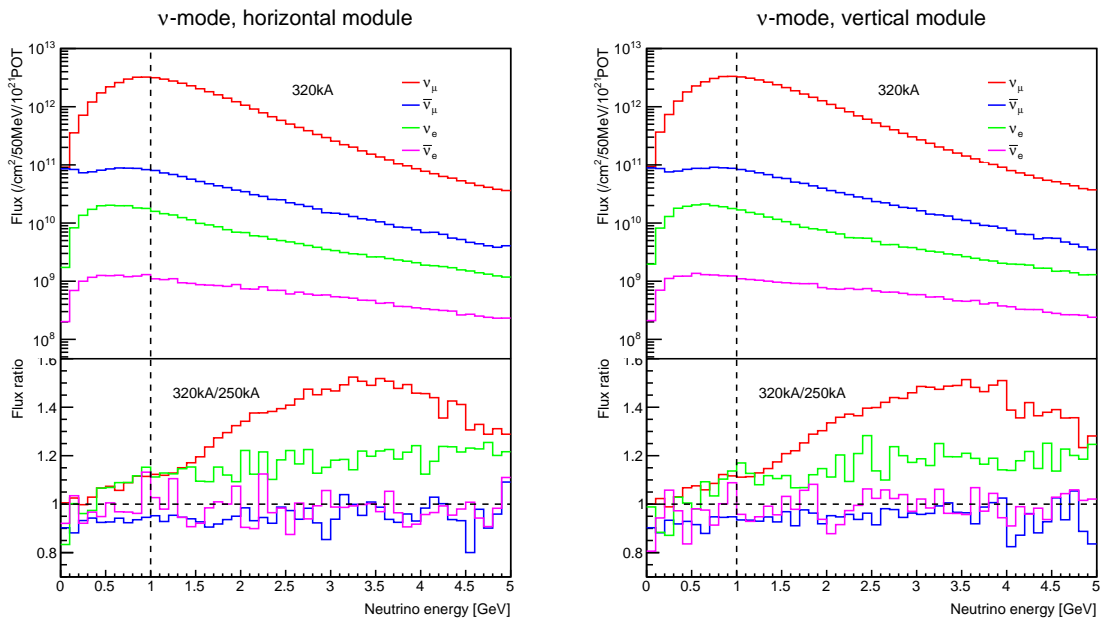
Figure 2.7: Neutrino fluxes at INGRID with +320 kA horn current applied.
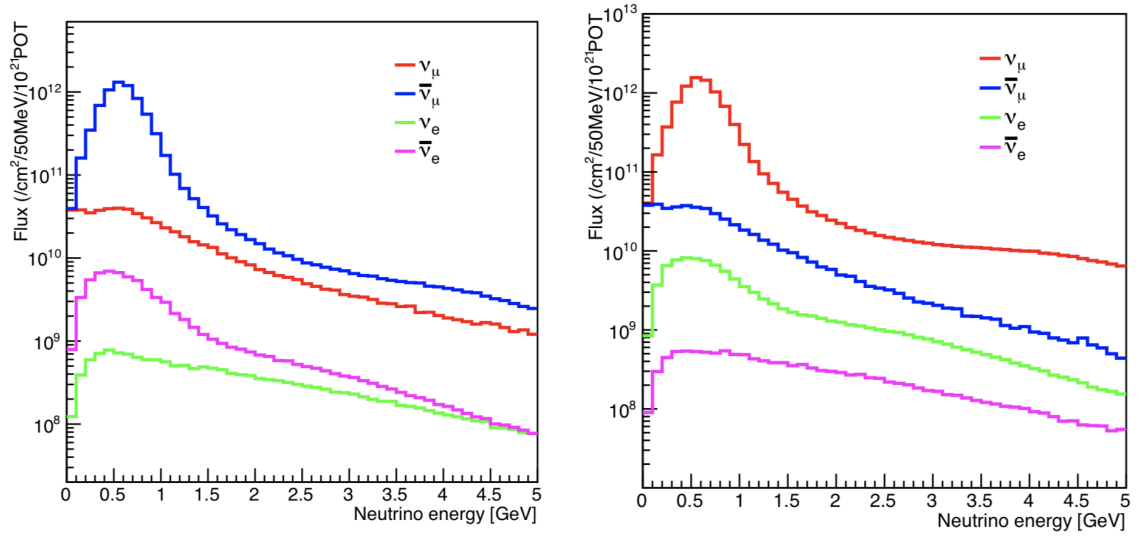
Figure 2.8: -320 kA (left) and +320 kA (right) fluxes at 2.5^o off-axis.
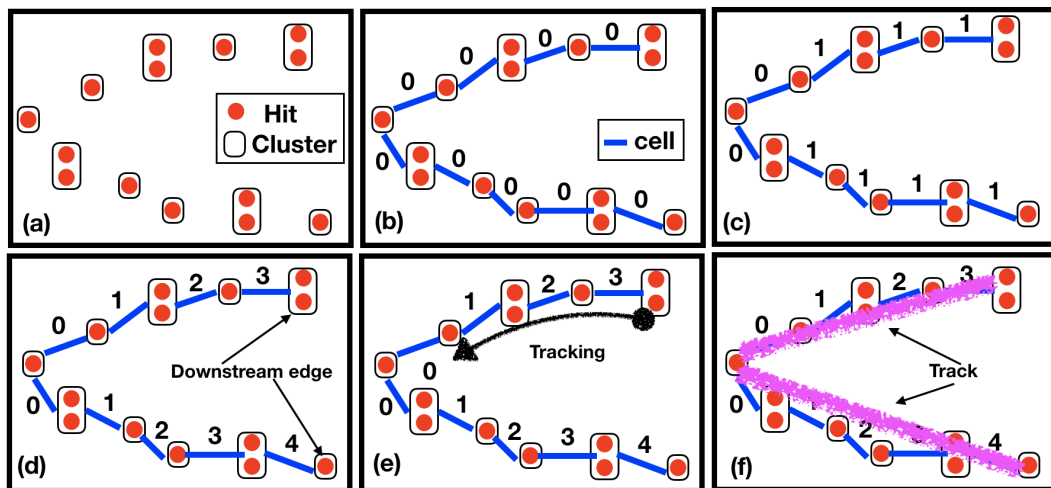
Figure 2.9: Cellular automaton algorithm.

proton-target collision. We therefore need to better understand neutrino-nucleus interactions at the detectors by which the neutrino energy can be reconstructed. There are some simulation packages called *event generator* allow us to study this procedure, such as NEUT, NUANCE, NEUGEN, GENIE, etc. T2K uses NEUT as its standard event generator, among others.

NEUT is a Monte Carlo simulation package studying interaction of neutrino with nucleus and nucleon from tens of MeV to hundreds of TeV energy range [57–59]. At the beginning, NEUT was developed to simulate the interaction of atmospheric neutrinos with hydrogen and oxygen nuclei in the water Cherenkov detector at the Kamikokande experiment. The program has been continuously updated to include more nuclear targets such as scintillators and iron in T2K near detectors. In NEUT, the simulation is not only for the primary interaction between neutrinos and nucleus but also for final state interaction (FSI) which describes the interaction between produced particles inside the nucleus. To run the program, we need to provide initial information, including neutrino source, target material, neutrino interaction models, and some other parameters. After running, the event generator will give kinematic information about target nucleons, outgoing leptons, all hadrons, and gamma rays.

2.2.2   Event selection

We follow the event selection procedure for INGRID data described in Ref. [67] for neutrino mode and Ref. [68] for anti-neutrino mode. The selection follows eight steps including:

1. Time clustering.
2. Number of continuous active planes selection.
3. Two-dimensional track reconstruction.
4. Three-dimensional track reconstruction.
5. Vertexing.
6. Beam timing cut.
7. Upstream VETO cut.
8. Fiducial volume cut.

Light produced by neutrino-nucleus interaction is collected by scintillators, then transmitted by wavelength shifting fiber before being detected by MPPCs (Multi-Pixel Photon Counters). The output charge of the signal is called ADC (Analog-to-Digital Converter), which is proportional to the number of detected photons or the number of PE (PhotoElectron). In our analysis, channels with ADC signals larger than 2.5PE are defined as *hit*.

At first, hits are classified into a cluster if there are more than five hits within 100 ns in an INGRID module. This step is to reduce the random MPPC noise hit.

Next, the so-called "continuous active planes selection" is applied to reduce accidental noise events. "Continuous active planes" are the neighborhood layers that

have at least one coincident hit in both x and y layers. The events which have more than two continuous active planes are selected.

In the third step, an algorithm called "cellular automaton" is used to reconstruct two-dimensional tracks (in x-z and y-z planes). The algorithm is a discrete model consisting of a regular grid of *cells*. Each cell has a finite number of states. First, a cluster is defined as adjacent hits in a layer (Fig. 2.9 (a)). Then two adjacent clusters are connected with a line segment which is *cell* of the cellular automaton (Fig. 2.9 (b)). The initial state value of cells is set to be zero (Fig. 2.9 (b)). Two cells are defined as neighbors if they share a common cluster which χ^2 is less than 1.5. If the upstream cell has the same state value as the current one, the state value increases by one unit (Fig. 2.9 (c and d)). The evolution is stopped if there are no more neighboring cells with the same state value. The downstream cluster of the last cell which has the largest state value is called *starting point* of the track reconstruction procedure (Fig. 2.9 (d)). From the starting point, the track is back upstream neighbor cells layer by layer until the state value of one upstream cell is zero or χ^2 is larger than two (Fig. 2.9 (e)). The algorithm reconstructs tracks from clusters belonging to the tracked cells (Fig. 2.9 (f)).

After two-dimensional track reconstruction is done, the work continues with three-dimensional ones. In this step, pairs of two-dimensional tracks in x track (x-z plane) and y track (y-z plane) are selected to combine three-dimensional tracks (i) if the difference between upstream point z of x track and y track is smaller than three layers; (ii) if there is more than one track satisfying the above condition with another one, the smallest difference is chosen; (iii) if there is more than one pair of tracks having the same difference from upstream point z, the pair with the smallest different downstream point z is selected. If they are still equal, the pair which has closest total PE per track length is selected.

The sixth step will search for vertexes of the tracks from three-dimensional tracks. The vertex is commonly identified as the upstream edge of each three-dimensional track. Two three-dimensional tracks are defined as from a common vertex if they satisfy both conditions:

(i) The sum of the z position distance between the upstream edges of the two tracks in x view and y view is less than one

$$|\Delta z_x| + |\Delta z_y| \leq 1 \text{ (plane)}, \tag{2.1}$$

where $|\Delta z_x|$ and $|\Delta z_y|$ are z position distance between the upstream edges of the two track in x view and y view.

(ii) Distance between upstream edges of the two track in xy-plane is less than 150mm

$$\sqrt{\Delta x^2 + \Delta y^2} < 150 (mm), \tag{2.2}$$

where Δx and Δy are x and y position distance between the upstream of the two tracks.

Item	FHC mode (%)	RHC mode (%)
Iron mass	0.13	0.13
Accidental PMMC noise	0.27	0.1
Hit efficiency	0.39	0.43
Event pileup	0.14	0.19
Beam related backgrounds	0.27	0.60
Not beam related background	0.01	0.01
Track reconstruction	0.49	1.21
Track matching	0.19	0.55
Vertexing	0.43	0.25
Beam timing selection	0.01	0.01
Upstream VETO cut	0.13	0.54
Fiducial volume cut	0.09	0.26
Total	0.91	1.67

Table 2.1: Systematic errors for total number of events in all modules for neutrino mode and anti-neutrino mode.

The beam timing cut is applied for events outside of expected on-timing interval [-100ns, +100ns] to reduce off-timing backgrounds such as cosmic rays.

The last two steps VETO cut and fiducial volume cut are applied to exclude events coming from outside the modules.

2.2.3 Systematic uncertainties

The systematic error of Data/MC is the INGRID detector systematic error of the total number of events selected in all modules, not including uncertainties of flux and neutrino interaction. The total systematic error is estimated to be 0.91% for the neutrino mode [67] and 1.67% for the anti-neutrino mode [68]. The sources of uncertainty are summarized in Table 2.1.

2.2.4 The event rate at INGRID

Fig. 2.10 shows daily event rate at INGRID detector in T2K run 10 taking data from 7/11 - 19/12/2019 and 13/01 - 12/02/2020. These data sets are for neutrino mode (FHC) at 250 kA horn operation. The data processing efficiencies are 99.91% with a total of 4.7656×10^{20} POT (protons-on-target). The neutrino event rate during the whole run is stable, and the average value is measured to be 1.694 [/10^{14} POT] $\pm$ 0.001(stat.) $\pm$ 0.015(sys.) with hps (horn power supply current) correction. The data to MC ratio for run 10 is 0.969 $\pm$ 0.001(stat.) $\pm$ 0.009(sys.). Tables 2.2 and 2.3 summarize the comparison between our MC simulation and data at INGRID.

Our MC study shows that when the horn current is increased from 250 kA to 320 kA, the neutrino event rates at INGRID are increased by 26% and 18% to be

| | Data | MC | Data/MC |
	[/10^{14} POT]	[/10^{14} POT]	[/10^{14} POT]
run1	1.710 ± 0.002(stat.) ± 0.015(sys.)	1.748	0.978 ± 0.001(stat.) ± 0.009(sys.)
run2	1.746 ± 0.001(stat.) ± 0.016(sys.)	1.748	0.999 ± 0.001(stat.) ± 0.009(sys.)
run3c	1.739 ± 0.001(stat.) ± 0.016(sys.)	1.748	0.995 ± 0.001(stat.) ± 0.009(sys.)
run8a	1.700 ± 0.001(stat.) ± 0.015(sys.)	1.748	0.973 ± 0.001(stat.) ± 0.009(sys.)
run8b	1.702 ± 0.001(stat.) ± 0.015(sys.)	1.748	0.974 ± 0.001(stat.) ± 0.009(sys.)
run8c	1.699 ± 0.001(stat.) ± 0.015(sys.)	1.748	0.972 ± 0.001(stat.) ± 0.009(sys.)
run9	1.697 ± 0.001(stat.) ± 0.015(sys.)	1.748	0.971 ± 0.001(stat.) ± 0.009(sys.)
run10	1.694 ± 0.001(stat.) ± 0.015(sys.)	1.748	0.969 ± 0.001(stat.) ± 0.009(sys.)

Table 2.2: Event rate comparison between FHC runs and MC with +250kA horn operation.

| | Data | MC | Data/MC |
	[/10^{14} POT]	[/10^{14} POT]	[/10^{14} POT]
run5	0.560 ± 0.0010(stat.) ± 0.0094(sys.)	0.565	0.991 ± 0.001(stat.) ± 0.017(sys.)
run6	0.554 ± 0.0004(stat.) ± 0.0093(sys.)	0.565	0.981 ± 0.001(stat.) ± 0.017(sys.)
run7	0.555 ± 0.0004(stat.) ± 0.0093(sys.)	0.565	0.982 ± 0.001(stat.) ± 0.017(sys.)

Table 2.3: Event rate comparison between RHC runs and MC with -250kA horn operation.

2.209 [/10^{14} POT] and 0.664 [/10^{14} POT] for neutrino mode and anti-neutrino mode, respectively.

Fig. 2.11 illustrates some basic MC distributions of number of events in both neutrino mode (FHC) and anti-neutrino mode (RHC) for 320 kA horn running.

2.3 Beam profile measurement

The physics of beam profile measurement at INGRID is as follows. The beam profiles for horizontal and vertical modules are reconstructed separately based on the neutrino event numbers of every single module (seven in the horizontal direction and seven in the vertical direction). Then the fitted Gaussian functions are used to specify peak position and standard deviation, which respectively correspond to the beam center and beam width.

For T2K run 10, the measurements of neutrino beam direction are stable with a requirement within 1 mrad (see Fig. 2.12):

$$\bar{\theta}_H = \ -0.055 \pm 0.013\text{(stat.)} \pm 0.096\text{(sys.) mrad,} \tag{2.3}$$

$$\bar{\theta}_V = \ \ \ 0.085 \pm 0.014\text{(stat.)} \pm 0.106\text{(sys.) mrad.} \tag{2.4}$$

Fig. 2.13 and 2.14 show that the beam center and beam width are stable and within allowed variation range. The data to MC ratio of beam width is calculated for
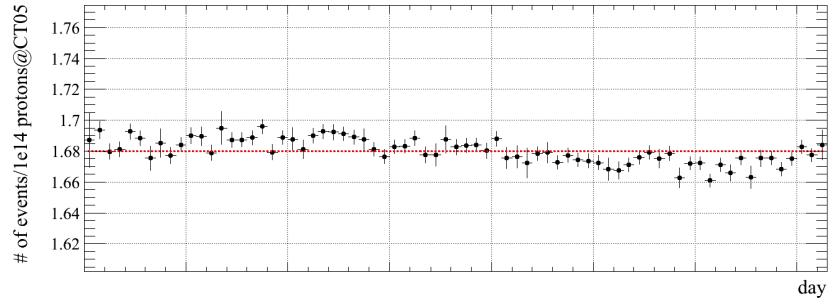
Figure 2.10: The daily event rate at INGRID in T2K run 10 without correction.
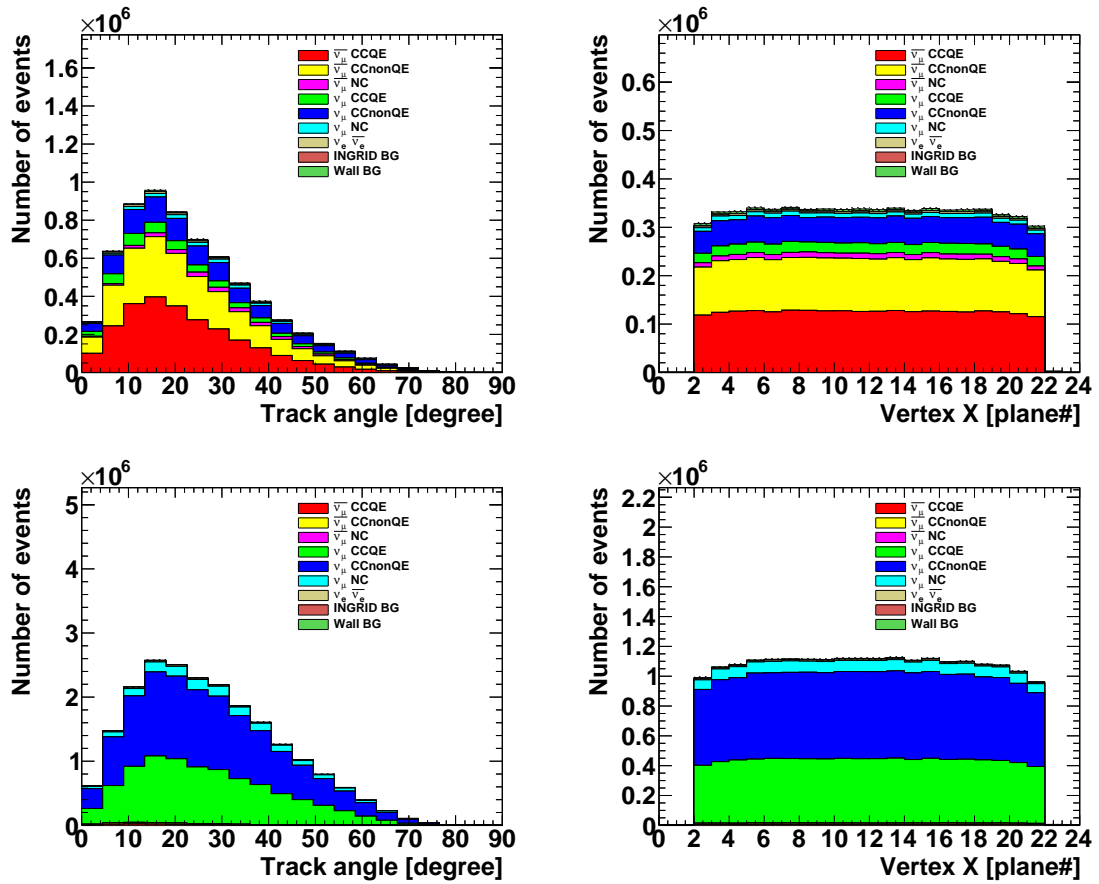
Figure 2.11: MC event distributions vs angle (left) and vertex x (right) of RHC mode (top) and FHC mode (bottom) for 320 kA horn operation.

	Horizontal center [cm]	Vertical center [cm]
FHC 250kA	2.33 ± 0.89	-0.24 ± 0.99
FHC 320kA	2.53 ± 0.67	-1.27 ± 0.72
RHC 250kA	2.93 ± 0.96	-0.56 ± 1.65
RHC 320kA	1.94 ± 1.11	-0.49 ± 1.19

Table 2.4:   Summary of INGRID MC beam center with 250 kA and 320 kA horn operations.

	Horizontal width [cm]	Vertical width [cm]
FHC 250kA	430.162 ± 1.429	454.508 ± 1.682
FHC 320kA	388.378 ± 0.962	399.982 ± 1.088
RHC 250kA	451.607 ± 2.444	483.255 ± 3.033
RHC 320kA	408.151 ± 1.680	423.141 ± 1.906

Table 2.5:   Summary of INGRID MC beam width with 250 kA and 320 kA horn operations.

250 kA horn operation as follow:

$$W(\text{Data/MC})_H = \quad 1.016 \pm 0.004(\text{stat.}), \tag{2.5}$$

$$W(\text{Data/MC})_V = \quad 1.009 \pm 0.004(\text{stat.}). \tag{2.6}$$

The results of the MC study on beam profile are presented. The particular values of the beam center and beam width of the horizontal module and vertical module for both FHC mode and RHC mode are summarized in Table 2.4 and Table 2.5 for 250 kA and 320 kA horn operations.

2.4   Conclusion

In the section, we have presented the MC study and the measurements at the INGRID detector for different horn configurations. The comparison shows good agreement between the MC results and the T2K data up to run 10 for 250 kA horn operation.

We also showed the MC study at INGRID with a 320 kA horn configuration, which can be tested with future data of T2K. At 320 kA operation, the expected event rates are 2.209 [/10^{14} POT] and 0.664 [/10^{14} POT] for neutrino mode and anti-neutrino mode, respectively. The expected beam directions with respect to the centers of the neutrino mode are 0.091 ± 0.024 mrad for horizontal and -0.046 ± 0.026 mrad for vertical. For anti-neutrino mode, the corresponding values are 0.070 ± 0.040 mrad and -0.018 ± 0.044 mrad.
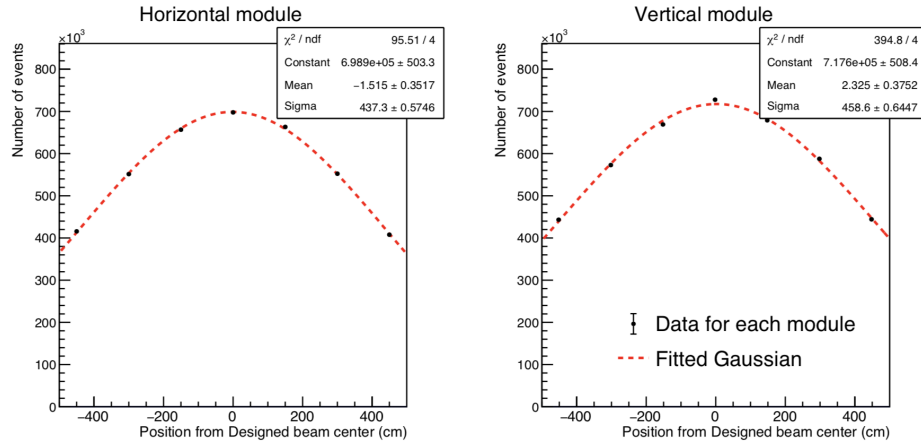
Figure 2.12: Reconstructed neutrino beam profiles for horizontal (left) and vertical (right) modules for T2K run 10. Each point represents the number of selected events in each module.
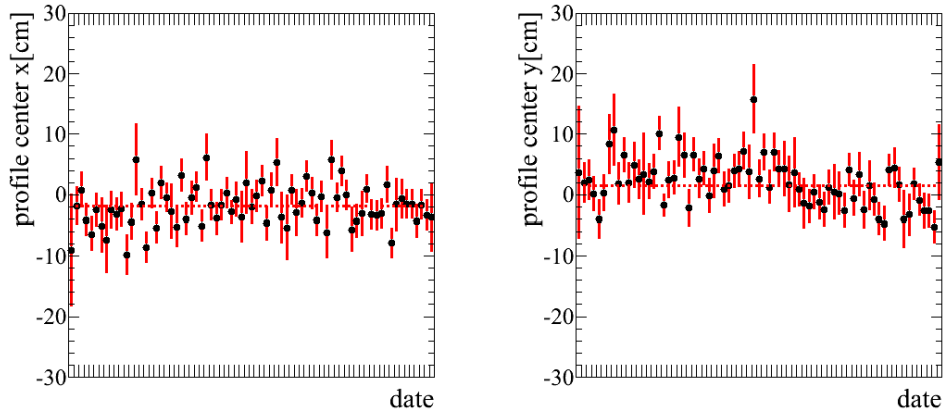
Figure 2.13: The stability of neutrino beam profiles of INGRID horizontal (left) and vertical (right) modules for T2K run 10.
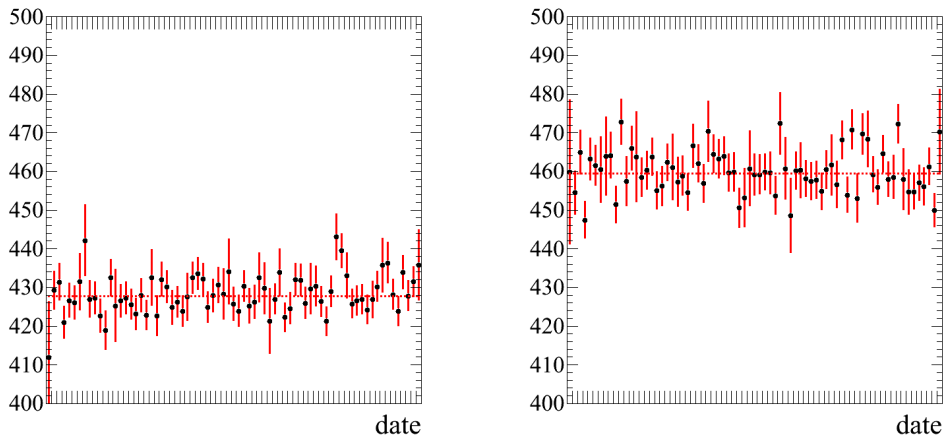
Figure 2.14: The history of neutrino beam width for INGRID horizontal (left) and vertical (right) modules for T2K run 10.

Chapter 3. Testing CP and CPT invariances with neutrino oscillation measurements in T2K experiment

3.1 C, P, and T symmetries

3.1.1 Charge conjugation C

Charge conjugation is an important discrete symmetry that transforms a particle into its antiparticle and vice versa. In particular, it converts not only the sign of electric charge but also other quantum charges such as baryon number, lepton number, strangeness, charm, beauty, truth, ... while leaving mass, energy, momentum, and spin unchanged [69]. The charge conjugation operator is denoted by the letter C and defined as follows

$$C|p\rangle = |\overline{p}\rangle, \tag{3.1}$$

where $|p\rangle$ and $|\overline{p}\rangle$ represent particle and antiparticle states, respectively. It is obvious that if we apply the charge conjugation twice, we get back to the initial state. That is, $C^2 = I$, or eigenvalues of the operator C are ± 1.

$$C|p\rangle = \pm|p\rangle = |\overline{p}\rangle. \tag{3.2}$$

Because they differ only by a sign, equation (3.2) shows that $|p\rangle$ and $|\overline{p}\rangle$ represent the same physical state. This means that only particles that are their own antiparticles can be eigenstates of C. They are called Majorana particles. Charge conjugation symmetry is conserved in strong and electromagnetic interactions but not in weak interaction. When we apply C to left-handed neutrino, it will give the left-handed antineutrino, which doesn't exist in the SM.

$$C|\nu_L\rangle = |\overline{\nu}_L\rangle. \tag{3.3}$$

C is an hermitian unitary operator $C = C^{-1} = C^\dagger$ which has explicit form in Dirac representation

$$C = i\gamma^0\gamma^2 = \begin{pmatrix} 0 & i\sigma_2 \\ i\sigma_2 & 0 \end{pmatrix}. \tag{3.4}$$

The Dirac γ matrices satisfy

$$C(\gamma^\mu)^T C^{-1} = -\gamma^\mu, \tag{3.5}$$

$$C(\gamma^5)^T C^{-1} = \gamma^5, \tag{3.6}$$

$$C(\gamma^\mu\gamma^5)^T C^{-1} = -\gamma^\mu\gamma^5. \tag{3.7}$$

The operation of C on scalar field $\phi(x)$, vector field $A(x)$, and Dirac spinor field $\psi(x)$ operators are

$$C\phi(x)C^{-1} = \phi(x)^\dagger, \tag{3.8}$$

$$CA_\mu(x)C^{-1} = -A_\mu^\dagger(x), \tag{3.9}$$

$$C\psi(x)C^{-1} = i\gamma^0\gamma^2\overline{\psi}(x)^T = C\overline{\psi}(x)^T = -i\gamma^2\psi(x)^*, \tag{3.10}$$

$$C\overline{\psi}(x)C^{-1} = i\psi(x)^T\gamma^2\gamma^0 = -\psi(x)^T(i\gamma^0\gamma^2) = -\psi(x)^T C^{-1}. \tag{3.11}$$

We can take an example to see how it works for the Dirac spinor field. Consider the Dirac equation of a particle with charge q and mass m coupled to an external electromagnetic field A_μ [38].

$$i\gamma^\mu(\partial_\mu + iqA_\mu)\psi - m\psi = 0. \tag{3.12}$$

By taking complex conjugate of equation (3.12) and multiplying left-handed with $-i\gamma^2$ gives (note that for γ matrices, $(\gamma^0)^* = \gamma^0$, $(\gamma^1)^* = \gamma^1$, $(\gamma^2)^* = -\gamma^2$, $(\gamma^3)^* = \gamma^3$, and $\gamma^2\gamma^\mu = -\gamma^\mu\gamma^2$ for $\mu \neq 2$)

$$(-i\gamma^2)(-i\gamma^{\mu*})(\partial_\mu - iqA_\mu^*)\psi^* - m(-i\gamma^2)\psi^* = 0$$
$$\Leftrightarrow -i\gamma^\mu(\partial_\mu - iqA_\mu^*)(i\gamma^2\psi^*) + m(i\gamma^2\psi^*) = 0 \tag{3.13}$$
$$\Leftrightarrow i\gamma^\mu(\partial_\mu - iqA_\mu^*)(i\gamma^2\psi^*) - m(i\gamma^2\psi^*) = 0.$$

This is the Dirac equation of a particle with the same mass as the original particle but with opposite charge $-q$ which is coupled to an external electromagnetic field A_μ^*. We refer to it as an antiparticle of the original one and its wave function is defined as $\psi^C = i\gamma^2\psi^*$.

We now can check for each Lorentz invariant terms in the free Dirac Lagrangian

$$\mathcal{L} = \overline{\psi}\gamma^\mu\partial_\mu\psi - m\overline{\psi}\psi \tag{3.14}$$

under C transformation with the help of equations (3.10) and (3.11) (note fermion fields are anticommutative $\overline{\psi}\psi = -\psi\overline{\psi}$, and $\overline{\psi}\partial_\mu\psi = -\psi\partial_\mu\overline{\psi}$). For the mass term

$$\overline{\psi}\psi \to C\overline{\psi}\psi C^{-1} = C\overline{\psi}C^{-1}C\psi C^{-1} = -\psi^T C^{-1}C\overline{\psi}^T = -\psi^T\overline{\psi}^T = -\psi\overline{\psi} = \overline{\psi}\psi. \tag{3.15}$$

For kinematic term

$$\begin{aligned}
\overline{\psi}\gamma^\mu\partial_\mu\psi \to C\overline{\psi}\gamma^\mu\partial_\mu\psi C^{-1} &= C\overline{\psi}C^{-1}C\gamma^\mu C^{-1}C\partial_\mu C^{-1}C\psi C^{-1} \\
&= (-\psi^T C^{-1})(-\gamma^{\mu T})C\partial_\mu C^{-1}(C\overline{\psi}^T) \\
&= (\psi^T C^{-1})_\alpha(\gamma^{\mu T})_{\alpha\beta}(C\partial_\mu\overline{\psi}^T)_\beta \\
&= \psi_{\alpha'}(C^{-1}\gamma^\mu C)_{\alpha'\beta'}(\partial_\mu\overline{\psi})_{\beta'} \\
&= \psi_{\alpha'}(-\gamma^\mu)_{\beta'\alpha'}(\partial_\mu\overline{\psi})_{\beta'} \\
&= \overline{\psi}_{\beta'}(\gamma^\mu)_{\beta'\alpha'}(\partial_\mu\psi)_{\alpha'} \\
&= \overline{\psi}\gamma^\mu\partial_\mu\psi. \tag{3.16}
\end{aligned}$$

Therefore, the free Dirac Lagrangian is invariant under the charge conjugation transformation

$$\mathcal{L} \to C\mathcal{L}C^{-1} = iC\overline{\psi}\gamma^\mu\partial_\mu\psi C^{-1} - mC\overline{\psi}\psi C^{-1}$$
$$= i\overline{\psi}\gamma^\mu\partial_\mu\psi - m\overline{\psi}\psi = \mathcal{L}. \tag{3.17}$$

Similarly, we can derive the transformation of vector current $j_V^\mu = \overline{\psi}\gamma^\mu\psi$ and axial-vector current $j_A^\mu = \overline{\psi}\gamma^\mu\gamma^5\psi$ as follows

$$j_V^\mu \to C\overline{\psi}\gamma^\mu\psi C^{-1} = -\overline{\psi}\gamma^\mu\psi = -j_V^\mu, \tag{3.18}$$

$$j_A^\mu \to C\overline{\psi}\gamma^\mu\gamma^5\psi C^{-1} = \overline{\psi}\gamma^\mu\gamma^5\psi = j_A^\mu. \tag{3.19}$$

3.1.2 Parity inversion P

The second discrete symmetry we now discuss is parity transformation, which is associated to spatial inversion through the origin

$$x^\mu = (t, x, y, z) \to x_\mu = (t, -x, -y, -z). \tag{3.20}$$

It is well known that parity is conserved in QED and QCD, but not in weak interaction. The parity operator is denoted as P such that

$$P|\psi(t, x)\rangle = |\psi(t, -x)\rangle. \tag{3.21}$$

Apparently, if P is applied twice, the original state is recovered

$$P^2|\psi(t, x)\rangle = P|\psi(t, -x)\rangle = |\psi(t, x)\rangle. \tag{3.22}$$

Therefore, parity is a hermitian and unitary operator with eigenvalues ± 1. The parity transformation applied for scalar field $\phi(x)$, vector field $A_\mu(x)$ and Dirac field $\psi(x)$ are as follows

$$P\phi(x)P^{-1} = \phi(-x), \tag{3.23}$$

$$PA^\mu(x)P^{-1} = A_\mu(-x), \tag{3.24}$$

$$P\psi(x)P^{-1} = \gamma^0\psi(-x), \tag{3.25}$$

$$P\overline{\psi}(x)P^{-1} = \overline{\psi}(-x)\gamma^0. \tag{3.26}$$

The matrix γ^0 is called intrinsic parity of the Dirac field. The transformation of a vector and an axial vector currents under parity are

$$j_V^\mu \to P\overline{\psi}\gamma^\mu\psi P^{-1} = P\overline{\psi}P^{-1}P\gamma^\mu P^{-1}P\psi P^{-1} = \overline{\psi}\gamma^0\gamma^\mu\gamma^0\psi$$
$$= (\overline{\psi}\gamma^0\psi, -\overline{\psi}\gamma^i\psi) = (j_V^0, -j_V^i) = (j_V)_\mu, \tag{3.27}$$

$$j_A^\mu \to P\overline{\psi}\gamma^\mu\gamma^5\psi P^{-1} = P\overline{\psi}P^{-1}P\gamma^\mu P^{-1}P\gamma^5 P^{-1}P\psi P^{-1} = \overline{\psi}\gamma^0\gamma^\mu\gamma^5\gamma^0\psi$$
$$= (-\overline{\psi}\gamma^0\gamma^5\psi, +\overline{\psi}\gamma^i\psi) = (-j_A^0, +j_A^i) = -(j_A)_\mu. \tag{3.28}$$

We then can easily check that

$$j_V^\mu \cdot j_{V\mu} \to j_V^\mu \cdot j_{V\mu}, \tag{3.29}$$

$$j_A^\mu \cdot j_{A\mu} \to j_A^\mu \cdot j_{A\mu}, \tag{3.30}$$

$$j_A^\mu \cdot j_{V\mu} \to -j_A^\mu \cdot j_{V\mu}. \tag{3.31}$$

The result of equation (3.31) provides a mechanism to explain violation of parity in the weak interaction. In particular, the weak interaction current should be a combination of vector and axial vector of the form V - A.

3.1.3 Time reversal T

Time reversal is a transformation that takes the sign of time to be opposite

$$(t, x, y, z) \rightarrow (-t, x, y, z). \tag{3.32}$$

Time reversal operator is denoted by the letter T. It is hermitian and unitary: $T = T^{-1} = T^{\dagger}$. For a field $\psi(t, x)$, we have

$$T|\psi(t, x)\rangle = |\psi(-t, x)\rangle. \tag{3.33}$$

T is called anti-linear operator since it converts imaginary number i to $-i$. Time reversal transformation for scalar field $\phi(t, x)$, vector field $A_\mu(t, x)$, and Dirac field $\psi(t, x)$ are

$$T\phi(t, x)T^{-1} = \phi(-t, x), \tag{3.34}$$
$$TA_\mu(t, x)T^{-1} = A^\mu(-t, x), \tag{3.35}$$
$$T\psi(t, x)T^{-1} = \gamma^1\gamma^3\psi(-t, x), \tag{3.36}$$
$$T\overline{\psi}(t, x)T^{-1} = \overline{\psi}(-t, x)\gamma^3\gamma^1. \tag{3.37}$$

The transformation of a vector and an axial vector currents under time reversal are

$$
\begin{aligned}
j_V^\mu \rightarrow T\overline{\psi}\gamma^\mu\psi T^{-1} &= T\overline{\psi}T^{-1}T\gamma^\mu T^{-1}T\psi T^{-1} = \overline{\psi}\gamma^3\gamma^1\gamma^{\mu*}\gamma^1\gamma^3\psi \\
&= (\overline{\psi}\gamma^0\psi, -\overline{\psi}\gamma^i\psi) = (j_V^0, -j_V^i) = (j_V)_\mu, \tag{3.38}
\end{aligned}
$$

$$
\begin{aligned}
j_A^\mu \rightarrow T\overline{\psi}\gamma^\mu\gamma^5\psi T^{-1} &= T\overline{\psi}T^{-1}T\gamma^\mu T^{-1}T\gamma^5 T^{-1}T\psi T^{-1} = \overline{\psi}\gamma^3\gamma^1\gamma^\mu\gamma^5\gamma^1\gamma^3\psi \\
&= (\overline{\psi}\gamma^0\gamma^5\psi, -\overline{\psi}\gamma^i\gamma^5\psi) = (j_A^0, -j_A^i) = (j_A)_\mu. \tag{3.39}
\end{aligned}
$$

3.2 The CPT theorem

CPT symmetry is a fundamental symmetry of Nature which simultaneously transforms the charge conjugation C, parity inversion P, and time reversal T. The CPT theorem states that *all interactions described by an unitary, local, Lorentz-invariant quantum field theory in a flat Minkowski space must be invariant under the combined CPT transformation.* Here we denote the combined CPT transformation as an antiunitary operator

$$\Theta = CPT, \quad \Theta^{-1} = \Theta^{\dagger}. \tag{3.40}$$

By applying the CPT operator Θ, a particle state transforms into an anti-particle state as follows

$$\Theta|p\rangle = |\overline{p}\rangle. \tag{3.41}$$

We present here the proofs of the CPT theorem based on Lagrangian and axiomatic quantum field theories. The work is comprehensibly summarized by Ralf Lehnert in Ref. [70]. A physical state in the Hilbert space and a quantum operator transform under CPT conjugation as follow:

$$|\psi\rangle \quad \rightarrow \quad |\Theta\psi\rangle = \Theta|\psi\rangle \equiv |\overline{\psi}\rangle, \tag{3.42}$$

$$\mathcal{A} \quad \rightarrow \quad \mathcal{A}_{CPT} = \Theta\mathcal{A}\Theta^\dagger. \tag{3.43}$$

3.2.1 Proof of CPT theorem based on Lagrangian quantum field theory

The CPT theorem was studied for the first time and formulated in the context of Lagrangian quantum field theory by Schwinger [71] [72], Luders [73], Pauli [74], and Bell [75]. Therefore this theorem is also called *Lagrangian CPT theorem*. This formalism simply means all terms that appear in Lagrangian must be CPT invariant. The CPT transformation of field operators, ordinary derivative and tensor are as follows:

$$\phi(x) \quad \rightarrow \quad \Theta\phi(x)\Theta^\dagger = \phi^\dagger(-x), \tag{3.44}$$

$$\psi(x) \quad \rightarrow \quad \Theta\psi(x)\Theta^\dagger = -\gamma^5\psi^*(-x), \tag{3.45}$$

$$\overline{\psi}(x) \quad \rightarrow \quad \Theta\overline{\psi}(x)\Theta^\dagger = -\psi^T(-x)\gamma^5\gamma^0, \tag{3.46}$$

$$A_\mu(x) \quad \rightarrow \quad \Theta A_\mu(x)\Theta^\dagger = -A_\mu^\dagger(-x), \tag{3.47}$$

$$\partial_\mu \quad \rightarrow \quad \Theta\partial_\mu\Theta^\dagger = \partial_\mu, \tag{3.48}$$

$$\mathcal{T}_{\mu_1,\mu_2,...,\mu_n}(x) \quad \rightarrow \quad \Theta\mathcal{T}_{\mu_1,\mu_2,...,\mu_n}(x)\Theta^\dagger = (-1)^n\mathcal{T}_{\mu_1,\mu_2,...,\mu_n}^\dagger(-x). \tag{3.49}$$

Here we denote the general spacetime coordinates $x \equiv (t, x, y, z)$. It is straightforward to check that following terms in the Lagrangian are CPT invariant

$$\overline{\psi}\psi, \quad \overline{\psi}\gamma^\mu\partial_\mu\psi, \quad \overline{\psi}\gamma^\mu A_\mu\psi, \quad \overline{\psi}\gamma^\mu\gamma^5\psi W_\mu, \quad \overline{\psi}\sigma^{\mu\nu}\psi F_{\mu\nu}.$$

For example under single C, P and T transformation

$$\overline{\psi}\gamma^\mu\psi = j_V^\mu \xrightarrow{C} -j_V^\mu \xrightarrow{P} -(j_V)_\mu \xrightarrow{T} -j_V^\mu,$$

$$\overline{\psi}\gamma^\mu\gamma^5\psi = j_A^\mu \xrightarrow{C} j_A^\mu \xrightarrow{P} -(j_A)_\mu \xrightarrow{T} -j_A^\mu,$$

$$A_\mu \xrightarrow{C} -A_\mu \xrightarrow{P} -A^\mu \xrightarrow{T} -A_\mu.$$

Then

$$\overline{\psi}\gamma^\mu A_\mu\psi = j_V^\mu A_\mu \xrightarrow{C} j_V^\mu A_\mu \xrightarrow{P} (j_V)_\mu A^\mu \xrightarrow{T} j_V^\mu A_\mu, \tag{3.50}$$

$$\overline{\psi}\gamma^\mu\gamma^5\psi W_\mu = j_A^\mu W_\mu \xrightarrow{C} -j_A^\mu W_\mu \xrightarrow{C} (j_A)_\mu W^\mu \xrightarrow{T} j_A^\mu W_\mu. \tag{3.51}$$

We now proof the theorem through three steps as follows:

(1) Lorentz invariance: All possible terms in the Lagrangian must be Lorentz scalars. Therefore, Lorentz indices must come in pairs in such terms, or equivalently, the total number of Lorentz indices in such terms must be even. The Lagrangian then transforms under CPT as

$$\Theta\mathcal{L}(x)\Theta^{-1} = (-1)^{2k}\mathcal{L}^\dagger(-x) = \mathcal{L}^\dagger(-x). \tag{3.52}$$

(2) Unitarity: The Lagrangian must be hermitian in order to preserve probability conservation

$$\Theta \mathcal{L}(x) \Theta^{-1} = \mathcal{L}^\dagger(-x) = \mathcal{L}(-x). \tag{3.53}$$

(3) Locality: This requires quantum fields to interact locally or they must be point interactions. If the theory satisfies this property, then the action is invariant under CPT

$$\Theta S \Theta^{-1} = \int d^4x \mathcal{L}(-x) = \int d^4x \mathcal{L}(x) = S. \tag{3.54}$$

In the last step, we note that all terms in the Lagrangian are Lorentz invariant, so it is straightforward to change the integration variable and eliminate the minus sign. We have just shown that every quantum field theory that respects Lorentz symmetry, unitarity, and locality must be CPT invariant.

3.2.2 Proof of CPT theorem based on axiomatic quantum field theory

Later, R. Jost [76] (English version by Greenberg [77]) completed a general proof based on axiomatic quantum field theory, which is known as *axiomatic CPT theorem*. Jost's version is more abstract and mathematically rigorous because it can perform a CPT transformation of any relativistic field without using individual discrete transformations C, P, and T separately. Jost's approaching method is to admit necessary axioms as follows:

(1) Enlargement of Lorentz group:

In order to prove the CPT theorem, we need to enlarge *proper Lorentz group* to *complex Lorentz group*. We will now see why it should be so. We have already known that spacetime coordinates x^μ change sign under CPT operation

$$x^\mu \xrightarrow{CPT} -x^\mu.$$

This means that the CPT transformation can be interpreted by multiplying with $-I_{4\times 4}$ matrix. *Proper Lorentz group* $L_+^\uparrow$, however does not contain this entity. An extension from the proper Lorentz group to *complex Lorentz group*, luckily satisfies our requirement. For example, consider a complex Lorentz group Λ

$$\Lambda = \begin{pmatrix} \cos\phi & i\sin\phi & 0 & 0 \\ i\sin\phi & \cos\phi & 0 & 0 \\ 0 & 0 & \cos\phi & -\sin\phi \\ 0 & 0 & \sin\phi & \cos\phi \end{pmatrix}. \tag{3.55}$$

It can be obviously seen that $\Lambda = -I_{4\times 4}$ if we choose $\phi = \pi$. This requirement shows a closed relationship between the CPT transformation and the Lorentz transformation.

(2) Poincare invariance of vacuum state:

The vacuum state is assumed to be invariant under the Poincare transformation, which consists of complex Lorentz and translation transformations.

$$U(\Lambda, a)|0\rangle = |0\rangle$$

More clearly, the vacuum should have zero momentum and angular momentum.

(3) Assumptions about domain and continuity of the field:

The domain of analyticity needs to be enlarged in order to contain real points (also called Jost's points). Under Poincare symmetry, a general field transforms as

$$U(\Lambda, a)\phi_i(x)U(\Lambda, a)^\dagger = \sum S_{ij}(\Lambda^{-1})\phi_j(\Lambda x + a). \tag{3.56}$$

+ Scalar field: $U(\Lambda, a)\phi(x)U(\Lambda, a)^\dagger = \phi(\Lambda x + a)$.
+ Vector field: $U(\Lambda, a)A_\mu(x)U(\Lambda, a)^\dagger = \Lambda_\mu^\nu(\Lambda^{-1})A_\nu(\Lambda x + a)$.
+ Dirac field: $U(\Lambda, a)\psi_\alpha(x)U(\Lambda, a)^\dagger = \sum_{\beta=1}^4 S(\Lambda^{-1})_{\alpha\beta}\psi_\beta(\Lambda x + a)$.

(4) Energy positivity:

Except for the zero energy level of vacuum, all physical states are required to have positive energy. This means that four-momenta p^μ must have a light-like nature, or in other words, lie in or on the forward light cone.

(5) Microscopic causality or local commutativity:

Microscopic causality requires that commutators or anti-commutators must vanish for all space-like point $(x - y)$

$$[\phi_i(x), \phi_j(y)]_\pm = 0, \quad \text{if} \quad (x - y)^2 < 0.$$

We now use the above axioms to prove the CPT theorem. The Wightman reconstruction theorem states that a quantum field theory is uniquely determined by its Wightman function $\mathcal{W}$ which is defined as vacuum expectation values of field operators

$$\mathcal{W}(\Delta x_1, \Delta x_2, \cdots, \Delta x_n) \equiv \langle 0|\phi(x_0)\phi(x_1)\cdots\phi(x_n)|0\rangle, \tag{3.57}$$

where $\Delta x_i = x_{i-1} - x_i$, x_i are physical spacetime points. With the light of Wightman reconstruction theorem, we do not directly works with field operators but rather with ordinary function $\mathcal{W}$ only. If $\mathcal{W}$ is conserved under CPT, so will the corresponding quantum field theory. With the help of equations (3.44) and (3.49), the CPT operator applied for Wightman function corresponding to scalar fields $\phi(x)$ is

$$
\begin{aligned}
\mathcal{W}(\Delta x_1, \Delta x_2, \cdots, \Delta x_n) \quad &= \quad \langle 0|\phi(x_0)\phi(x_1)\cdots\phi(x_n)|0\rangle \\
&\xrightarrow{CPT} \quad \langle 0|\phi^\dagger(-x_0)\phi^\dagger(-x_1)\cdots\phi^\dagger(-x_n)|0\rangle^* \\
&= \quad \langle 0|[\phi(-x_n)\phi(-x_{n-1})\cdots\phi(-x_0)]^\dagger|0\rangle^* \\
&= \quad \langle 0|\phi(-x_n)\phi(-x_{n-1})\cdots\phi(-x_0)|0\rangle \\
&= \quad \mathcal{W}(\Delta x_n, \Delta x_{n-1}, \cdots, \Delta x_1). \tag{3.58}
\end{aligned}
$$

This is what we need to prove. The Wightman function associated to scalar fields

under axiom (2) and (3) transforms as

$$
\begin{aligned}
\mathcal{W}(\Delta x_1, \cdots, \Delta x_n) &= \langle 0|\phi(x_0)\phi(x_1)\cdots\phi(x_n)|0\rangle \\
&= \langle 0|U^\dagger(\Lambda, a)U(\Lambda, a)\phi(x_0)\phi(x_1)\cdots\phi(x_n)U^\dagger(\Lambda, a)U(\Lambda, a)|0\rangle \\
&= \langle 0|\phi(\Lambda x_0 + a)\phi(\Lambda x_1 + a)\cdots\phi(\Lambda x_n + a)|0\rangle \\
&= \mathcal{W}(\Lambda\Delta x_1, \cdots, \Lambda\Delta x_n), \quad \text{for real} \quad x_i, \Lambda.
\end{aligned}
\tag{3.59}
$$

By requiring positivity of energy, we can expand above expression applied for complex Δz_i in *extended tube* which is a set of complex Lorentz transformations

$$
\begin{aligned}
\mathcal{W}(\Delta z_1, \cdots, \Delta z_n) &= \mathcal{W}(\Lambda_c\Delta z_1, \cdots, \Lambda_c\Delta z_n) \\
&= \mathcal{W}(-\Delta z_1, \cdots, -\Delta z_n), \quad \text{for complex} \quad z_i, \Lambda_c.
\end{aligned}
\tag{3.60}
$$

Now complex Lorentz transformations Λ_c can also acts on complex Δz_i to give real four vector called Jost points $\Delta y_i = \Lambda_c\Delta z_i$. The equation (3.60) can be rewritten for physical Jost points Δy_i as

$$
\mathcal{W}(\Delta y_1, \cdots, \Delta y_n) = \mathcal{W}(-\Delta y_1, \cdots, -\Delta y_n).
\tag{3.61}
$$

Therefore at Jost points we have

$$
\begin{aligned}
\mathcal{W}(\Delta y_1, \cdots, \Delta y_n) &= \langle 0|\phi(y_0)\phi(y_1)\cdots\phi(y_n)|0\rangle \\
&= \langle 0|\phi(-y_0)\phi(-y_1)\cdots\phi(-y_n)|0\rangle \\
&= \langle 0|\phi^\dagger(-y_n)\phi^\dagger(-y_{n-1})\cdots\phi^\dagger(-y_0)|0\rangle^* \\
&= \langle 0|\phi^\dagger(-y_0)\phi^\dagger(-y_1)\cdots\phi^\dagger(-y_n)|0\rangle^* \quad \text{(for scalar fields)} \\
&= \langle 0|[\phi(-y_n)\phi(-y_{n-1})\cdots\phi(-y_0)]^\dagger|0\rangle^* \\
&= \langle 0|\phi(-y_n)\phi(-y_{n-1})\cdots\phi(-y_0)|0\rangle \\
&= \mathcal{W}(\Delta y_n, \cdots, \Delta y_1).
\end{aligned}
\tag{3.62}
$$

This result can be generalized for any physical spacetime position Δx_i, that is

$$
\mathcal{W}(\Delta x_1, \cdots, \Delta x_n) = \mathcal{W}(\Delta x_n, \cdots, \Delta x_1).
\tag{3.63}
$$

3.3 Testing CP invariance with neutrino oscillation experiments

3.3.1 Testing CP invariance in neutrino oscillation

As we already know in the SM, neutrinos are left-handed particles, while antineutrinos are right-handed. If CP symmetry is conserved in the lepton sector, the oscillation probabilities of the neutrino and antineutrino must be identical if the CPT symmetry holds

$$
P(\nu_\alpha \to \nu_\beta) = P(\overline{\nu}_\alpha \to \overline{\nu}_\beta).
\tag{3.64}
$$

From (1.41) and (1.42), the CP asymmetry is defined as the difference between the neutrino and antineutrino oscillation probabilities

$$
\begin{aligned}
\mathcal{A}_{\text{CP}} &= P(\nu_\alpha \to \nu_\beta) - P(\bar{\nu}_\alpha \to \bar{\nu}_\beta) \\
&= 4 \sum_{i>j} Im\left[U^*_{\alpha i} U_{\beta i} U_{\alpha j} U^*_{\beta j}\right] \sin\left(\frac{\Delta m^2_{ij}}{2E} L\right).
\end{aligned} \tag{3.65}
$$

If CP is violated, $\mathcal{A}_{\text{CP}}$ must be nonzero, or equivalently $U^*_{\alpha i} U_{\beta i} U_{\alpha j} U^*_{\beta j}$ has to contain an imaginary component. For $\alpha = \mu$ and $\beta = e$, then

$$
\begin{aligned}
\mathcal{A}_{\text{CP}} &= P(\nu_\mu \to \nu_e) - P(\bar{\nu}_\mu \to \bar{\nu}_e) \\
&= 4 \sum_{i>j} Im\left[U^*_{\mu i} U_{e i} U_{\mu j} U^*_{e j}\right] \sin\left(\frac{\Delta m^2_{ij}}{2E} L\right) \\
&= 16 c_{12} s_{12} c^2_{13} s_{13} c_{23} s_{23} \sin\delta_{CP} \sin\frac{\Delta m^2_{21} L}{4E} \sin\frac{\Delta m^2_{31} L}{4E} \sin\frac{\Delta m^2_{32} L}{4E}. \tag{3.66}
\end{aligned}
$$

In equation (3.66), Jarlskog invariant J, a quantity for evaluating CP violation that is independent of parameterization, is defined as

$$
\begin{aligned}
J &= \sum_{i>j} Im\left[U^*_{\alpha i} U_{\beta i} U_{\alpha j} U^*_{\beta j}\right] \\
&= c_{12} s_{12} c^2_{13} s_{13} c_{23} s_{23} \sin\delta_{CP}. \tag{3.67}
\end{aligned}
$$

In the quark sector, Jarlskog invariant is measured precisely [12]

$$
J_{quark} = 3.08^{+0.15}_{-0.13} \times 10^{-5}. \tag{3.68}
$$

In the lepton sector, by inserting values of mixing angles measured by neutrino oscillation experiments from Table 3.1 in equation (3.67), we can calculate the Jarlskog invariant

$$
J_{lepton} \approx -2.25 \times 10^{-2}. \tag{3.69}
$$

From Fig. 3.1, we can see that CP violation in the quark sector is too small to explain the matter-antimatter asymmetry of the universe, while CP violation in the lepton sector (if confirmed, at least with current values of oscillation parameters) could well do so.

3.3.2   Testing CP invariance with T2K experiment

T2K is able to measure simultaneously the disappearance of muon (anti-)neutrinos and the appearance of electron (anti-)neutrinos from the flux of almost pure muon (anti-)neutrinos. While the data samples of the $\nu_\mu(\bar{\nu}_\mu)$ disappearance provide a precise measurement of the atmospheric neutrino parameters, $\sin^2 2\theta_{23}$ and Δm^2_{31}, the $\nu_e(\bar{\nu}_e)$ appearance rates are driven by $\sin^2 2\theta_{13}$ and sensitive to δ_{CP} and mass hierarchy (MH). T2K made an observation of electron neutrinos appearing from a muon

Parameter	Value
$\sin^2 \theta_{12}$	0.304
$\sin^2 \theta_{13}$	0.0212
$\sin^2 \theta_{23}$	0.528
Δm^2_{31}	$2.509 \times 10^{-3} eV^2$
Δm^2_{21}	$7.53 \times 10^{-5} eV^2$
δ_{CP}	-2.14
Mass hierarchy	Normal (NH)

Table 3.1: Values of oscillation parameters used in calculating Jarlskog invariant.
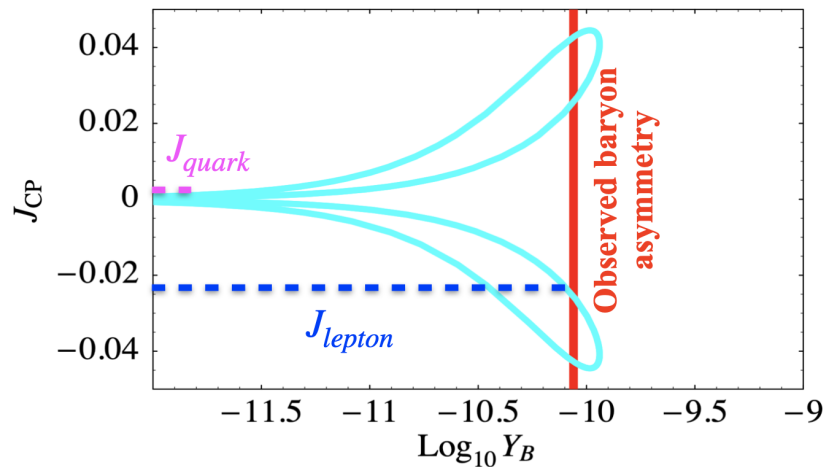
Figure 3.1: The Jarlskog invariant versus the baryon asymmetry varying $\delta_{CP} = [0, 2\pi]$ (cyan). The red region denotes the 2σ range for the baryon asymmetry. The magenta and blue lines indicate values of Jarlskog invariant in the quark and lepton sectors. The plot is taken from Ref. [9].
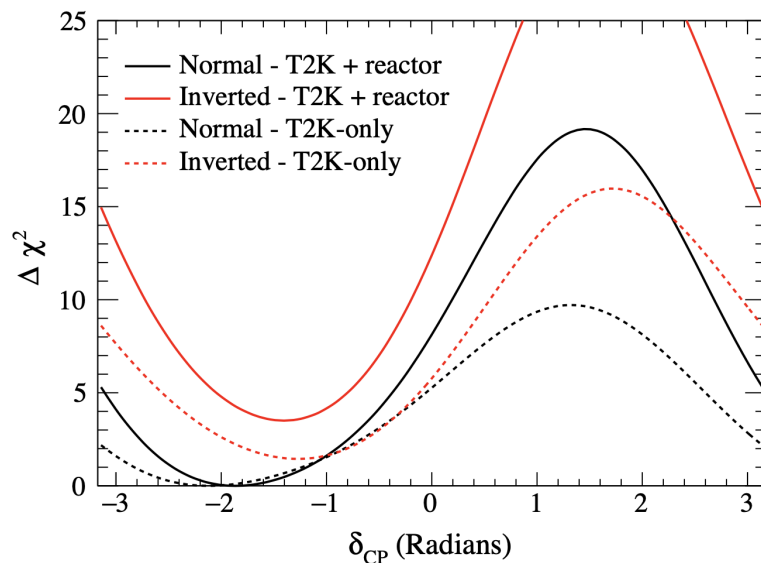
Figure 3.2: The $\Delta\chi^2$ distribution as a function of δ_{CP} for T2K, with and without reactor constraint.

	$1R_e$ ν mode	$1R_e$ $\overline{\nu}$ mode	$1R_e$ + 1de ν mode
$\nu_\mu \to \nu_e$	59.0	3.0	5.4
$\overline{\nu}_\mu \to \overline{\nu}_e$	0.4	7.5	0.0
Background	13.8	6.4	1.5
Total predicted	73.2	16.9	6.9
Systematic uncertainty	8.8%	7.1%	18.4%
Data	75	15	15

Table 3.2: The predicted number of events for $\delta_{CP} = -\pi/2$ and the measured number of events in the three electron-like samples at Super-K.

neutrino beam [78] and presented an indication of CP violation in the neutrino oscillation [18]. In this section, we will investigate the T2K ability to explore CP violation in the lepton sector by using neutrino oscillation measurements.

In 2020, T2K published a paper on Nature indicating CP violation in lepton sector [18]. In this analysis, T2K used data collected from 2009 to 2018 with a total exposure of 3.13×10^{21} POT in both neutrino mode (1.49×10^{21} POT) and antineutrino mode (1.64×10^{21}). Neutrinos are detected at the far detector Super-K via their weak interactions with target material (water). At a peak energy of 0.6 GeV, the dominant neutrino-nucleus interaction is charged current quasi-elastic (CCQE) scattering. CCQE interaction of neutrino (antineutrino) will produce charged lepton (antilepton) of the same flavour. Super-K can detect charged leptons (muons, electrons) with high precision, it is able to identify the flavour of incoming neutrinos. Table 3.2 summarizes the number of predicted events for $\delta_{CP} = -\pi/2$ and number of observed events at Super-K. The analysis indicates that δ_{CP} is near the maximal CP violating value $-\pi/2$. The CP conserving values $\delta_{CP} = 0$ and $\delta_{CP} = \pi$ are disfavoured at 95% C. L.

Recently, in 2021, the T2K experiment reported the updated measurements of neutrino and antineutrino oscillation using both appearance and disappearance channels [79]. This analysis used the same data-set collected at Super-K as the previous analysis reported in [18]. In the updated analysis, the event reconstruction algorithm is improved to match directly with the pattern of light observed in Super-K. This provides more information about the event, makes it easier to discriminate between the event categories, and improves the resolution of the lepton momentum and vertex location. The fiducial volume, therefore, can be significantly expanded, leading to more statistics, roughly equivalent to a 20% increase in statistics for the ν_e samples and a 40% reduction in the background contamination in the ν_μ samples. The new analysis also improves the theory of neutrino interaction models. The models of dominant CCQE and subdominant processes have been updated. The new analysis therefore provides more results than the previous one. Fig. 3.2 shows the distribution of $\Delta\chi^2$ function versus δ_{CP}, with and without constraint from reactor, for both neutrino mass hierarchy cases. The best-fit values and 1σ confidence intervals for δ_{CP} in both mass hierarchy

Parameters	NH	IH
δ_{CP} (T2K only)	$-2.14^{+0.90}_{-0.69}$	$-1.26^{+0.61}_{-0.69}$
δ_{CP} (T2K+reactor)	$-1.89^{+0.70}_{-0.58}$	$-1.38^{+0.48}_{-0.55}$

Table 3.3: The best fit and best fit $\pm 1\sigma$ intervals of δ_{CP} for T2K only and T2K+reactor for normal (NH) and inverted (IH) hierarchies. The $\pm 1\sigma$ interval corresponds to the values for which $\Delta\chi^2 \leq 1$.

Parameter	Best fit$\pm 1\sigma$
$\sin^2\theta_{12}$	$0.310^{+0.013}_{-0.012}$
$\sin^2\theta_{13}(\times 10^{-2})$	$2.241^{+0.067}_{-0.066}$
$\sin^2\theta_{23}$	$0.558^{+0.020}_{-0.033}$
$\delta_{CP}(^\circ)$	222^{+38}_{-28}
$\Delta m^2_{21}(10^{-5}\text{eV}^2/c^4)$	$7.39^{+0.21}_{-0.20}$
$\Delta m^2_{31}(10^{-3}\text{eV}^2/c^4)$	$2.523^{+0.032}_{-0.030}$

Table 3.4: Nominal values of oscillation parameters used for study in Section 3.3.3. *Normal* mass hierarchy is assumed.

scenarios are summarized in Table 3.3, with and without constraint from $\sin^2\theta_{13}$ from reactors.

3.3.3 Sensitivity to CP violation with a joint fit of T2K-II, NOvA-II, and JUNO

The content of this section is based on some parts of our study in the paper [80]. Accordingly, we will present the sensitivity to CP violation by combining the data from the three experiments, T2K-II, NOνA-II, and JUNO. The study in this section is done with the oscillation parameters available in Ref. [2, 81], which is briefly summarized in Table 3.4.

Searching for CP violation and measuring the value of δ_{CP} depend on the ability to resolve the parameter degeneracies among δ_{CP}, the sign of $|\Delta m^2_{31}|$, θ_{13}, and θ_{23} [82]. Combining the data samples of the accelerator-based long baseline experiments (T2K-II and NOνA-II) and JUNO would enhance the CP violation search and MH determination since the JUNO sensitivity to MH has no ambiguity to δ_{CP}. To further enhance the CP violation search, one can break the δ_{CP}-θ_{13} degeneracy by using the constraint of θ_{13} from reactor-based short-baseline (R-SBL) neutrino experiments such as Daya Bay [83], Double Chooz [84], and RENO [85]. This combination also helps to solve the θ_{23} octant in the case of non-maximal mixing.

GLoBES setup for simulating T2K-II, NOνA-II, and JUNO experiments

General Long Baseline Experiment Simulator (GLoBES) [86, 87] is a software package used to simulate neutrino oscillation phenomenon in accelerator-based long

baseline and reactor-based experiments. In GLoBES, the experiments are described by Abstract Experiment Definition Language (AEDL) files which contain information of the experiments including fluxes, cross sections, efficiencies, oscillation channels, backgrounds, energy resolutions, energy ranges and bin widths, detector setup, as well as source power. The output information including oscillation probabilities, event rates, and χ^2 values can be extracted by a C-library.

The AEDL allows GLoBES to incorporate different experiment setups within one data structure. The experiment setup is implemented into the experiment definition by three abstraction levels (Fig. 3.3): *channel, rule*, and *experiment*. A *channel* specifies the link between a specific neutrino flavor produced at the source and a reconstructed neutrino flavor detected at the detector. A *rule* consists of several *channels* which are defined as "signal" and "background" oscillation channels. Number of events of each *rule* is the sum of all *channels* in the *rule*. The χ^2 value of each *rule* is then calculated and the total χ^2 of one experiment is the sum of all χ^2's of all *rule*.

χ^2 is a function of all oscillation parameters which is used to measure the difference between the spectral of *test parameters* and the spectral of *true parameters*. The smaller χ^2 is, the better matching between the two spectra. The GLoBES built-in χ^2 function is defined by a Gaussian statistics

$$\chi^2 = \sum_{i}^{\text{\# of bin}} \frac{(O_i - T_i)^2}{O_i}, \tag{3.70}$$

where O_i is the event rate for the i-th bin at far detector, calculated for the assumed *true values* of the oscillation parameters, T_i is the event rate for the *test values* of the oscillation parameters.

In some experiments which have multi-detector setup such as reactor-based experiment JUNO or RENO, the GLoBES built-in χ^2 function is not sufficient to handle the systematical errors that are correlated between different detectors. In this cases, user-defined systematics can be used to replace the default χ^2 function of GLoBES

$$\chi^2 = \sum_{i}^{\text{\# of bin}} \sum_{d=N,F} \frac{(O_{d,i} - (1 + a_R + a_d)T_{d,i})^2}{O_{d,i}} + \frac{a_R^2}{\sigma_R^2} + \frac{a_N^2}{\sigma_N^2} + \frac{a_F^2}{\sigma_F^2}, \tag{3.71}$$

where, N and F are corresponding to *near* and *far* detectors. a_R, a_N, and a_F are the uncertainties in the reactor flux and the fiducial mass of the two detectors. σ_R, σ_N, and σ_F are the standard deviations of the central values which are assumed to be zero.

In each specific situation, the $\Delta\chi^2$ is defined accordingly. For example, in searching for CP violation, $\Delta\chi^2 = \chi^2(\delta_{CP} = 0, \pm\pi) - \chi^2(\text{true } \delta_{CP})$ to exclude CP conservation. The statistical significane of a measurement is defined as the squared root of the $\Delta\chi^2$ in terms of σ C. L. value

$$\sigma = \sqrt{\Delta\chi^2}. \tag{3.72}$$

In our study in this section and the following sections, we use GLoBES to simulate experiments and calculating the statistical significance. We describe the ex-
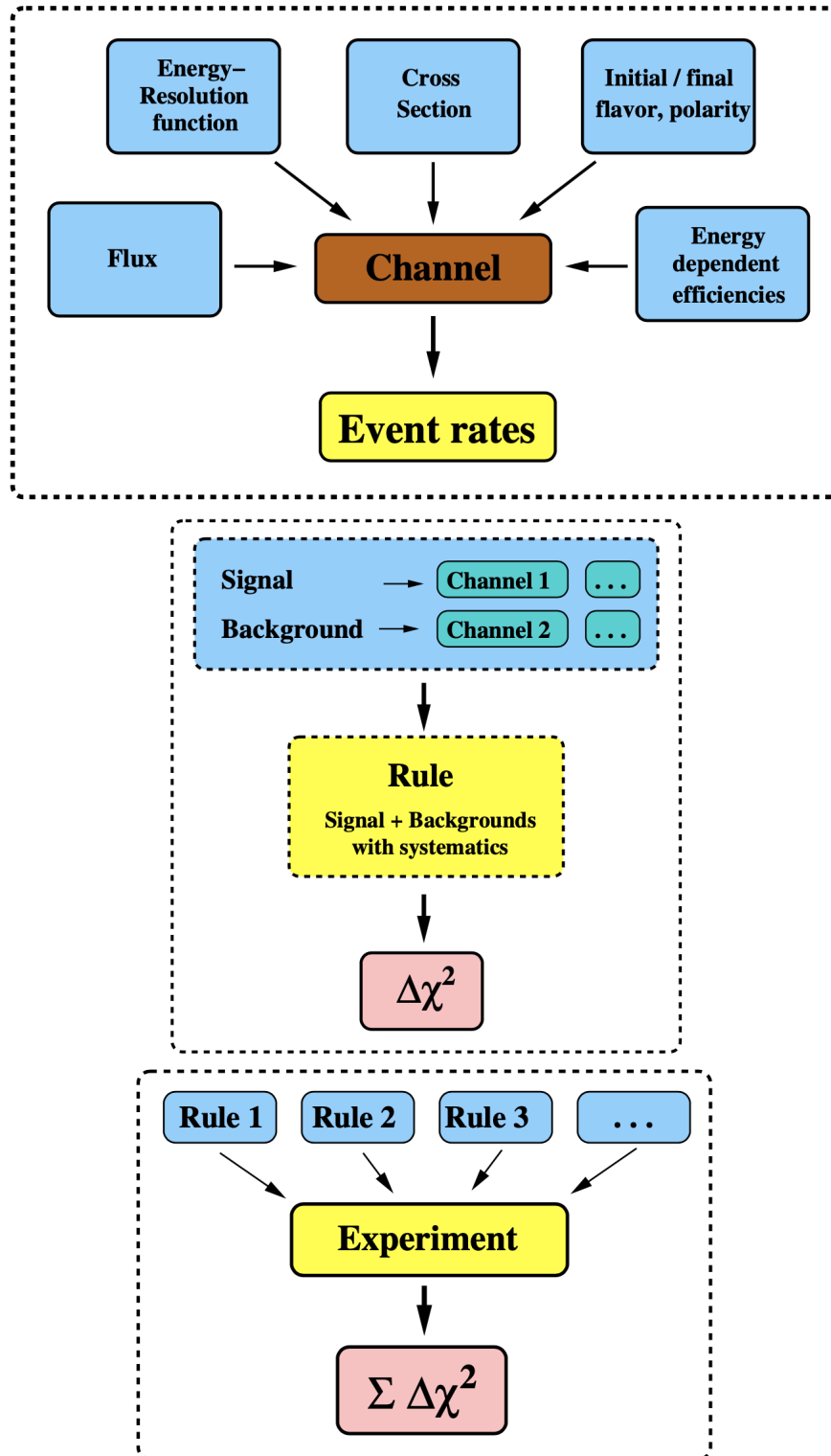
Figure 3.3: The abstract levels which define the AEDL file.

Characteristics	T2K-II [10, 46]	NOνA-II [51, 53]
Baseline	295 km	810 km
Matter density [88]	2.6 g/cm^3	2.84 g/cm^3
Total Exposure	20×10^{21} POT	72×10^{20} POT
Detector fiducial mass	22.5 kton	14 kton
Systematics	3% (0.01%)	5% (2.5%)
Energy resolution	$0.03 \times \sqrt{E(GeV)}$	$x \times \sqrt{E(GeV)}$
Energy window APP (DIS)	0.1-1.3 GeV (0.2-5.05 GeV)	0.0-4.0 GeV (0.0-5.0 GeV)
Bin Width APP (DIS)	0.125 GeV/bin (0.1 GeV/bin)	0.5 GeV/bin (0.1 GeV/bin)

Table 3.5: Experimental specifications of T2K-II and NOνA-II in GLoBES.

		$\nu_\mu \to \nu_e$	$\bar{\nu}_\mu \to \bar{\nu}_e$	ν_μ CC	$\bar{\nu}_\mu$ CC	ν_e CC	$\bar{\nu}_e$ CC	NC
T2K-II	ν mode	65.5	46.2	0.02	0.02	19.8	19.8	0.41
	$\bar{\nu}$ mode	45.8	70.7	0.01	0.01	17.5	17.5	0.45
NOνA-II	ν mode	62.0	38.0	0.15	–	79.0	69.0	0.87
	$\bar{\nu}$ mode	25.0	67.0	0.14	0.05	20.7	40.7	0.51

Table 3.6: Detection efficiencies(%) of $\nu_e/\bar{\nu}_e$ events in appearance samples. Normal hierarchy and $\delta_{CP} = 0$ are assumed.

periments using updated information on fluxes, signal and background efficiencies, and systematic errors. Remaining differences between the energy spectra of the simulated data sample at the reconstruction level obtained by GLoBES and the real experiment simulation can be due to the effects of the neutrino interaction model, the detector acceptance, detection efficiency variation as a function of energy, etc... These differences are then treated quantitatively using post-smearing efficiencies, allowing us to match our simulation with the published spectra of each simulated sample from each experiment. Each experimental setup is validated at the event rate level and sensitivity level to ensure that the physics reaches of the simulated data samples we obtain are in relatively good agreement with the real experimental setup.

For each of T2K-II and NOνA-II, four simulated data samples per each experiment are used: $\nu_\mu(\bar{\nu}_\mu)$ disappearance and $\nu_e(\bar{\nu}_e)$ appearance in both ν mode and $\bar{\nu}$ mode. The experimental specifications of these two experiments are shown in Table 3.5, in which APP and DIS are shortened for the appearance sample and the disappearance sample, respectively. The values of x for NOνA-II are defined as $x = 0.107, 0.091, 0.088$ and 0.081 for ν_e, ν_μ, $\bar{\nu}_e$ and $\bar{\nu}_\mu$, respectively. The systematics indicates normalization (calibration) error for both signals and backgrounds. Detection efficiencies[1] of $\nu_e/\bar{\nu}_e$ events in appearance samples and $\nu_\mu/\bar{\nu}_\mu$ events in disappearance samples are listed in Table 3.6 and Table 3.7, respectively.

---

[1]defined per each interaction channel as the ratio of selected events in the data sample to the totally simulated interaction supposed to happen in the detector

		ν_μ	ν_μ	$\bar{\nu}_\mu$	$\bar{\nu}_\mu$	$(\nu_e + \bar{\nu}_e)$	NC	$\nu_\mu \to \nu_e$
		CCQE	CC non-QE	CCQE	CC non-QE	CC	NC	
T2K-II	ν mode	71.2	20.4	71.8	20.4	0.84	2.7	0.84
	$\bar{\nu}$ mode	65.8	24.5	77.5	24.5	0.58	2.5	0.58
NOνA-II	ν mode	31.2		27.0		–	0.44	–
	$\bar{\nu}$ mode	33.9		20.5		–	0.33	–

Table 3.7: Detection efficiencies(%) of $\nu_\mu/\bar{\nu}_\mu$ events in disappearance samples. Normal hierarchy is assumed.

In T2K(-II), neutrino events are dominated by the Charged Current Quasi-Elastic (CCQE) interactions. Thus, for appearance (disappearance) in ν mode and $\bar{\nu}$ mode, the signal events are obtained from the $\nu_\mu \to \nu_e$ ($\nu_\mu \to \nu_\mu$) CCQE events and $\bar{\nu}_\mu \to \bar{\nu}_e$ ($\bar{\nu}_\mu \to \bar{\nu}_\mu$) CCQE events, respectively. In the appearance samples, the intrinsic $\nu_e/\bar{\nu}_e$ contamination from the beam, the *wrong-sign* components i.e $\bar{\nu}_\mu \to \bar{\nu}_e$ ($\nu_\mu \to \nu_e$) in ν ($\bar{\nu}$) mode respectively, and the neutral current (NC) events constitute the backgrounds. In the disappearance samples, the backgrounds come from $\nu_\mu, \bar{\nu}_\mu$ CC interaction excluding CCQE, hereby called CC-nonQE, and NC interactions. We use the updated T2K flux released along with Ref. [89]. In simulation, the cross section for low and high energy regions are taken from Ref. [90] and Ref. [91] respectively. In our T2K-II set-up, an exposure of 20×10^{21} POT equally divided among the ν mode and $\bar{\nu}$ mode is considered along with a 50% effectively statistic improvement as presented in Ref. [46]. The signal and background efficiencies and the spectral information for T2K-II are obtained by scaling the T2K analysis reported in Ref. [10] to same exposure as the T2K-II proposal. In Fig. 3.4, the T2K-II expected spectra of the signal and background events as a function of reconstructed neutrino energy obtained with GLoBES are compared to those of the Monte-Carlo simulation scaled from Ref. [46]. A 3% error is assigned for both the energy resolution and the normalization uncertainties of the signal and background in all simulated samples.

For NOνA-II, we consider a total exposure of 72×10^{20} POT equally divided among ν mode and $\bar{\nu}$ mode [53]. We predict the neutrino fluxes at the NOνA far detector by using the flux information from the near detector given in Ref. [92] and normalizing it with the square of their baseline ratio. A 5% systematic error for all samples and 8-10% sample-dependent energy resolution are assigned. Significant background events in the appearance samples stem from the intrinsic beam $\nu_e/\bar{\nu}_e$, NC components, and cosmic muons. In the appearance sample of the $\bar{\nu}$ mode, *wrong-sign* events from ν_e appearance events are included as the backgrounds in the simulation. We use the reconstructed energy spectra of the NOνA far detector simulated sample reported in Ref. [93] to tune our GLoBES simulation. The low- and high-particle identification (PID) score samples are used but not the peripheral samples since the reconstructed energy information is not available. In the disappearance samples of
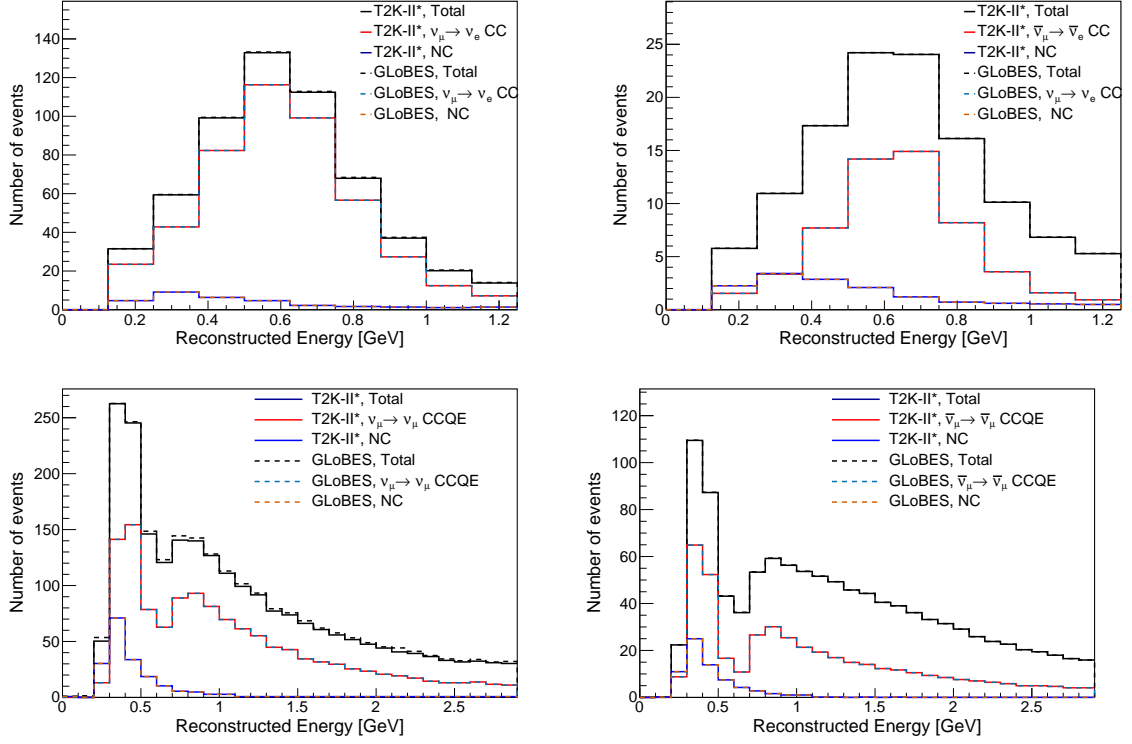
Figure 3.4: Expected event spectra of the signal and background as a function of reconstructed neutrino energy for T2K-II. The top (bottom) spectra are for the appearance (disappearance) samples and the left (right) spectra are for ν ($\bar{\nu}$) mode. Same oscillation parameters as Ref. [10] are used.
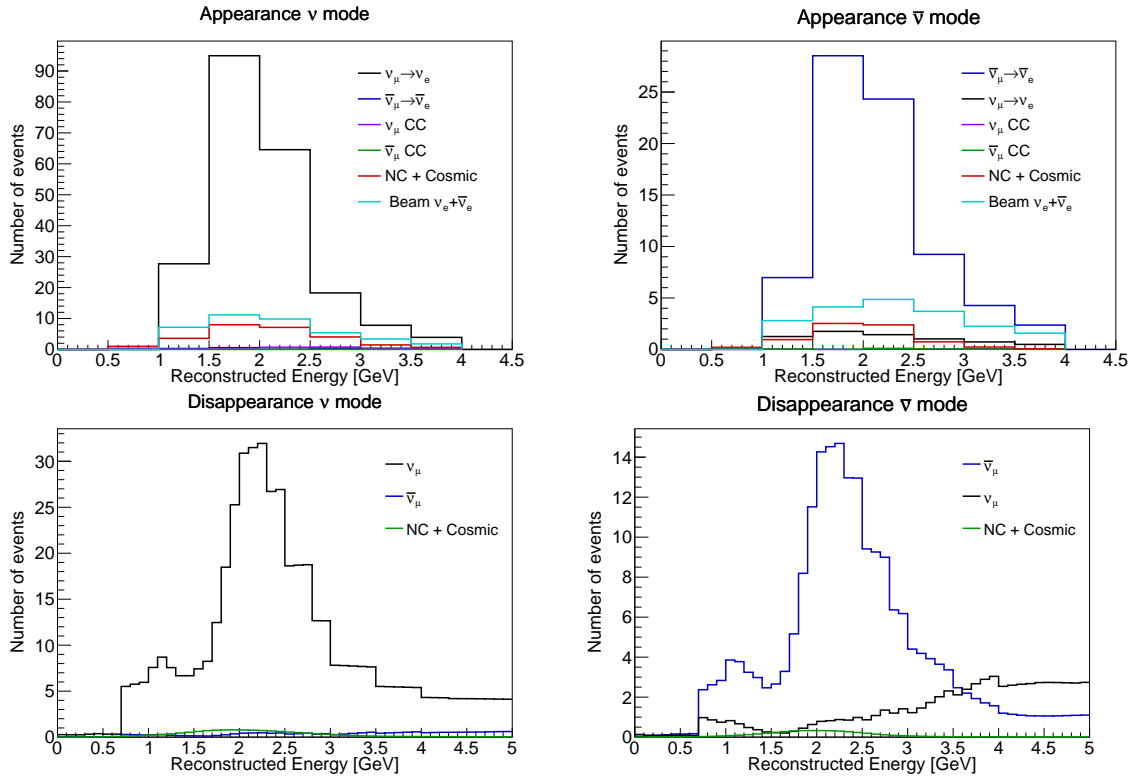
Figure 3.5: Expected event spectra of the signal and background as a function of reconstructed neutrino energy for NOνA-II. The top (bottom) spectrum is for the appearance (disappearance) channel and the left (right) spectrum is for ν ($\bar{\nu}$) mode. *Normal* MH, $\delta_{\rm CP} = 0$, and other oscillation parameters given in Tab. 3.1 are assumed.

Characteristics	Inputs
Baseline	52.5 km
Density	2.6 g/cm^3 [95]
Detector type	Liquid Scintillator
Detector mass	20 kton
$\bar{\nu}_e$ Detection Efficiency	73%
Running time	6 years
Thermal power	36 GW
Energy resolution	3% $/\sqrt{E \, (\text{MeV})}$
Energy window	1.8-9 MeV
Number of bins	200

Table 3.8: JUNO simulated specifications in GLoBES.

both ν mode and $\bar{\nu}$ mode, events from both CC ν_μ and $\bar{\nu}_\mu$ interactions are considered as signal events, which is tuned to match with the NOνA far detector simulated signal given an identical exposure. Background from the NC ν_μ ($\bar{\nu}_\mu$) interactions is taken into consideration and weighted such that the rate at a predefined exposure is matched to a combination of the reported NC and cosmic muon backgrounds in Ref. [93]. Fig. 3.5 shows the simulated NOνA-II event spectra as a function of reconstructed neutrino energy, for ν_e appearance and ν_μ disappearance channels in both ν mode and $\bar{\nu}$ mode, where *normal* MH is assumed, δ_{CP} is fixed at $0°$, and other parameters are given in Table 3.1.

In JUNO, the electron anti-neutrino $\bar{\nu}_e$ flux, which is produced mainly from four radioactive isotopes ^{235}U, ^{238}U, ^{239}Pu, and ^{241}Pu [94], is simulated with an assumed detection efficiency of 73%. The backgrounds, which have a marginal effect on the MH sensitivity, are not included in our simulation. In our setup, to speed up the calculation, we consider one core of 36 GW thermal power with an average baseline of 52.5 km instead of the true distribution of the reactor cores, baselines, and powers. The simulated JUNO specification is listed in Table 3.8. The contribution of the event rate of four isotopes as a function of the neutrino energy is shown in Fig. 3.6. For systematic errors, we use 1% commonly for the errors associated with the uncertainties of the normalization of the $\bar{\nu}_e$ flux produced from the reactor core, the normalization of the detector mass, the spectral normalization of the signal, the detector response to the energy scale, the isotopic abundance, and the bin-to-bin reconstructed energy shape.

Besides T2K-II, NOνA-II, and JUNO, we implement a R-SBL neutrino experiment to constrain $\sin^2\theta_{13}$ at 3% uncertainty, which is reachable as prospected in Ref. [96]. This constraint is important to break the parameter degeneracy between δ_{CP}-θ_{13}, which is inherent from the measurement with the electron (anti-)neutrino appearance samples in the A-LBL experiments.

To calculate the sensitivity, a joint χ^2 is formulated by summing over all individual experiments under consideration without taking into account any systematic correlation among experiments. For T2K-II and NOνA-II, we use a built-in χ^2 function (equation 3.70) from GLoBES for taking the signal and background normalization systematics with the spectral distortion into account. For JUNO, an user-defined formula for χ^2 (equation 3.71) is used. For a given *true* value of the oscillation parameters, $\vec{\Theta}_{\text{truth}} = (\theta_{12}, \theta_{13}, \theta_{23}, \delta_{\text{CP}}; \Delta m_{21}^2, \Delta m_{31}^2)_{\text{truth}}$, at a *test* set of oscillation parameters, $\vec{\Theta}_{\text{test}}$, and systematic variations $\vec{s}_{\text{syst.}}$, a measure $\chi^2(\vec{\Theta}_{\text{truth}}|\vec{\Theta}_{\text{test}}, \vec{s}_{\text{syst.}})$ is calculated. It is then minimized over the nuisance parameters (both systematic parameters and marginalized oscillation parameters) to obtain the statistical significance on the hyperplane of parameters of interest.

CP violation sensitivity with the joint fit of T2K-II, NOνA-II, and JUNO

The statistical significance $\sqrt{\Delta\chi^2}$ to exclude the CP-conserving values ($\delta_{\text{CP}} = 0, \pi$) or sensitivity to CP violation is evaluated for any *true* value of δ_{CP} with the *normal* MH assumed. For the minimization of χ^2 over the MH options, we consider two cases: (i) MH is *known* and *normal*, same as the truth value or (ii) MH is *unknown*. Fig. 3.7 shows the CP violation sensitivity as a function of the *true* value of δ_{CP} for both MH options obtained by different analyses: (i) T2K-II only; (ii) a joint T2K-II and R-SBL experiments; (iii) a joint of T2K-II, NOνA-II and R-SBL experiments; and (iv) a joint of T2K-II, NOνA-II, JUNO and R-SBL experiments. The result shows that whether the MH is *known* or *unknown* affects the first three analyses, but not the fourth. This is because, as concluded in the above section, the MH can be determined conclusively with a joint analysis of all considered experiments. It can be seen that the sensitivity to CP violation is driven by T2K-II and NOνA-II. Contribution of the R-SBL neutrino experiment is significant only at the region where δ_{CP} is between 0 and π and when the MH is not determined conclusively. JUNO further enhances the CP violation sensitivity by lifting up the overall MH sensitivity and consequently breaking the MH-δ_{CP} degeneracy. At δ_{CP} close to $-\pi/2$, which is indicated by recent T2K data [18], the sensitivity of the joint analysis with all considered experiments can reach approximately the 5σ C.L. We also calculate the statistical significance of the CP violation sensitivity as a function of *true* δ_{CP} at different values of θ_{23}, as shown in Fig. 3.8. When *inverted* MH is assumed, although A_{CP} amplitude fluctuates in the same range as when *normal* MH, that the probability and rate of ν_e appearance becomes smaller make the statistic error, $\sigma_{\nu_e}^{\text{stat.}}$, lower. In sum, sensitivity to CP violation, which is proportional to $A_{\text{CP}}/\sigma_{\nu_e}^{\text{stat.}}$, is slightly higher if the *inverted* MH is assumed to be *true* as shown at the right of the Fig. 3.8.

Table 3.9 shows the fractional region of all possible *true* δ_{CP} values for which we can exclude CP conserving values of δ_{CP} to at least the 3σ C.L., obtained by the joint analysis of all considered experiments. Due to the fact that the MH is resolved
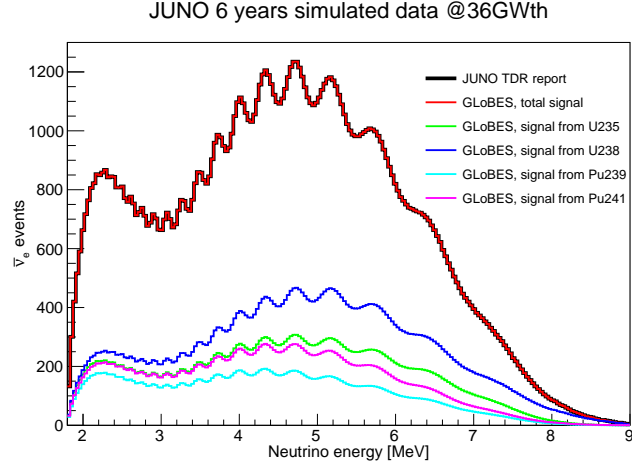
Figure 3.6: JUNO event rate calculated at same oscillation parameters as Ref. [11].
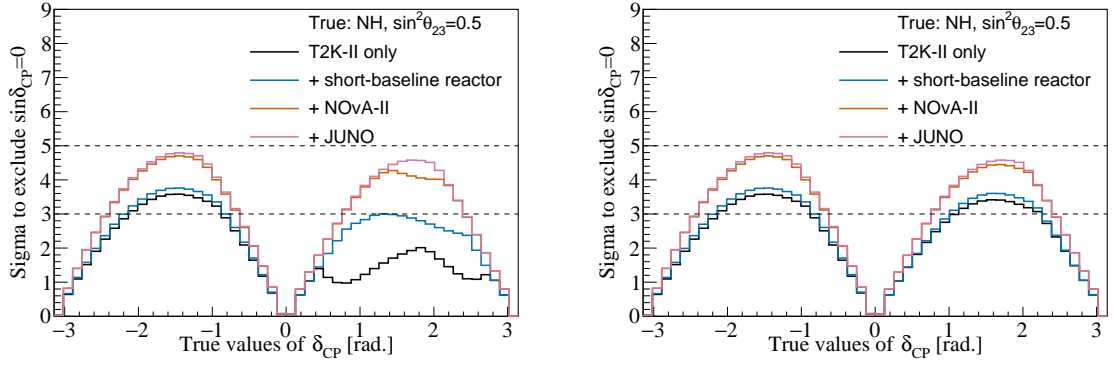
Figure 3.7: CP violation sensitivity as a function of the *true* δ_{CP} obtained with different analyses. *Normal* MH and $\sin^2 \theta_{23} = 0.5$ are assumed to be *true*. Left (right) plot is with the MH assumed to be *unknown* (*known*) in the analysis, respectively.
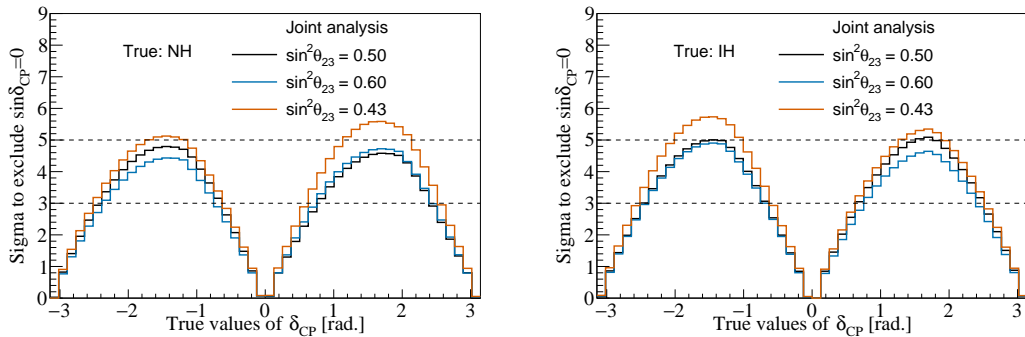
Figure 3.8: CP violation sensitivity as a function of the *true* δ_{CP} obtained with a joint analysis of all considered experiments at different *true* $\sin^2 \theta_{23}$ values (0.43, 0.5, 0.6). Left (right) plot is with the *normal* (*inverted*) MH, respectively. MH is assumed to be *unknown* in the analysis.

Value of $\sin^2 \theta_{23}$	0.43	0.50	0.60
Fraction of *true* δ_{CP} values (%), NH	61.6	54.6	53.3
Fraction of *true* δ_{CP} values (%), IH	61.7	57.2	54.2

Table 3.9: Fractional region of δ_{CP}, depending on $\sin^2 \theta_{23}$, can be explored with 3σ or higher significance.

completely with the joint analysis, the CP violation sensitivities are quantitatively identical no matter whether the MH is assumed to be *known* or *unknown*.

3.4 Testing CPT invariance with neutrino oscillation experiments

3.4.1 Testing CPT invariance in neutrino oscillation

We consider an unitary, local, Lorentz-invariant quantum field theory with Hamiltonian H. The CPT transformation reads

$$\langle p|H|p \rangle \xrightarrow{CPT} \langle p|\Theta^{-1}\Theta H\Theta^{-1}\Theta|p \rangle = \langle \overline{p}|\Theta H \Theta^{-1}|\overline{p} \rangle = \langle \overline{p}|H|\overline{p} \rangle. \tag{3.73}$$

The result in equation (3.73) shows that if the CPT symmetry is conserved, the particle and its anti-particle must have the same energy spectra. This is an important consequence of the CPT theorem that opens a possibility for direct testing CPT invariance by comparing the mass spectra, or other properties such as lifetime or magnetic moment of a particle and its antiparticle. In terms of relative precision, the most stringent constraint on the CPT violation was achieved on the neutral kaon system [12]

$$\left| \frac{m(K^\circ) - m(\overline{K}^\circ)}{m_K} \right| < 6 \times 10^{-19} \text{ at } 90\% \ C.L. \tag{3.74}$$

The bound on the $K^\circ - \overline{K}^\circ$ system seems so strong that there is very little room for CPT violation. However, it is pointed out in Ref. [27] that this may be misleading. The terms that appear in the Lagrangian and Einstein's mass-energy relation are mass squared instead of mass itself. In terms of mass squared difference, the bound in Eq.(3.74) becomes much weaker

$$|m^2(K^\circ) - m^2(\overline{K}^\circ)| < 0.3 \ eV^2. \tag{3.75}$$

From neutrino oscillation experiments, the mass-squared differences of neutrinos have been measured to be of order $\mathcal{O}(10^{-3})$ eV^2 and $\mathcal{O}(10^{-5})$ eV^2 [97]. We can see that in terms of the mass-squared difference, measurements on neutrino provide the best limit on the CPT violation but not neutral kaon [26, 27]. It is worth noting that the neutrino mass spectrum cannot be calculated solely from neutrino oscillations, but must be combined with cosmological constraints and beta decay, as recently discussed in Ref. [7]. Neutrinos, unlike neutral kaon mesons, are neutral elementary particles

and it is intriguing that this particle could be a Majorana particle, where neutrino and antineutrino are indistinguishable in the conventional sense of the CPT invariant paradigm. The neutrino nature under the CPT-violating scenario has been explored in Ref. [98]. Here we focus on the phenomenological consequence of the CPT violation in the observable neutrino oscillation.

In context of three-flavor PMNS framework [29, 99], neutrino oscillation is described by an unitary 3×3 matrix with six oscillation parameters including three mixing angles θ_{12}, θ_{13}, θ_{23}, one Dirac phase δ, and two mass squared differences Δm_{21}^2, Δm_{31}^2. Under CPT symmetry, the oscillation probabilities of neutrino and antineutrino are related as follows:

$$P(\nu_\alpha \to \nu_\beta) \xrightarrow{CPT} P(\overline{\nu}_\beta \to \overline{\nu}_\alpha) = P(\nu_\alpha \to \nu_\beta). \tag{3.76}$$

Although the T2K result is expected as a hint of CP violation [18], this is, however, with the assumption of CPT conservation. There is a CP-conserving CPT-violating scenario that can also explain the observation at T2K [100]. It is also stressed in Ref. [100] that before we can make a certain claim about CP violation at any level, we must rule out the CPT violation possibility at the same level first. If CPT is violated, the two sets of parameters are different for neutrinos and antineutrinos. Let's assume

$$P(\nu_\alpha \to \nu_\beta) = f(\theta_{12}, \ \theta_{13}, \ \theta_{23}, \ \delta, \ \Delta m_{21}^2, \ \Delta m_{31}^2), \tag{3.77}$$

for neutrino, and

$$P(\overline{\nu}_\alpha \to \overline{\nu}_\beta) = f(\overline{\theta}_{12}, \ \overline{\theta}_{13}, \ \overline{\theta}_{23}, \ \overline{\delta}, \ \Delta\overline{m}_{21}^2, \ \Delta\overline{m}_{31}^2), \tag{3.78}$$

for antineutrino. The differences between the parameters of the two sets indicate CPT violation in the lepton sector. The CPT violation was triggered to explain the anomaly in the short-baseline neutrino experiment, in Ref. [27]. It is provided in Ref. [100] the most recent update at 3σ on the bounds of CPT violation with neutrino experiment analysis.

$$
\begin{aligned}
|\delta_{\nu\overline{\nu}}(\sin^2\theta_{12})| &< 0.14, \\
|\delta_{\nu\overline{\nu}}(\sin^2\theta_{13})| &< 0.029, \\
|\delta_{\nu\overline{\nu}}(\sin^2\theta_{23})| &< 0.19, \\
|\delta_{\nu\overline{\nu}}(\Delta m_{21}^2)| &< 4.7 \times 10^{-5} \ eV^2, \\
|\delta_{\nu\overline{\nu}}(\Delta m_{31}^2)| &< 2.5 \times 10^{-4} \ eV^2,
\end{aligned} \tag{3.79}
$$

where $|\delta_{\nu\overline{\nu}}(X)| = |X - \overline{X}|$ for the X oscillation parameter. The future long baseline neutrino oscillation experiment DUNE may exclude CPT conservation at 3σ C. L. and improve the bound on $\delta_{\nu\overline{\nu}}(\Delta m_{31}^2)$ to at least one order compared to its current value [101]

$$|\delta_{\nu\overline{\nu}}(\Delta m_{31}^2)| < 8.1 \times 10^{-5} \ eV^2 \text{ at } 3\sigma \text{ C. L.} \tag{3.80}$$
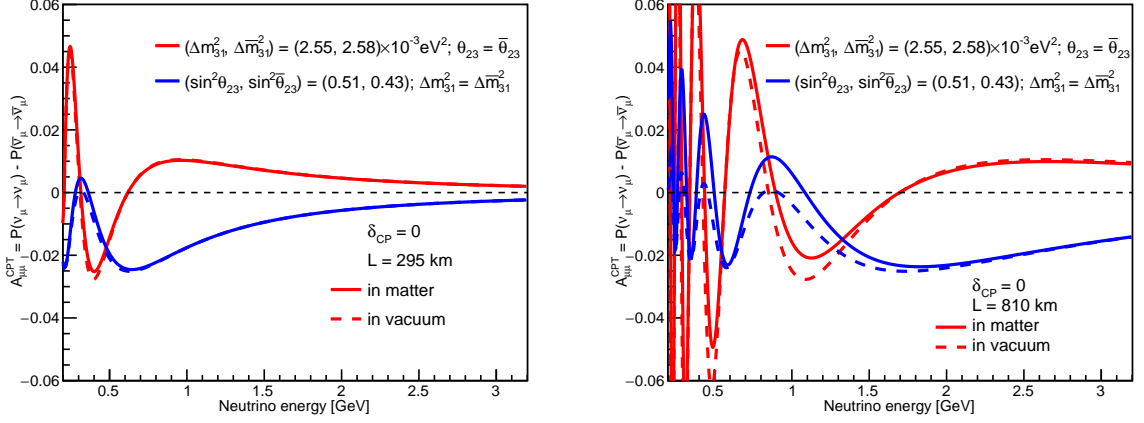
Figure 3.9: CPT asymmetries in disappearance channels at T2K baseline L = 295 km (left) and NOνA baseline L = 810 km (right). The differences in solid lines and dashed lines indicate extrinsic CPT effect caused by matter.

The difference in oscillation probabilities of neutrino and antineutrino can be evaluated as the CPT asymmetry

$$\mathcal{A}_{\alpha\beta}^{CPT} = P(\nu_\alpha \to \nu_\beta) - P(\overline{\nu}_\beta \to \overline{\nu}_\alpha). \qquad (3.81)$$

The asymmetry $\mathcal{A}_{\alpha\beta}^{CPT}$ in Eq. (3.81) may consist of two parts: *intrinsic* or *true* CPT asymmetry and *extrinsic* or *fake* CPT asymmetry caused by matter effect [102] [103] [104] [105] [106]. Fig. 3.9 demonstrates the CPT asymmetries in disappearance channels at T2K baseline (L = 295 km) and NOνA baseline (L = 810 km). The differences in solid lines and dashed lines indicate extrinsic CPT effect caused by matter. We can see from the plots that the matter effect is very small in disappearance channels. The extrinsic CPT asymmetry, therefore, can be neglected in the disappearance measurements. Current long-baseline neutrino oscillation experiments such as T2K and NOνA focus on four channels, including two appearance channels ($\nu_\mu \to \nu_e$, $\overline{\nu}_\mu \to \overline{\nu}_e$), and two disappearance channels ($\nu_\mu \to \nu_\mu$, $\overline{\nu}_\mu \to \overline{\nu}_\mu$). It can be seen from Eq. (3.81) that T2K and NOνA alone can test CPT invariance via their measurements of the disappearance channels which are sensitive to the atmospheric parameters $\Delta m_{31}^2, \Delta\overline{m}_{31}^2, \theta_{23}$, and $\overline{\theta}_{23}$. These experiments, therefore, are sensitive to the CPT asymmetric quantities $\mathcal{A}_{\mu\mu}^{CPT}(\sin^2\theta_{23})$ and $\mathcal{A}_{\mu\mu}^{CPT}(\Delta m_{31}^2)$.

In this section, we will investigate the possibility of testing CPT invariance with T2K and with the synergy of T2K-II, NOνA-II, and JUNO experiments. In which we focus only on the disappearance channels of T2K, T2K-II, and NOνA-II. Constraint on $\Delta\overline{m}_{31}^2$ from JUNO experiment can help to improve the sensitivity. We will show that the current T2K data indicates no CPT violation, while the combined analysis of T2K-II, NOνA-II, and JUNO can achieve the sensitivity levels of DUNE even before its starting by 2028.

3.4.2 GLoBES setup for simulating T2K-II, NOvA-II, and JUNO experiments

GLoBES [86, 87] is a flexible framework to simulate neutrino experiments. By default, GLoBES assumes that CPT symmetry holds. This means that the framework sets identical definitions and values of the oscillation parameters for neutrinos and anti-neutrinos in Eq. (3.77) and Eq. (3.78). We can modify or update the software in order to meet our needs or the realistic setup of the experiments. In our study, the oscillation framework was modified to include oscillation parameters for antineutrinos. For the oscillation probability formula, we follow Barger *et. al.* [107]. Neutrino (anti-neutrino) oscillation in matter now depends on nine variables, including six parameters listed in Eq. (3.77) for neutrino and Eq. (3.78) for antineutrino, as well as three additional parameters E_ν, L and ρ. Where E_ν, L and ρ respectively represent neutrino energy, distance travelled, and the matter density.

The similarity in configuration and operating principle of T2K and NOνA makes it interesting for joint fit. Both experiments use intense muon (anti-)neutrino beams created by accelerators to study oscillation phenomena. The off-axis technique can optimize the probabilities with a narrow-band beam of neutrinos at a defined low energy. The ability to focus positive or negative particles (mainly pion and kaon) makes them unique for operating in both neutrino-mode and anti-neutrino-mode. This important feature enables the testing of CPT invariance in accelerator-based neutrino oscillation experiments. JUNO [11] is a reactor-based medium baseline neutrino oscillation experiment which studies electron antineutrino disappearance ($\overline{\nu}_e \to \overline{\nu}_e$). The experiment uses electron anti-neutrino flux produced from nuclear reactors to study neutrino oscillation. With rich statistics, advanced improvements in electronics and calibration system, JUNO is able to reach energy resolution below 3% and better than 0.5% precision on $\sin^2 \overline{\theta}_{12}$, $\Delta \overline{m}_{21}^2$ and $|\Delta \overline{m}_{31}^2|$ [108]. It also can break neutrino mass hierarchy at 3σ after six years of operation, thus significantly contribute to the constraint on $\Delta \overline{m}_{31}^2$.

We basically follow the GLoBES setup for T2K-II, NOνA-II, and JUNO in the Ref. [80], which was described in detail in the Section 3.3.3, except for some modifications in T2K-II and JUNO. T2K is expected to operate until 2027, exposing 20×10^{21} protons-on-target (POT) in original proposal [46]. According to the latest plan, the statistics may be reduced to only one half of the primary plan [109]. We also updated the T2K flux, which was released in 2020 [110]. For JUNO, a total thermal of 26.6 GWth [108] is used instead of 36 GWth as in the previous report. Also, as mentioned above, the energy resolution is set at 2.9% [108] to reflect closely the JUNO's prospect. In our simulation, for T2K-II and NOνA-II, we used the disappearance channels only, with statistics equally divided for ν mode and $\overline{\nu}$ mode. For JUNO, $\overline{\nu}_e$ disappearance data is used. We assume neutrino masses are in normal ordering throughout the study in Sec. 3.4.4. The studies are done with the values of nominal parameters listed in Table 3.10, in which we follow the measurements of T2K [1] for atmospheric parameters

Parameter	Value
$\sin^2 \theta_{23}$	0.51
$\sin^2 \overline{\theta}_{23}$	0.43
Δm_{31}^2	$2.55 \times 10^{-3} \text{eV}^2$
$\Delta \overline{m}_{31}^2$	$2.58 \times 10^{-3} \text{eV}^2$
$\sin^2 \theta_{12}, \ \sin^2 \overline{\theta}_{12}$	0.318
$\sin^2 \theta_{13}, \ \sin^2 \overline{\theta}_{13}$	0.022
$\delta, \ \overline{\delta}$	1.08π rad
$\Delta m_{21}^2, \ \Delta \overline{m}_{21}^2$	$7.5 \times 10^{-5} \text{eV}^2$

Table 3.10: Values of nominal parameters used for the study in Section 3.4, taken from Ref. [1] and Ref. [2].

and global fit [2] for the rest.

The sensitivity to rule out CPT invariance hypothesis with $\delta_{\nu\overline{\nu}}(X)$ for X parameter is explored. The χ^2 of individual experiment is calculated for given true values of X and $\overline{X}$, where X can be $\sin^2 \theta_{23}$ or Δm_{31}^2. We use a GLoBES built-in χ^2 function (equation 3.70) for T2K-II and NOνA-II, while an user-defined formula is used for JUNO (equation 3.71) as mentioned in the previous section. The calculation of χ^2 is then minimized over the nuisance parameters except for X and $\overline{X}$. The two-dimensional distributions of $\Delta\chi^2$ which is the sum of all individual ones of the three experiments, are obtained (see Fig. 3.13). The minimum of $\Delta\chi^2$ as a function of $\delta_{\nu\overline{\nu}}(X)$ is then found. The statistical significance of excluding CPT conservation is expressed as the squared root of the minimum joint $\Delta\chi^2$.

3.4.3 Testing CPT invariance with T2K experiment

In 2017, T2K announced its measurements on θ_{23} and Δm_{23}^2 using 1.5×10^{21} POT [111] [112] in both neutrino mode (7.482×10^{20} POT) and antineutrino mode (7.471×10^{20} POT)

$$
\begin{aligned}
\sin^2(\theta_{23}) &= 0.51^{+0.08}_{-0.07} & \nu \text{ mode,} \\
\sin^2(\overline{\theta}_{23}) &= 0.42^{+0.25}_{-0.07} & \overline{\nu} \text{ mode,} \\
\Delta m_{32}^2 &= 2.53^{+0.15}_{-0.13} \times 10^{-3} \text{ eV}^2 & \nu \text{ mode,} \\
\Delta \overline{m}_{32}^2 &= 2.55^{+0.33}_{-0.27} \times 10^{-3} \text{ eV}^2 & \overline{\nu} \text{ mode.}
\end{aligned}
\tag{3.82}
$$

In this analysis, ν_μ and $\overline{\nu}_\mu$ oscillations are treated independently such that $\theta_{23} \neq \overline{\theta}_{23}$ and $\Delta m_{32}^2 \neq \Delta \overline{m}_{32}^2$ while keeping other parameters the same. An updated analysis using 3.13×10^{21} POT was done in Ref. [1]. This update analyzes disappearance channels using 1.49×10^{21} POT in neutrino mode and 1.64×10^{21} POT in antineutrino

mode with assuming normal mass hierarchy (NH).

$$\begin{aligned}
\sin^2(\theta_{23}) &= 0.51^{+0.06}_{-0.07} \quad \nu \text{ mode,} \\
\sin^2(\overline{\theta}_{23}) &= 0.43^{+0.21}_{-0.05} \quad \overline{\nu} \text{ mode,} \\
\Delta m^2_{32} &= 2.47^{+0.08}_{-0.09} \times 10^{-3} \text{ eV}^2 \quad \nu \text{ mode,} \\
\Delta \overline{m}^2_{32} &= 2.50^{+0.18}_{-0.13} \times 10^{-3} \text{ eV}^2 \quad \overline{\nu} \text{ mode.}
\end{aligned} \tag{3.83}$$

For NH of neutrinos, we have $\Delta m^2_{31} = \Delta m^2_{32} + \Delta m^2_{21}$. From equation (3.83), we can derive the values of Δm^2_{31} and $\Delta \overline{m}^2_{31}$ as follows:

$$\begin{aligned}
\Delta m^2_{31} &= 2.55^{+0.08}_{-0.09} \times 10^{-3} \text{ eV}^2 \quad \nu \text{ mode,} \\
\Delta \overline{m}^2_{31} &= 2.58^{+0.18}_{-0.13} \times 10^{-3} \text{ eV}^2 \quad \overline{\nu} \text{ mode.}
\end{aligned} \tag{3.84}$$

The following results are done with GLoBES simulation using 3.13×10^{21} POT. Fig. 3.10 shows the distributions of $\Delta\chi^2$ as a function of Δm^2_{31} (left) and $\sin^2\theta_{23}$ (right). The ν_μ parameters (red lines) and $\overline{\nu}_\mu$ parameters (blue lines) are treated independently. The right plot shows that the antineutrino mode of current T2K data alone can not resolve the θ_{23} octant degeneracy. Fig. 3.11 represents 3σ region of $\Delta\chi^2$ values of Δm^2_{31} versus $\Delta \overline{m}^2_{31}$ (left) and $\sin^2\theta_{23}$ versus $\sin^2\overline{\theta}_{23}$ (right). The red points represent T2K best fits, which are listed in Table 3.10. The statistical significance to exclude CPT conservation hypothesis is shown in Fig. 3.12 in terms of σ values versus $\delta_{\nu\overline{\nu}}(\Delta m^2_{31})$ (left) and $\delta_{\nu\overline{\nu}}(\sin^2\theta_{23})$ (right). The results show no CPT violation signature with current T2K data. The expression (3.85) summarizes the CPT violation bounds at 3σ C. L. with $|\delta_{\nu\overline{\nu}}(\Delta m^2_{31})|$ and $|\delta_{\nu\overline{\nu}}(\sin^2\theta_{23})|$

$$\begin{aligned}
|\delta_{\nu\overline{\nu}}(\Delta m^2_{31})| &< 6.35 \times 10^{-4} eV^2, \\
|\delta_{\nu\overline{\nu}}(\sin^2\theta_{23})| &< 0.19.
\end{aligned} \tag{3.85}$$

3.4.4 Sensitivity to CPT violation with a joint fit of T2K-II, NOvA-II, and JUNO

Bounds on CPT violation

In this study, assuming that CPT is exactly conserved, we estimate the expected bound of the two sensitive parameters, asymmetry in the mass-squared differences $\delta_{\nu\overline{\nu}}(\Delta m^2_{31})$ and asymmetry in the leptonic mixing angles $\delta_{\nu\overline{\nu}}(\sin^2\theta_{23})$, on the possible CPT violation. In particular, $\Delta m^2_{31} = \Delta \overline{m}^2_{31} = 2.55 \times 10^{-3}$ eV^2 and $\sin^2\theta_{23} = \sin^2\overline{\theta}_{23} = 0.51$, which are the T2K's best-fit points with recent measurement [1], are assumed to be *true*. To compute the allowed region of the $\delta_{\nu\overline{\nu}}(\Delta m^2_{31})$ and $\delta_{\nu\overline{\nu}}(\sin^2\theta_{23})$ parameters, we build up the χ^2 profiles on a two-dimensional grid points of neutrino and anti-neutrino corresponding parameters $(\Delta m^2_{31},\ \Delta \overline{m}^2_{31})$ and $(\sin^2\theta_{23},\ \sin^2\overline{\theta}_{23})$, respectively. The χ^2 profiles take into account the correlations among the oscillation
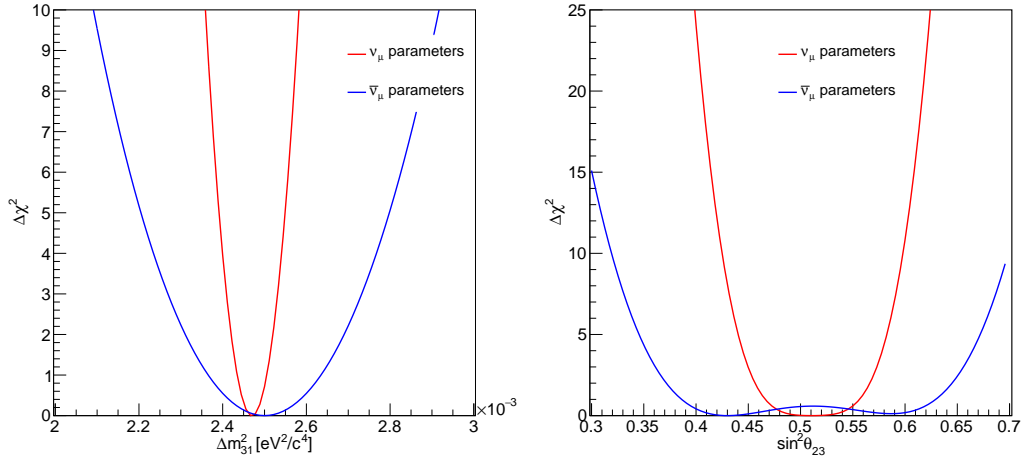
Figure 3.10: The distributions of $\Delta\chi^2$ as a function of Δm_{31}^2 (left) and $\sin^2\theta_{23}$ (right). The $\Delta\chi^2$ functions are treated independently for ν_μ parameters (red lines) and $\overline{\nu}_\mu$ parameters (blue lines). The simulation is done for T2K with 3.13×10^{21} POT exposure.
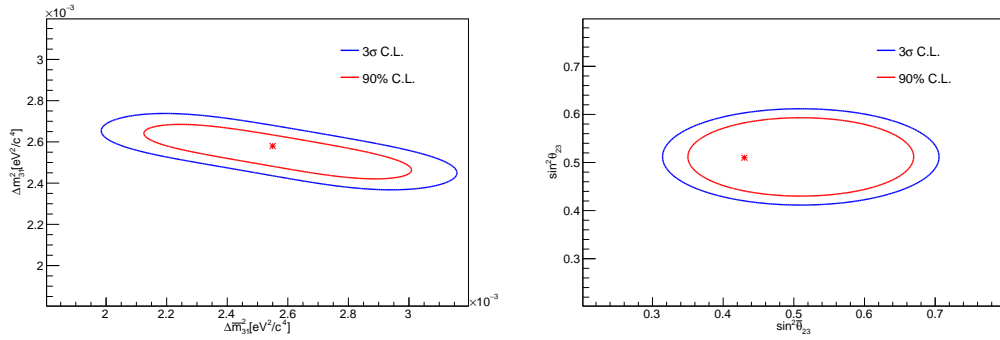
Figure 3.11: 3σ regions of Δm_{31}^2 and $\Delta\overline{m}_{31}^2$ (left), $\sin^2\theta_{23}$ and $\sin^2\overline{\theta}_{23}$ (right). The red points represent T2K best fits. The simulation is done for T2K with 3.13×10^{21} POT exposure.
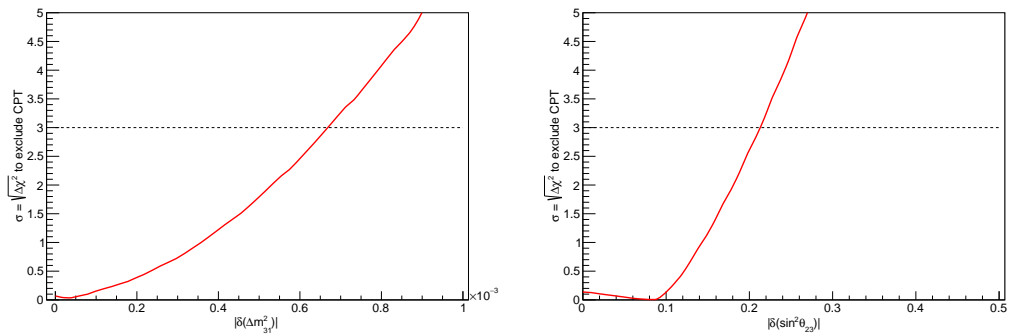
Figure 3.12: Statistical significance to exclude CPT conservation hypothesis with $\delta(\Delta m_{31}^2)$ (left) and $\delta(\sin^2\theta_{23})$ (right) for T2K with 3.13×10^{21} POT exposure.
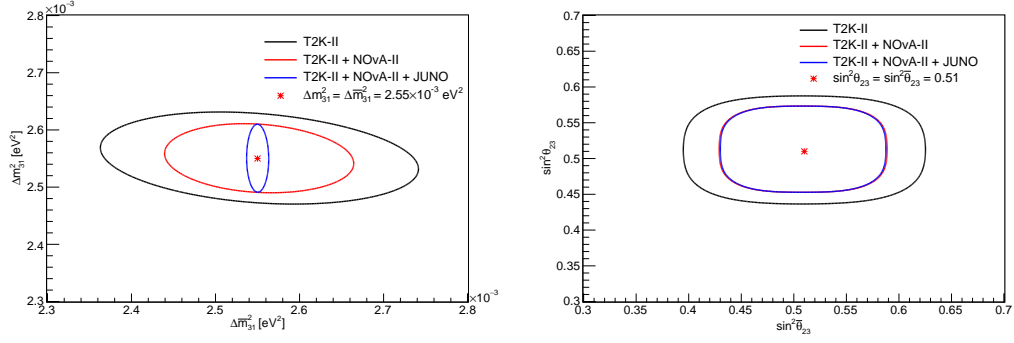
Figure 3.13: The 3σ C. L. regions of Δm_{31}^2 and $\Delta \overline{m}_{31}^2$ (left), $\sin^2 \theta_{23}$ and $\sin^2 \overline{\theta}_{23}$ (right). The back, red and blue lines are for an analysis with T2K-II only, a joint of T2K-II and NOνA-II, and a joint of T2K-II, NOνA-II, and JUNO, respectively.
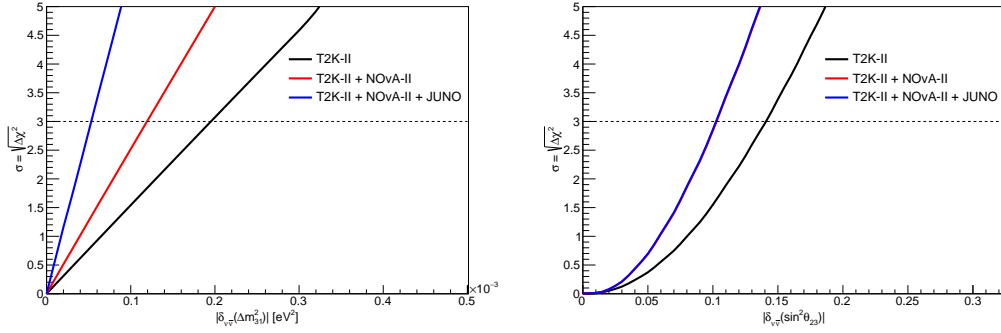
Figure 3.14: The bounds on possible CPT violation manifested in the asymmetries of the mass-squared splittings $|\delta_{\nu\overline{\nu}}(\Delta m_{31}^2)|$ (left) and of the leptonic mixing angles $|\delta_{\nu\overline{\nu}}(\sin^2 \theta_{23})|$ (right). The black, red, and blue lines correspond to an analysis with T2K-II only, a joint of T2K-II and NOνA-II, and a joint of T2K-II, NOνA-II, and JUNO, respectively.
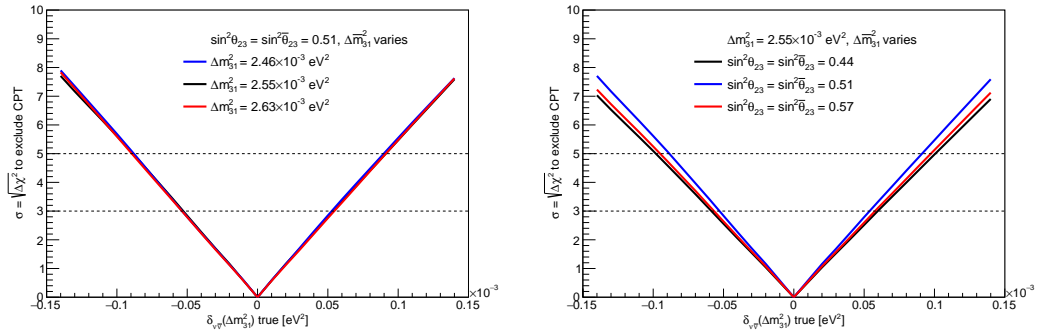
Figure 3.15: Statistical significance to exclude CPT is computed as a function of *true* $\delta_{\nu\overline{\nu}}(\Delta m_{31}^2)$ under various scenarios of the involved parameters. The left plot is when Δm_{31}^2 is examined at three different *true* values, while $\sin^2 \theta_{23} = \sin^2 \overline{\theta}_{23} = 0.51$ is assumed to be *true*. The right plot presents the CPT sensitivity of $\delta_{\nu\overline{\nu}}(\Delta m_{31}^2)$ at different *true* values of $\sin^2 \theta_{23}$ and $\sin^2 \overline{\theta}_{23}$ while $\Delta m_{31}^2 = 2.55 \times 10^{-3} \text{eV}^2$ is assumed to be *true*.

Experiments	3σ C. L. upper limits	
	$\|\delta_{\nu\overline{\nu}}(\Delta m_{31}^2)\|$	$\|\delta_{\nu\overline{\nu}}(\sin^2\theta_{23})\|$
T2K-II	2.0×10^{-4} eV^2	0.14
T2K-II+NOνA-II	1.2×10^{-4} eV^2	0.10
T2K-II+NOνA-II+JUNO	5.3×10^{-5} eV^2	0.10

Table 3.11:   The bounds on CPT violation with atmospheric mass-squared difference and mixing angle at 3σ C. L. for three analyses: T2K-II only, a joint of T2K-II and NOνA-II, a joint of T2K-II, NOνA-II, and JUNO.

parameters. The $\Delta\chi^2$ profiles are attained by subtracting to the minimum value of the according χ^2, which is essentially located at the *true* values.

Fig. 3.13 shows 3σ C. L. allowed regions of pairs of parameters (Δm_{31}^2, $\Delta\overline{m}_{31}^2$) and ($\sin^2\theta_{23}$, $\sin^2\overline{\theta}_{23}$) under the assumption that CPT is conserved. Three different analyses are presented: (i) T2K-II only, (ii) a joint of T2K-II and NOνA-II, and (iii) a joint of T2K-II, NOνA-II, and JUNO. It is expected that a joint analysis of T2K-II and NOνA-II improves significantly the precision of four involved (Δm_{31}^2, $\Delta\overline{m}_{31}^2$, $\sin^2\theta_{23}$, $\sin^2\overline{\theta}_{23}$) parameters while JUNO mainly contribute to the precision of $\Delta\overline{m}_{31}^2$.

To answer for the question about the allowed parameter magnitudes in the mass-squared difference $\delta_{\nu\overline{\nu}}(\Delta m_{31}^2)$ and the leptonic mixing angle $\delta_{\nu\overline{\nu}}(\sin^2\theta_{23})$, projections of $\Delta\chi^2$ profiles on these two variables are constructed and depicted in Fig. 3.14. The upper limits of these two CPT-sensitive variables at 3σ C. L. are extracted and summarized in Table 3.11. With total exposure of 10×10^{20} POT, T2K-II alone can set more stringent limits on the CPT violation search, if it will be not found, both with atmospheric mass-squared splitting $\|\delta_{\nu\overline{\nu}}(\Delta m_{31}^2)\| \leq 2.0 \times 10^{-4}$ eV^2 and leptonic mixing angles $\delta_{\nu\overline{\nu}}(\sin^2\theta_{23}) \leq 0.14$, than the combined data of current neutrino experiments. By adding NOνA-II, the 3σ C. L. limit on $\|\delta_{\nu\overline{\nu}}(\sin^2\theta_{23})\|$ for CPT violation is reduced to 0.10, a 47% improvement over the current limit. Meanwhile, if no evidence of CPT violation is found, the potential bound on $\|\delta_{\nu\overline{\nu}}(\Delta m_{31}^2)\|$ at 3σ C. L. will be expected to be 5.3×10^{-5} eV^2 for the combined analysis of the three experiments. This prospective bound on the possible CPT violation search is slightly better than the DUNE sensitivity [101], $\|\delta_{\nu\overline{\nu}}(\Delta m_{31}^2)\| < 8.1 \times 10^{-5}$ eV^2 at 3σ C. L.

Sensitivities to CPT violation

Apparently if the analyses with real data shows the asymmetries of $\|\delta_{\nu\overline{\nu}}(\Delta m_{31}^2)\|$ or $\|\delta_{\nu\overline{\nu}}(\sin^2\theta_{23})\|$ larger than the corresponding upper limits presented in Table 3.11, it would imply the CPT violation in the lepton sector. However, one raised question is whether these anticipated limits are affected by the *true* values of the underlying parameters, which can fluctuate from the current best-fit values. To investigate this issue, we performed the full joint analysis of T2K-II, NOνA-II, and JUNO under various assumptions of the involved parameters. In particular, for the potential effect on $\delta_{\nu\overline{\nu}}(\Delta m_{31}^2)$, we

Δm^2_{31} [eV^2]	Shared values of $\sin^2 \theta_{23}$, $\sin^2 \overline{\theta}_{23}$		
	0.44	0.51	0.57
2.46×10^{-3}	5.96×10^{-5}	5.36×10^{-5}	5.80×10^{-5}
2.55×10^{-3}	5.95×10^{-5}	5.39×10^{-5}	5.77×10^{-5}
2.63×10^{-3}	5.99×10^{-5}	5.46×10^{-5}	5.79×10^{-5}
	$\delta_{\nu\overline{\nu}}(\Delta m^2_{31})$ limit to exclude CPT at 3 σ C. L.		

Table 3.12: Lower limits for the *true* $|\delta_{\nu\overline{\nu}}(\Delta m^2_{31})|$ amplitude to exclude CPT at 3σ C. L. are computed at different *true* values of the involved parameters.

examine the CPT sensitivity at three points $(2.46 \times 10^{-3},\ 2.55 \times 10^{-3},\ 2.63 \times 10^{-3} \text{eV}^2)$ of Δm^2_{31}, taken as the T2K best-fit and $\pm 1\sigma$ shifted values, in combination with a variation of $\Delta \overline{m}^2_{31}$ such that $|\delta_{\nu\overline{\nu}}(\Delta m^2_{31})| < 0.15 \times 10^{-3} \text{eV}^2$. In this case of study, $\sin^2 \theta_{23} = \sin^2 \overline{\theta}_{23} = 0.51$ is assumed to be *true*. In addition, we check the sensitivities of CPT violation on the $\delta_{\nu\overline{\nu}}(\Delta m^2_{31})$ parameter at three shared values (0.44, 0.51, 0.57) of $(\sin^2 \theta_{23},\ \sin^2 \overline{\theta}_{23})$. For each case, the statistical significance to exclude the corresponding form of the CPT invariance is extracted as function of $\delta_{\nu\overline{\nu}}(\Delta m^2_{31})$ and the results are shown in Fig. 3.15. It is observed that the CPT violation sensitivity manifested on the $\delta_{\nu\overline{\nu}}(\Delta m^2_{31})$ parameter depends marginally on the central value of Δm^2_{31} and $\Delta \overline{m}^2_{31}$ in the current allowed range of this parameter. Also the dependence of the $\delta_{\nu\overline{\nu}}(\Delta m^2_{31})$ sensitivity on the *true* values of the mixing parameters $(\sin^2 \theta_{23},\ \sin^2 \overline{\theta}_{23})$ is relatively small. Apparently, due to the octant degeneracy of $(\sin^2 \theta_{23},\ \sin^2 \overline{\theta}_{23})$ presented in the *disappearance* probabilities of muon (anti-)neutrinos, the significance of the CPT test is slightly worse than the case where $(\sin^2 \theta_{23},\ \sin^2 \overline{\theta}_{23})$ is exactly equal or near the maximal mixing. The lower limit of *true* $\delta_{\nu\overline{\nu}}(\Delta m^2_{31})$ amplitude to exclude the CPT at 3σ C. L. or higher significance is presented in Table 3.12.

We find that if the amplitude of $\delta_{\nu\overline{\nu}}(\Delta m^2_{31})$ is greater than $6.0 \times 10^{-5} \text{eV}^2$ the CPT invariance will be excluded at 3σ C. L. for almost the entire currently-allowed range of the involved parameters. The range of possible $\delta_{\nu\overline{\nu}}(\Delta m^2_{31})$ asymmetry to be explored significantly is slightly extended $([5.36, 5.46] \times 10^{-5} \text{eV}^2)$ if the mixing angle is near the maximal mixing. Due to the aforementioned octant degeneracy of the (anti-)neutrino oscillation probabilities in the *disappearance* samples, the amplitude of $\delta_{\nu\overline{\nu}}(\Delta m^2_{31})$ must be moderately greater $([5.77, 5.99] \times 10^{-5} \text{eV}^2)$ for attaining a same level of significance to exclude the CPT invariance. To see how impressive the improvement in the CPT test sensitivity from this three-experiment combined analysis is, we project the statistical significance from the current measurements. Table 3.13 summarize the measurements of the $(\Delta m^2_{31},\ \Delta \overline{m}^2_{31},\ \theta_{23},\ \overline{\theta}_{23})$ parameters with the first generation of the A-LBL experiment MINOS [3, 4], on-going second generation T2K [1], NOνA [5], and precise constraint of the $\Delta \overline{m}^2_{31}$ parameter from the R-SBL experiment Daya Bay [6]. From the Table 3.13, we see that the difference in mass-squared splitting at the best-fit values of $(\Delta m^2_{31},\ \Delta \overline{m}^2_{31})$ measured by T2K [1]

	MINOS(+)	T2K	NOνA	Daya Bay
$\Delta m^2_{31}/10^{-3}\mathrm{eV}^2$	$2.48^{+0.08}_{-0.09}$	$2.55^{+0.08}_{-0.09}$	$2.56^{+0.07}_{-0.09}$	-
$\Delta \overline{m}^2_{31}/10^{-3}\mathrm{eV}^2$	$2.55^{+0.23}_{-0.25}$	$2.58^{+0.18}_{-0.13}$	$2.63^{+0.12}_{-0.13}$	$2.53^{+0.06}_{-0.06}$
$\sin^2\theta_{23}$	$0.43^{+0.20}_{-0.04}$	$0.51^{+0.06}_{-0.07}$	$0.51^{+0.06}_{-0.06}$	-
$\sin^2\overline{\theta}_{23}$	$0.41^{+0.05}_{-0.08}$	$0.43^{+0.21}_{-0.05}$	$0.41^{+0.04}_{-0.03}$	-

Table 3.13: Measurements of the (Δm^2_{31}, $\Delta\overline{m}^2_{31}$, θ_{23}, $\overline{\theta}_{23}$) parameters, which govern the muon neutrino and muon antineutrino disappearances, from different experiments: MINOS(+) [3,4], T2K [1], NOνA [5], Daya Bay [6]. Normal neutrino mass hierarchy is assumed.

is $|\delta_{\nu\overline{\nu}}(\Delta m^2_{31})| = 3 \times 10^{-5}\mathrm{eV}^2$, well consistent within 1σ uncertainty of $20 \times 10^{-5}\mathrm{eV}^2$. However, if this asymmetry persists as the *true*, it will correspond to 1.7σ C. L. exclusion of CPT conservation by the combined analysis of T2K-II, NOνA-II, and JUNO. If the level of asymmetrical $\delta_{\nu\overline{\nu}}(\Delta m^2_{31})$ in the neutrino and anti-neutrino best-fit values of NOνA and MINOS(+), which is 7.0×10^{-5} eV^2, are assumed to be persisted as the *true*, the synergy of the three experiments can exclude CPT conservation at 4σ C. L.

Regarding the sensitivity of $\delta_{\nu\overline{\nu}}(\sin^2\theta_{23})$ on the CPT test, we examine and find that their dependence on the fluctuation of the (Δm^2_{31}, $\Delta\overline{m}^2_{31}$) parameters is relatively small while the dependence on the *true* value of ($\sin^2\theta_{23}$, $\sin^2\overline{\theta}_{23}$) is significant, as shown in Fig. 3.16. When the *true* value of $\sin^2\theta_{23}$ belongs to an octant, there exists a degenerated solution in the other octant. For example, when $\sin^2\theta_{23}$=0.44, the *extrinsic* CPT-invariant solution of $\sin^2\overline{\theta}_{23}$=0.58 (along with the *genuine* solution of $\sin^2\overline{\theta}_{23}$=0.44). Similar behavior is observed when $\sin^2\theta_{23}$ values in the higher octant. The behavior is well-understood due to the dependence of muon (anti-) neutrino *disappearance* probabilities on the $\sin^2 2\theta_{23}$ ($\sin^2 2\overline{\theta}_{23}$) rather than $\sin^2\theta_{23}$ ($\sin^2\overline{\theta}_{23}$). As summarized in Table 3.14, to attain the same significance level to exclude the CPT, compared to the maximal case $\sin^2\theta_{23}$=0.51, the amplitude of *true* $\delta_{\nu\overline{\nu}}(\sin^2\theta_{23})$ asymmetry in the non-maximal cases ($\sin^2\theta_{23}$=0.44 and $\sin^2\theta_{23}$=0.57) is required to be larger or smaller depending on whether the θ_{23} and $\overline{\theta}_{23}$ belong to the different or same octants, respectively. In particular, for $\sin^2\theta_{23}$=0.51 as indicated by both T2K [1] and NOνA [5], the amplitude of $\delta_{\nu\overline{\nu}}(\sin^2\theta_{23})$ asymmetry must be between [0.076, 0.084] to be discovered with 3σ C. L. T2K (NOνA) measured $\delta_{\nu\overline{\nu}}(\sin^2\theta_{23})$=0.08 (0.10) respectively, and if it remains as *true* the CPT invariance will be excluded at 3σ or higher C. L. If θ_{23} and $\overline{\theta}_{23}$ are in the same octant and relatively far off from the maximal values, the amplitude of $\delta_{\nu\overline{\nu}}(\sin^2\theta_{23})$ must be greater than 0.051 in order to rule out CPT invariance at 3σ C. L.. If θ_{23} and $\overline{\theta}_{23}$ are in different octants, θ_{23} in lower octant and $\overline{\theta}_{23}$ in higher octant or vice versa, the amplitude of $\delta_{\nu\overline{\nu}}(\sin^2\theta_{23})$ must be significantly higher, varying in the (0.165,0.190) range, to exclude CPT at the same 3σ statistical significance. The sensitivity to detect CPT violation via the $\delta_{\nu\overline{\nu}}(\sin^2\theta_{23})$ asymmetry is not good due to the aforementioned octant degeneracy in the muon (anti-) neutrino *disappearance* samples. The sensitivity can be improved by adding the electron
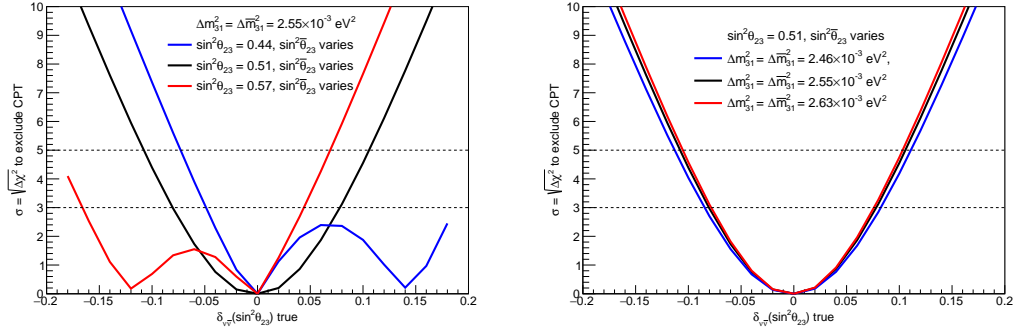
Figure 3.16: Statistical significance to exclude CPT is computed as function of *true* $\delta_{\nu\overline{\nu}}(\sin^2\theta_{23})$ under various scenarios of the involved parameters. The left is when $\sin^2\theta_{23}$ is examined at three different *true* values while $\Delta m_{31}^2 = \Delta\overline{m}_{31}^2 = 2.55 \times 10^{-3}\text{eV}^2$ is assumed. The right presents the CPT sensitivity of $\delta_{\nu\overline{\nu}}(\sin^2\theta_{23})$ at different *true* values of Δm_{31}^2 and $\Delta\overline{m}_{31}^2$ while $\sin^2\theta_{23} = 0.51$ is assumed to be *true*.
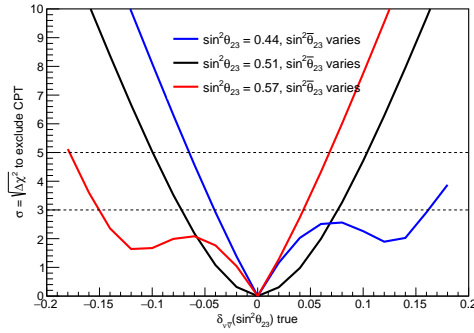
Figure 3.17: Statistical significance to exclude CPT is computed as a function of *true* $\delta_{\nu\overline{\nu}}(\sin^2\theta_{23})$ under various scenarios of the involved parameters. Both muon (anti-)neutrino *disappearance* samples and electron (anti-)neutrino *appearance* samples from T2K-II and NOνA-II are used. The sensitivity is examined at three different *true* values of $\sin^2\theta_{23}$ values while $\Delta m_{31}^2 = \Delta\overline{m}_{31}^2 = 2.55 \times 10^{-3}\text{eV}^2$ is assumed to be *true*.

$\sin^2\theta_{23}$	Shared values of Δm_{31}^2, $\Delta\overline{m}_{31}^2$ [eV^2]		
	2.46×10^{-3}	2.55×10^{-3}	2.63×10^{-3}
0.44	-0.051 (+0.190)	-0.049 (+0.187)	-0.048 (+0.186)
0.51	-0.084 (+0.082)	-0.080 (+0.078)	-0.078 (+0.076)
0.57	-0.169 (+0.047)	-0.166 (+0.044)	-0.165 (+0.043)
	$\delta_{\nu\overline{\nu}}(\sin^2\theta_{23})$ limit to exclude CPT at 3 σ C. L.		

Table 3.14: Lower limits for the *true* $|\delta_{\nu\overline{\nu}}(\sin^2\theta_{23})|$ amplitude to exclude CPT at 3σ C. L. are computed at different *true* values of involved parameters. The -(+) signs in each cell correspond to the negative (positive) value of $\delta_{\nu\overline{\nu}}(\sin^2\theta_{23})$.

(anti-)neutrino *appearance* samples from the A-LBL experiments. Fig. 3.17 shows the sensitivity of $\delta_{\nu\overline{\nu}}(\sin^2\theta_{23})$ on the CPT exclusion with a combination of both *disappearance* and *appearance* samples. It is observed that by adding the electron (anti-)neutrino *appearance* samples, the statistical significance to exclude the *extrinsic* CPT-invariant solution is enhanced notably. Consequently, the sensitivity of $\delta_{\nu\overline{\nu}}(\sin^2\theta_{23})$ to the CPT violation has improved. However, one must consider carefully when adding the electron (anti-)neutrino *appearance* samples. The reason is that the probabilities of $\nu_e(\overline{\nu}_e)$ from $\nu_\mu(\overline{\nu}_\mu)$ depend not only on $\theta_{23}(\overline{\theta}_{23})$ but also on two known unknowns, CP-violating phase and mass hierarchy, which will complicate the interpretation of the experimental observation.

Conclusions

In the thesis, we have presented the simulations and measurements in the T2K experiment that we have directly contributed. The results come into two main parts, neutrino beam profile study at INGRID, and testing CP and CPT invariances with T2K and with the combined analysis of T2K-II, NOvA-II, and JUNO.

We presented our MC study and the measurements at the INGRID detector for different horn configurations in the Chapter 2. Our study shows that the event rates, neutrino beam directions, and beam widths are stable and in good agreement between the MC study and the data of T2K run 10. We also showed the MC study at INGRID with a 320 kA horn configuration, which can be tested with future data of T2K.

In the Appendix A, we showed some preliminary results of the neutrino cross section measurements at WAGASCI BabyMIND experiment which we have currently involved in the analysis.

In Chapter 3, the CP and CPT violation searches with the T2K experiment are presented. The current data of T2K rules out CP conserving hypothesis at more than 95%. With T2K data only, the CP violating phase δ_{CP} is measured to be $-2.14^{+0.90}_{-0.69}$ in case of normal mass ordering and $-1.26^{+0.61}_{-0.69}$ in case of inverted mass ordering. When T2K is combined with short baseline reactor experiments, the best fits and best fits $\pm 1\sigma$ values of δ_{CP} are $-1.89^{+0.70}_{-0.58}$ for normal ordering and $-1.38^{+0.48}_{-0.55}$ for inverted ordering. We also show that if T2K-II data is combined with NOvA-II and JUNO experiments, we will be able to discover CP violation at around 5σ C. L. by 2028.

The study shows there is no signature of CPT violation with current data of T2K. The synergy of T2K-II, NOvA-II, and JUNO will improve the sensitivity and bounds on CPT violation to unprecedented levels of precision. If the recent T2K (NOvA) results on mass squared splittings (Δm^2_{31}, $\Delta \overline{m}^2_{31}$) and mixing angles ($\theta_{23}$, $\overline{\theta}_{23}$) are presumed to be true values, the combined data of the three experiments is able to exclude CPT symmetry at 1.7σ (4σ) and 3σ (4σ) C. L., respectively. By 2028, before the next generation neutrino experiments DUNE and Hyper-K begin their operations, the synergy of T2K-II, NOvA-II and JUNO can improve the bound on $|\delta(\Delta m^2_{31})|$ to the world's best value, $5.3 \times 10^{-5} eV^2$ at 3σ C. L. The sensitivity to CPT violation basically does not depend on the true values of Δm^2_{31} and $\Delta \overline{m}^2_{31}$, and the θ_{23} octant degeneracy. The mixing angle CPT violation sensitivity, otherwise significantly depends on the true values of θ_{23} and $\overline{\theta}_{23}$ as well as their differences.

Next step, we will try to make a real data fit with T2K, NOvA, and MINOS. Also, a preliminary study of the Hyper-K sensitivity shows that it will provide the best constraint on CPT violation ever. We will make more investigation on this exciting study.

List of Publications

List of publications used for thesis defense

1. T. V. Ngoc, S. Cao, N. T. Hong Van, and P. T. Quyen. *Stringent constraint on CPT violation with a combined analysis of T2K-II, NOνA extension, and JUNO.* Phys. Rev. D, 107 016013, 2023.

2. S. Cao, A. Nath, T. V. Ngoc, Ng. K. Francis, N. T. Hong Van, and P. T. Quyen. *Physics potential of the combined sensitivity of T2K-II, NOνA extension, and JUNO.* Phys. Rev. D, 103 11 112010, 2021.

List of other publications

1. S. Cao, N. T. Hong Van, T. V. Ngoc, and P. T. Quyen. *Neutrino Mass Spectrum: Present Indication and Future Prospect.* Symmetry, 14 1, 2022.

2. T. V. Ngoc, S. Cao, N. T. Hong Van. *Combined Sensitivity of T2K-II and NOνA Experiments to CP Violation in Lepton Sector.* Commun. in Phys., 28 4, 337, 2018.

3. S. Cao, T. V. Ngoc, N. T. Hong Van, and P. T. Quyen. *Practical use of reactor anti-neutrinos for nuclear safeguard in Vietnam.* Accepted to publish on Commun. in Phys., [arXiv:2209.03541].

4. N. H. Duy Thanh, N. V. Chi Lan, S. Cao, T. V. Ngoc, N. Khoa, N. T. H. Van, and P. T. Quyen. *Multi-pixel photon counter for operating a tabletop cosmic ray detector under loosely controlled conditions.* Dalat University Journal of Science, 13 1, 16-29, 2022.

5. T. V. Ngoc *et. al.* [T2K collaboration]. *T2K measurements of muon neutrino and antineutrino disappearance using 3.13×10^{21} protons on target.* Phys. Rev. D, 103 1, L011101, 2021.

6. T. V. Ngoc *et. al.* [T2K collaboration]. *Improved constraints on neutrino mixing from the T2K experiment with 3.13×10^{21} protons on target.* Phys. Rev. D, 103 11, 112008, 2021.

7. T. V. Ngoc *et. al.* [T2K collaboration]. *Constraint on the matter–antimatter symmetry-violating phase in neutrino oscillations.* Nature, 580 7803, 339-344, 2020. Nature, 583 7814, E16, 2020 (erratum).

Bibliography

[1] K. Abe et al. *T2K measurements of muon neutrino and antineutrino disappearance using 3.13×10^{21} protons on target. Phys. Rev. D*, 103:L011101, Jan 2021.

[2] Ivan Esteban, M.C. Gonzalez-Garcia, Alvaro Hernandez-Cabezudo, Michele Maltoni, and Thomas Schwetz. *Global analysis of three-flavour neutrino oscillations: synergies and tensions in the determination of θ_{23}, δ_{CP}, and the mass ordering. J. High Energy Phys.*, 01:106, 2019.

[3] P. Adamson et al. *Measurement of Neutrino and Antineutrino Oscillations Using Beam and Atmospheric Data in MINOS. Phys. Rev. Lett.*, 110(25), Jun 2013.

[4] P. Adamson et al. *Precision Constraints for Three-Flavor Neutrino Oscillations from the Full MINOS+ and MINOS Dataset. Phys. Rev. Lett.*, 125:131802, Sept 2020.

[5] Patricia Diana Mendez Mendez. *Comparison of oscillation parameters measured from ν_μ and $\bar{\nu}_\mu$ disappearance in the NOvA experiment.* PhD thesis, University of Sussex, Oct 2019.

[6] Kam-Biu Luk. *Reactor Neutrino: Latest Results from Daya Bay.* Jun 2022.

[7] Son Cao, Nguyen T. Hong Van, Tran V. Ngoc, and Phan T. Quyen. *Neutrino Mass Spectrum: Present Indication and Future Prospect. Symmetry*, 14(56), Jan 2022.

[8] Tatsuya Kikawa. *Measurement of Neutrino Interactions and Three Flavor Neutrino Oscillations in the T2K Experiment.* PhD thesis, Kyoto U. (main), Sept 2014.

[9] S. Pascoli, S. T. Petcov, and Antonio Riotto. *Connecting low energy leptonic CP-violation to leptogenesis. Phys. Rev. D*, 75(8), Apr 2007.

[10] K. Abe et al. *Measurement of neutrino and antineutrino oscillations by the T2K experiment including a new additional sample of ν_e interactions at the far detector. Phys. Rev. D*, 96(9):092006, 2017. [Erratum: *Phys. Rev. D*, 98 019902, 2018].

[11] Zelimir Djurcic et al. *JUNO Conceptual Design Report.* Aug 2015.

[12] R. L. Workman and Others. *Review of Particle Physics. PTEP*, 2022:083C01, 2022.

[13] T. D. Lee and C. N. Yang. *Question of Parity Conservation in Weak Interactions. Phys. Rev.*, 104:254–258, Oct 1956.

[14] C. S. Wu, E. Ambler, R. W. Hayward, D. D. Hoppes, and R. P. Hudson. *Experimental Test of Parity Conservation in Beta Decay*. Phys. Rev., 105:1413–1415, Feb 1957.

[15] J. H. Christenson, J. W. Cronin, V. L. Fitch, and R. Turlay. *Evidence for the 2π Decay of the K_2^0 Meson*. Phys. Rev. Lett., 13:138–140, Jul 1964.

[16] B. Aubert et al. *Measurement of CP-Violating Asymmetries in B^0 Decays to CP Eigenstates*. Phys. Rev. Lett., 86:2515–2522, Mar 2001.

[17] K. Abe et al. *Observation of Large CP Violation in the Neutral B Meson System*. Phys. Rev. Lett., 87:091802, Aug 2001.

[18] K. Abe et al. *Constraint on the matter–antimatter symmetry-violating phase in neutrino oscillations*. Nature, 580:339–344, Apr 2020.

[19] O. Bertolami, Don Colladay, V.Alan Kostelecký, and R. Potting. *CPT violation and baryogenesis*. Phys. Lett. B, 395(3-4):178–183, Mar 1997.

[20] Don Colladay and V. Alan Kostelecký . ”*CPT violation and the Standard Model*. Phys. Rev. D, 55(11):6760–6774, Jun 1997.

[21] D. Colladay and V. Alan Kostelecky. *Lorentz-violating extension of the standard model*. Phys. Rev. D, 58:116002, Oct 1998.

[22] V. Alan Kostelecky. *Gravity, Lorentz violation, and the standard model*. Phys. Rev. D, 69(10), May 2004.

[23] V. Alan Kostelecký and Neil Russell. *Data tables for Lorentz and CPT violation*. Reviews of Modern Physics, 83(1):11–31, Mar 2011.

[24] C. Q. Geng and Lei Geng. *Some test on CPT invariance*. Modern Physics Letters A, 22(07n10):651–659, Mar 2007.

[25] C. A. Argüelles et al. *Snowmass White Paper: Beyond the Standard Model effects on Neutrino Flavor*, 2022.

[26] V. Barger, S. Pakvasa, T. J. Weiler, and K. Whisnant. *CPT-Odd Resonances in Neutrino Oscillations*. Phys. Rev. Lett., 85(24):5055–5058, Dec 2000.

[27] Hitoshi Murayama. *CPT tests: kaon vs. neutrinos*. Phys. Lett. B, 597(1):73–77, Sept 2004.

[28] B. Pontecorvo. *Mesonium and anti-mesonium*. Sov. Phys. JETP, 6:429, 1957. [Zh. Eksp. Teor. Fiz.33,549(1957)].

[29] Ziro Maki, Masami Nakagawa, and Shoichi Sakata. *Remarks on the unified model of elementary particles*. Prog. Theor. Phys., 28:870–880, 1962. [,34(1962)].

[30] Raymond Davis, Jr., Don S. Harmer, and Kenneth C. Hoffman. *Search for neutrinos from the sun*. Phys. Rev. Lett., 20:1205–1209, 1968.

[31] B. T. Cleveland, Timothy Daily, Raymond Davis, Jr., James R. Distel, Kenneth Lande, C. K. Lee, Paul S. Wildenhain, and Jack Ullman. *Measurement of the solar electron neutrino flux with the Homestake chlorine detector*. Astrophys. J., 496:505–526, 1998.

[32] K. S. Hirata et al. *Experimental Study of the Atmospheric Neutrino Flux*. Phys. Lett., B205:416, 1988. [,447(1988)].

[33] Y. Fukuda et al. *Evidence for oscillation of atmospheric neutrinos*. Phys. Rev. Lett., 81:1562–1567, 1998.

[34] Q. R. Ahmad et al. *Measurement of the rate of $\nu_e + d \rightarrow p + p + e^-$ interactions produced by ^8B solar neutrinos at the Sudbury Neutrino Observatory*. Phys. Rev. Lett., 87:071301, 2001.

[35] C. L. Cowan, F. Reines, F. B. Harrison, H. W. Kruse, and A. D. McGuire. *Detection of the Free Neutrino: a Confirmation*. Science, 124(3212):103–104, 1956.

[36] G. Danby, J-M. Gaillard, K. Goulianos, L. M. Lederman, N. Mistry, M. Schwartz, and J. Steinberger. *Observation of High-Energy Neutrino Reactions and the Existence of Two Kinds of Neutrinos*. Phys. Rev. Lett., 9:36–44, Jul 1962.

[37] K. Kodama et al. *Observation of tau neutrino interactions*. Phys. Lett. B, 504(3):218–224, 2001.

[38] Mark Thomson. *Modern particle physics*. Cambridge University Press, New York, 2013.

[39] Jiro Arafune, Masafumi Koike, and Joe Sato. *Erratum: CP violation and matter effect in long baseline neutrino oscillation experiments [Phys. Rev. D, 56 3093, 1997]*. Phys. Rev. D, 60:119905, Oct 1999.

[40] L. Wolfenstein. *Neutrino Oscillations in Matter*. Phys. Rev. D, 17:2369–2374, 1978.

[41] S.P. Mikheyev and A.Yu. Smirnov. *Resonance Amplification of Oscillations in Matter and Spectroscopy of Solar Neutrinos*. Sov. J. Nucl. Phys., 42:913–917, 1985.

[42] Carlo Giunti and Chung W. Kim. *Fundamentals of Neutrino Physics and Astrophysics*. 2007.

[43] Fumihiko Suekane. *Neutrino Oscillations: A Practical Guide to Basics and Applications*, volume 898. 2015.

[44] K. Abe et al. *Indication of Electron Neutrino Appearance from an Accelerator-Produced Off-Axis Muon Neutrino Beam. Phys. Rev. Lett.*, 107:041801, Jul 2011.

[45] K. Abe et al. *Evidence of electron neutrino appearance in a muon neutrino beam. Phys. Rev. D*, 88:032002, Aug 2013.

[46] K. Abe et al. *Sensitivity of the T2K accelerator-based neutrino experiment with an Extended run to* 20×10^{21} *POTs.* Jul 2016.

[47] K. Abe et al. *Hyper-Kamiokande Design Report.* May 2018.

[48] Patrick Dunne. *Latest Neutrino Oscillation Results from T2K*, Jul 2020.

[49] D.S. Ayres et al. *The NOvA Technical Design Report.* Oct 2007.

[50] L. Wolfenstein. *Neutrino Oscillations in Matter. Phys. Rev. D*, 17:2369–2374, 1978.

[51] Mario A Acero, P Adamson, et al. *First measurement of neutrino oscillation parameters using neutrinos and anti-neutrinos by NOνA. Phys. Rev. Lett.*, 123(15):151803, 2019.

[52] Alex Himmel. *New Oscillation Results from the NOνA Experiment*, Jul 2020.

[53] M. Sanchez. *NOνA results and prospects. XXVIII International Conference on Neutrino Physics and Astrophysics*, 2018.

[54] Liang Zhan, Yifang Wang, Jun Cao, and Liangjian Wen. *Determination of the Neutrino Mass Hierarchy at an Intermediate Baseline. Phys. Rev. D*, 78:111103, 2008.

[55] Angel Abusleme et al. *Calibration Strategy of the JUNO Experiment. J. High Energy Phys.*, 03:004, 2021.

[56] *T2K-TN-038.*

[57] Y. Hayato. *NEUT. Nucl. Phys. B Proc. Suppl.*, 112:171–176, 2002.

[58] Yoshinari Hayato. *A neutrino interaction simulation program library NEUT. Acta Phys. Polon. B*, 40:2477–2489, 2009.

[59] Yoshinari Hayato and Luke Pickering. *The NEUT neutrino interaction simulation program library. The European Physical Journal Special Topics*, 230(24):4469–4481, Oct 2021.

[60] René Brun, F. Bruyant, Federico Carminati, Simone Giani, M. Maire, A. McPherson, G. Patrick, and L. Urban. *GEANT Detector Description and Simulation Tool.* Oct 1994.

[61] Alfredo Ferrari, Paola R. Sala, Alberto Fasso, and Johannes Ranft. *FLUKA: A multi-particle transport code (Program version 2005).* Oct 2005.

[62] G. Battistoni, F. Cerutti, A. Fassò, A. Ferrari, S. Muraro, J. Ranft, S. Roesler, and P. R. Sala. *The FLUKA code: description and benchmarking. AIP Conference Proceedings*, 896(1):31–49, 2007.

[63] http://www.fluka.org/fluka.php?id=release. Accessible: 03-Jan-2023.

[64] N. Abgrall et al. *Report from the NA61/SHINE experiment at the CERN SPS*. Apr 2008.

[65] N. Abgrall et al. *Measurements of $\pi^\pm, K^\pm, K^0_S, \Lambda$ and proton production in proton-carbon interactions at 31 GeV/c with the NA61/SHINE spectrometer at the CERN SPS. The European Physical Journal C*, 76(2), Feb 2016.

[66] Antoni Marcinek. *Highlights from the NA61/SHINE experiment. Acta Phys. Polon. Supp.*, 16:1–A8, 2023.

[67] *T2K-TN-132*.

[68] *T2K-TN-283*.

[69] David Griffiths. *Introduction to elementary particles*. 2008.

[70] Ralf Lehnert. *CPT Symmetry and Its Violation. Symmetry*, 8(11), 2016.

[71] Julian S. Schwinger. *The Theory of quantized fields. 1. Phys. Rev.*, 82:914–927, 1951.

[72] Julian S. Schwinger. *Spin, statistics, and the TCP theorem. Proc. Nat. Acad. Sci.*, 44:223–228, 1958.

[73] Gerhart Luders. *On the Equivalence of Invariance under Time Reversal and under Particle-Antiparticle Conjugation for Relativistic Field Theories. Kong. Dan. Vid. Sel. Mat. Fys. Med.*, 28N5(5):1–17, 1954.

[74] W. Pauli, L. Rosenfeld, and V. Weisskopf. *Niels Bohr and the Development of Physics*. 1955.

[75] Andrew Whitaker. *John Stewart Bell and Twentieth-Century Physics*. 2016.

[76] R. Jost. *Eine Bemerkung zum CTP theorem. Helv. Phys. Acta*, 30(409), 1957.

[77] O.W. Greenberg. *Why is CPT fundamental? Found. Phys.*, 36:1535–1553, 2006.

[78] K. Abe et al. *Observation of Electron Neutrino Appearance in a Muon Neutrino Beam. Phys. Rev. Lett.*, 112:061802, 2014.

[79] K. Abe et al. *Improved constraints on neutrino mixing from the T2K experiment with 3.13×10^{21} protons on target. Phys. Rev. D*, 103:112008, Jun 2021.

[80] S. Cao, A. Nath, T. V. Ngoc, P. T. Quyen, N. T. Hong Van, and Ng. K. Francis. *Physics potential of the combined sensitivity of T2K-II, NOνA extension, and JUNO. Phys. Rev. D*, 103(11):112010, 2021.

[81] Ivan Esteban et al. *NuFIT 4.1 (2019), www.nu-fit.org.* `http://www.nu-fit.org/?q=node/211`, July 2019.

[82] V. Barger, D. Marfatia, and K. Whisnant. *Breaking eight fold degeneracies in neutrino CP violation, mixing, and mass hierarchy.* Phys. Rev. D, 65:073023, 2002.

[83] Xinheng Guo et al. *A Precision measurement of the neutrino mixing angle θ_{13} using reactor antineutrinos at Daya-Bay.* Jan 2007.

[84] F. Ardellier et al. *Double Chooz: A Search for the neutrino mixing angle theta(13).* June 2006.

[85] J.K. Ahn et al. *RENO: An Experiment for Neutrino Oscillation Parameter θ_{13} Using Reactor Neutrinos at Yonggwang.* Mar 2010.

[86] Patrick Huber, M. Lindner, and W. Winter. *Simulation of long-baseline neutrino oscillation experiments with GLoBES (General Long Baseline Experiment Simulator).* Comput. Phys. Commun., 167:195, 2005.

[87] Patrick Huber, Joachim Kopp, Manfred Lindner, Mark Rolinec, and Walter Winter. *New features in the simulation of neutrino oscillation experiments with GLoBES 3.0.* Comput. Phys. Commun., 177(5):432–438, 2007.

[88] Adam M Dziewonski and Don L Anderson. *Preliminary reference Earth model (PREM).* Phys. Earth Planet. Interiors, 25(4):297–356, 1981.

[89] K. Abe et al. *Measurements of neutrino oscillation in appearance and disappearance channels by the T2K experiment with 6.6×10^{20} protons on target.* Phys. Rev. D, 91(7):072010, 2015.

[90] Mark D. Messier. *Evidence for neutrino mass from observations of atmospheric neutrinos with Super-Kamiokande.* PhD thesis, Boston University, 1999. UMI-99-23965.

[91] E. A. Paschos and J. Y. Yu. *Neutrino interactions in oscillation experiments.* Phys. Rev. D, 65:033002, 2002.

[92] Leonidas Aliaga Soplin and Linda Cremonesi. *NOνA near detector fluxes.* `https://nova-docdb.fnal.gov/cgi-bin/ShowDocument?docid=25266`, Jul 2018.

[93] MA Acero, P Adamson, et al. *New constraints on oscillation parameters from ν_e appearance and ν_μ disappearance in the NOνA experiment.* Phys. Rev. D, 98(3):032012, 2018.

[94] Patrick Huber and Thomas Schwetz. *Precision spectroscopy with reactor antineutrinos.* Phys. Rev. D, 70(5):053011, 2004.

[95] Amir N Khan, Hiroshi Nunokawa, and Stephen J Parke. *Why matter effects matter for JUNO? Phys. Lett. B*, 803:135354, 2020.

[96] Jun Cao and Kam-Biu Luk. *An overview of the Daya Bay Reactor Neutrino Experiment. Nucl. Phys. B*, 908:62–73, 2016.

[97] P.A. Zyla et al. *Review of Particle Physics. PTEP*, 2020(8):083C01, 2020. And 2021 update.

[98] G. Barenboim, John F. Beacom, L. Borissov, and Boris Kayser. *CPT Violation and the Nature of Neutrinos. Phys. Lett. B*, 537:227–232, 2002.

[99] Bruno Pontecorvo. *Mesonium and antimesonium. JETP*, 6:429, 1958.

[100] Gabriela Barenboim, Christoph A. Ternes, and Mariam Tortola. *CPT and CP, an entangled couple. Journal of High Energy Physics*, 2020(7), Jul 2020.

[101] G. Barenboim, C.A. Ternes, and M. Tórtola. *Neutrinos, DUNE and the world best bound on CPT invariance. Phys. Lett. B*, 780:631 – 637, 2018.

[102] M.C. Bañuls, G. Barenboim, and J. Bernabéu. *Medium effects for terrestrial and atmospheric neutrino oscillations. Phys. Lett. B*, 513(3-4):391–400, Aug 2001.

[103] Zhi zhong Xing. *Fake CPT violation in disappearance neutrino oscillations. Journal of Physics G: Nuclear and Particle Physics*, 28(2):B7–B11, Jan 2002.

[104] J. Bernabéu, S. Palomares-Ruiz, A. Pérez, and S.T. Petcov. *The earth Mantle-Core effect in charge-asymmetries for atmospheric neutrino oscillations. Phys. Lett. B*, 531(1-2):90–98, Apr 2002.

[105] Magnus Jacobson and Tommy Ohlsson. *Extrinsic CPT violation in neutrino oscillations in matter. Phys. Rev. D*, 69(1), Jan 2004.

[106] Tommy Ohlsson and Shun Zhou. *Extrinsic and intrinsic CPT asymmetries in neutrino oscillations. Nuclear Physics B*, 893:482 – 500, 2015.

[107] V. Barger, K. Whisnant, S. Pakvasa, and R. J. N. Phillips. *Matter effects on three-neutrino oscillations. Phys. Rev. D*, 22:2718–2726, Dec 1980.

[108] JUNO Collaboration, Angel Abusleme, et al. *Sub-percent Precision Measurement of Neutrino Oscillation Parameters with JUNO*, 2022.

[109] Christophe Bronner. *Accelerator Neutrino I_Recent results from T2K*, Jun 2022.

[110] Abe, K. et. al. *Neutrino beam flux prediction 2020*, Nov 2021.

[111] K. Abe et al. *Updated T2K measurements of muon neutrino and antineutrino disappearance using 1.5×10^{21} protons on target. Phys. Rev. D*, 96:011102, Jul 2017.

[112] K. Abe et al. *Combined Analysis of Neutrino and Antineutrino Oscillations at T2K*. *Phys. Rev. Lett.*, 118:151801, Apr 2017.

[113] C.H. Llewellyn Smith. *Neutrino reactions at accelerator energies*. *Physics Reports*, 3(5):261 – 379, 1972.

[114] J. Nieves, I. Ruiz Simo, and M. J. Vicente Vacas. *Inclusive charged-current neutrino-nucleus reactions*. *Phys. Rev. C*, 83:045501, Apr 2011.

[115] Dieter Rein and Lalit M Sehgal. *Neutrino-excitation of baryon resonances and single pion production*. *Annals of Physics*, 133(1):79 – 153, 1981.

[116] R. P. Feynman, M. Kislinger, and F. Ravndal. *Current Matrix Elements from a Relativistic Quark Model*. *Phys. Rev. D*, 3:2706–2732, Jun 1971.

[117] Krzysztof M. Graczyk and Jan T. Sobczyk. *Lepton mass effects in weak charged current single pion production*. *Phys. Rev. D*, 77:053003, Mar 2008.

[118] Stephen L. Adler. *Tests of the Conserved Vector Current and Partially Conserved Axial-Vector Current Hypotheses in High-Energy Neutrino Reactions*. *Phys. Rev.*, 135:B963–B966, Aug 1964.

[119] Dieter Rein and Lalit M. Sehgal. *Coherent pion production in neutrino reactions*. *Nuclear Physics B*, 223(1):29 – 44, 1983.

[120] D. Rein and L.M. Sehgal. *PCAC and the deficit of forward muons in pion production by neutrinos*. *Phys. Lett. B*, 657(4):207 – 209, 2007.

[121] Ch. Berger and L. M. Sehgal. *Partially conserved axial vector current and coherent pion production by low energy neutrinos*. *Phys. Rev. D*, 79:053003, Mar 2009.

Appendix A. Neutrino cross section measurements at WAGASCI BabyMIND

In the T2K analysis, large sources of systematic uncertainty come from flux and cross section model, which are strongly constrained by the near detector measurements. The large cross section uncertainty is mainly caused by the difference in the target material between the near and far detectors, and by the limited acceptance of ND280 as well. The target material of the ND280 detector is mostly hydrocarbons (CH), while the Super-K detector is water (H_2O). In order to reduce this systematic error, the new water grid scintillator detector (WAGASCI) is constructed at the B2 floor of the J-PARC neutrino hall at 1.5° off-axis angle. The primary goals of WAGASCI-BabyMIND are

- to measure the charge current cross section ratio between water and scintillator targets with 3% accuracy.

- to measure different charged current neutrino interaction channels with high precision and large acceptance.

In this section, we will present the current status and recent measurements of neutrino cross sections on water and on hydrocarbons by using WAGASCI-BabyMIND detectors.

A.0.1 WAGASCI BabyMIND

The WAGASCI BabyMIND consists of several modules classified into the central detectors and muon range detector (MRD). Fig. A.1 left shows the configuration of the WAGASCI modules. Along the neutrino flux direction, the central part is three neutrino interaction targets including water-out WAGASCI, Proton Module, and water-in WAGASCI detectors. These detectors are surrounded by two Wall-MRDs and one downstream muon range detector called Baby MIND.

WAGASCI detectors

The WAGASCI central module includes two sub-detectors which are mainly made from plastic scintillators. The total of 1280 plastic scintillator bars are constructed in a hollow cuboid lattice structure which can have 4π angular acceptance for charged particles as illustrated in Fig. A.2. Scintillator bars are fixed in plane with 40 parallel bars which are perpendicular to the beam and another 40 lattice bars which are parallel to the beam. One WAGASCI detector consists of 16 scintillator tracking planes. The whole structure is protected by a stainless steel tank of size 460mm×1250mm×1250 mm, and weighs 0.5 tonne (Fig. A.3 left). Each plastic scintillator bar used in the WAGASCI experiment has a size of 1020mm×25mm×3 mm.

The scintillators are made from polystyrene material and covered by a thin reflector which is made from TiO^2. The bars in which one half of them have slits every 50mm cross each other to form the 3-D grid structure of the detector (Fig. A.2). The WAGASCI module can operate with two conditions. The water-in option is the condition in which the detector is fully filled with pure water. In this case, the water mass inside fiducical volume is 188 kg and is equal to 80% of the total target mass. The 20% left is the mass of scintillator. The water-out WAGASCI module doesn't have water inside the detector. The water-out detector has a total mass of 47 kg and it is 100% of the scintillator.

The signal produced by neutrino interaction with the target is collected by Y-11 wave length shifting fibers. The fibers are gathered in groups of 32 fibers each and read-out by 32-channel MPPC array (S13660(ES1)) produced by Hamamatsu company.

Proton module

The INGRID proton module is installed between two WAGASCI modules (see Fig. A.1) on the B2 floor of the T2K near detector hall. It is a fully-active neutrino detector developed by T2K to measure neutrino cross section with a 100% scintillator target. Fig. A.3 right illustrates the schematic view of the proton podule. The total mass of the hydrocarbon target inside the fiducial volume is 302 kg. The module is surrounded by veto planes to prevent wrong sign signals coming from outside detectors. The main part of the detector is assembled from 36 tracking planes, which are made from two types of scintillator strips. The inner region has 16 strips with dimensions of 25mm×13mm×1200mm. The outer region has 16 strips with dimensions of 50mm×10mm×1200mm. The signals in the form of scintillation lights are guided by wave length shifting fibers and read out by MPPCs as for the WAGASCI modules.

Wall-MRD detectors

There are two Wall-MRD modules, which are on the left side and on the right side of the central WAGASCI module. They are used for muon identification and muon momenta measurements. One module is composed of 11 steel plates and 10 plastic scintillator layers, with a total weight of about 8.5 tons. Each steel plate has a size of 1610 mm × 1800 mm × 30 mm. Each scintillator layer consists of eight scintillator bars, in which every bar has a size of 200 mm × 1800 mm × 7 mm (Fig. A.4 right). The wavelength shifting fibers and the MPPC readout are the same as for WAGASCI detectors and the INGRID proton module.

Baby MIND detector

Baby MIND is a downstream muon range detector which also works as a magnet with a minimum magnetic field of 1.5 T (Fig. A.5 (left)). It is a magnetized iron neutrino detector used to measure muon momentum and charge identification. The (anti-)muons produced by neutrino interactions with the WAGASCI targets will be
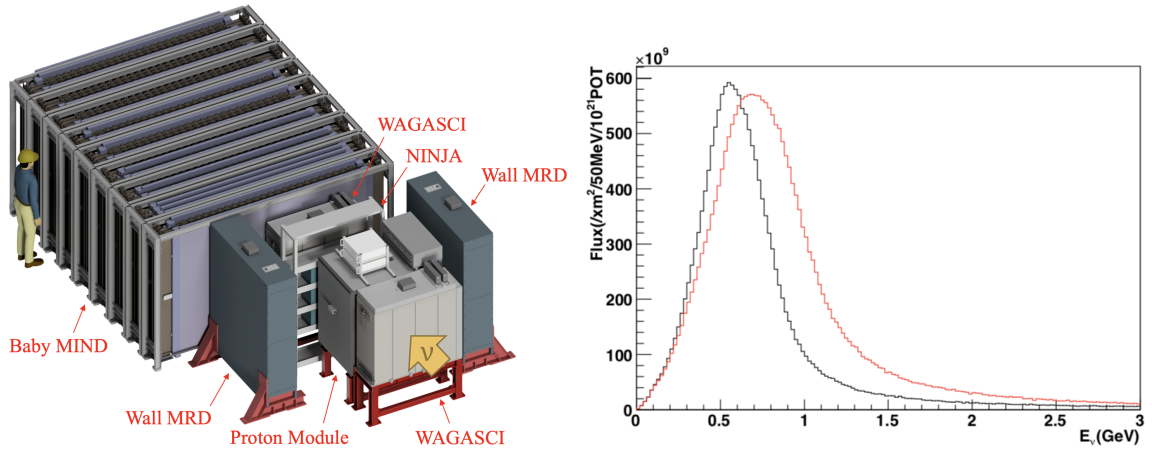
Figure A.1: Left: The configuration of WAGASCI-BabyMIND detectors; Right: The flux at WA-GASCI (1.5^o off-axis, red line) and ND280 (2.5^o off-axis, back line).
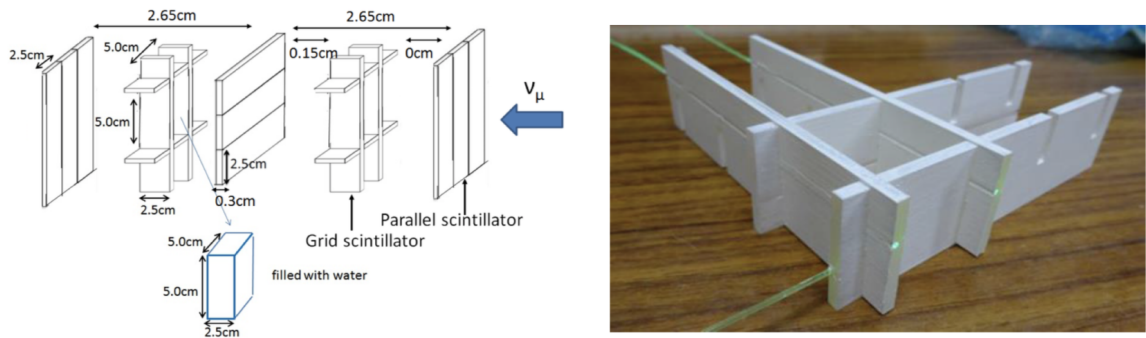

Figure A.2: The 3D grid structure of the plastic scintillator bars.
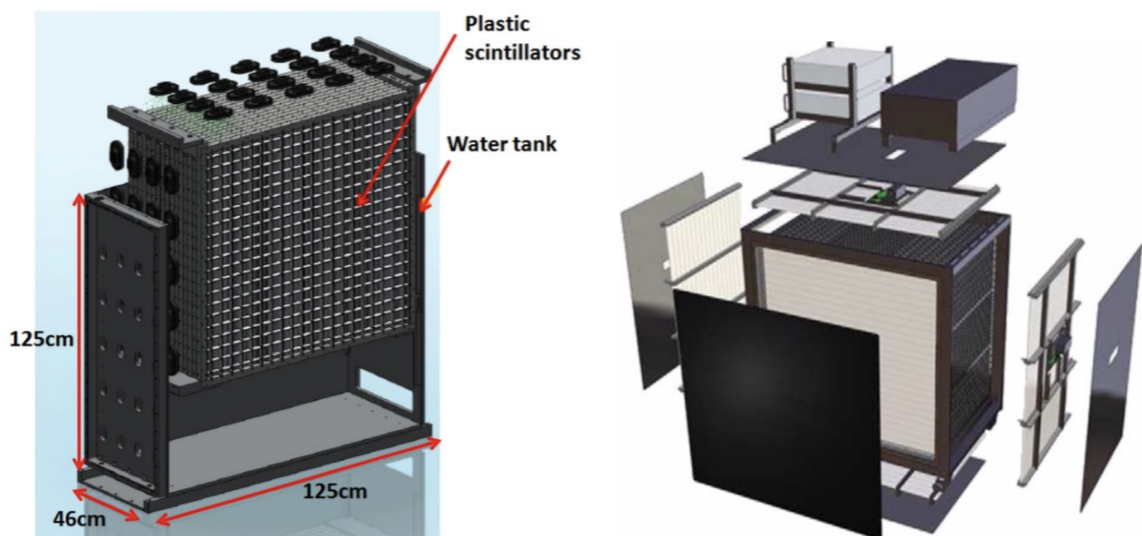

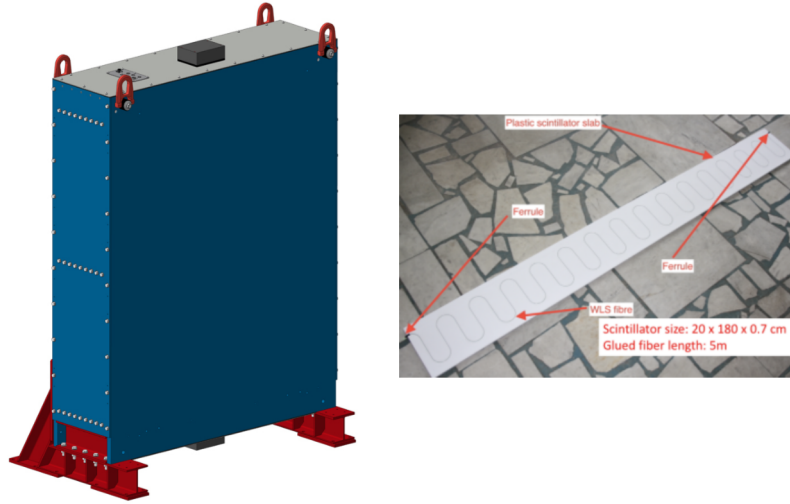Figure A.3: WAGASCI module (left) and Proton Module (right).

Figure A.4: Wall-MRD module (left) and scintillator bar of the module (right).
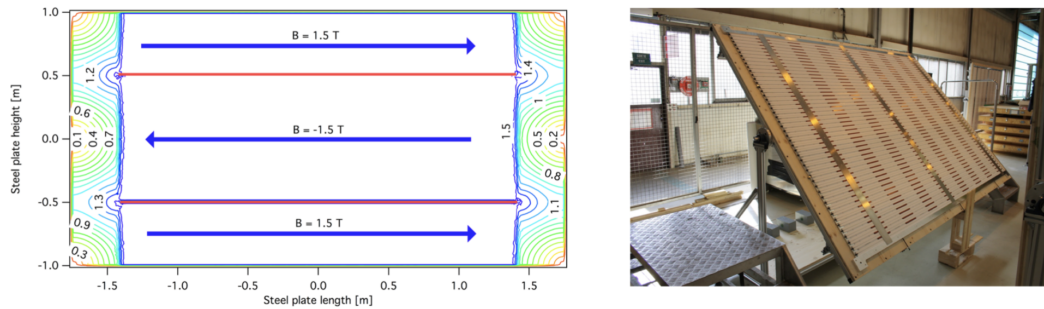

Figure A.5: Magnetic field inside the magnet module (left) and scintillator module (right) of Baby MIND.

bent in curvatures by the magnetic field in opposite directions and therefore can be identified very precisely. The detector consists of 33 magnet modules and 18 scintillator planes. Each magnet module has one 30 mm thick iron plate and weighs 2 tons. The total size of one magnet module is 3500 mm $\times$ 2000 mm $\times$ 50 mm. On one half of the scintillator module there are 95 horizontal bars of size 3000 mm $\times$ 31 mm $\times$ 7.5 mm each and 8 vertical bars of size 1950 mm $\times$ 210 mm $\times$ 7.5 mm each (Fig. A.5 (right)). The wavelength shifting fibers and the MPPC readout are same as for WAGASCI detectors and the INGRID proton module. There are two YASU trakers which have recently been integrated into the upstream part of the Baby MIND module to detect low momentum muons.

A.0.2 Neutrino-nucleus interaction cross section models

The neutrino-nucleus interaction cross section is predicted by NEUT, which is a Monte Carlo simulation package officially used in the T2K experiment to simulate neutrino-nucleus and nucleon interactions in a wide range of energy from MeV to TeV. The neutrino interaction with matter depends on its energy.

Quasi-elastic scatterings

At low energy region (below 1 GeV), quasi-elastic scattering processes dominate:

+ Charged current (CCQE):

$$\nu_l + n \rightarrow l^- + p, \tag{A.1}$$

$$\bar{\nu}_l + p \rightarrow l^+ + n. \tag{A.2}$$

+ Neutral current (NCQE):

$$\nu_l + N \rightarrow \nu_l + N, \tag{A.3}$$

$$\bar{\nu}_l + N \rightarrow \bar{\nu} + N. \tag{A.4}$$

in which l is charged lepton and N is nucleon (proton p or neutron n). In NEUT, CCQE process is modeled by Llewellyn-Smith [113] or Nieves 1p1h [114].

Single meson (π, γ, K, η) production via baryon resonances

At a few GeV, a neutrino is able to excite the nucleus to a baryon resonant state and consequently produce a meson. The dominating process is via $\Delta(1232)$ resonance:

+ CC1π:

$$\nu_l + N \rightarrow l^- + \Delta \rightarrow l^- + N' + \pi, \tag{A.5}$$

$$\bar{\nu}_l + N \rightarrow l^+ + \Delta \rightarrow l^+ + N' + \pi. \tag{A.6}$$

+ NC1π:

$$\nu_l + N \rightarrow \nu_l + \Delta \rightarrow \nu_l + N' + \pi, \tag{A.7}$$

$$\bar{\nu}_l + N \rightarrow \bar{\nu}_l + \Delta \rightarrow \bar{\nu}_l + N' + \pi. \tag{A.8}$$

There are 14 reactions of this kind (6 for CC1π and 8 for NC1π). These processes were considered by Rein-Sehgal [115] with the assumption that lepton mass $m_l = 0$. In this model, the resonance region is up to 2 GeV in terms of the relativistic quark model of Feynman, Kislinger and Ravndal (FKR model [116]). Experimental data indicates that the Rein-Sehgal model overestimates the cross section in the low Q^2 region. Recent Graczyk-Sobczyk model [117] has been used since NEUT 5.3.2. In this model Graczyk and Sobczyk used the same hadronic current as in the Rein-Sehgal model and included additional correction from $m_l \neq 0$ effects by appropriate substituting hadronic weak current matrix elements and adding a new term in the axial current based on partially conserved axial vector current (PCAC) theorem [118] .

Coherent pion productions

In addition to the above resonant processes in this medium energy range, neutrinos can interact coherently with nucleus A, producing pion and leaving the nucleus unchanged in the final state. This is known as *coherent pion production* process

+ CCcoh1π:

$$\nu_l + A \rightarrow l^- + A + \pi^+, \tag{A.9}$$

$$\bar{\nu}_l + A \rightarrow l^+ + A + \pi^-, \tag{A.10}$$

T2K run	Period	Accumulated POT
Run 10	November to December 2019	2.65×10^{20} POT
Run 10	January to February 2020	2.12×10^{20} POT
Run 11	March to April 2021	1.78×10^{20} POT

Table A.1: Summary of data taking at WAGASCI-BabyMIND.

+NCcoh1π:

$$\nu_l + A \to \nu_l + A + \pi^0, \tag{A.11}$$

$$\bar{\nu}_l + A \to \bar{\nu}_l + A + \pi^0. \tag{A.12}$$

There are some models describing these processes, including PCAC based models and microscopic models. In this essay, we will present in detail the PCAC based models of Rein-Sehgal [119], [120] and Berger-Sehgal [121], which describe the early high energy data connection between coherent reaction and π elastic scattering with target nucleus. These models, however, overestimate at low energy, so they need to be implemented with corrections to fit the data. The Rein-Sehgal model assumes the collision is forward-scattering (small scattering angle of out-going lepton) and takes an approximation of $m_l = 0$ and $Q^2 = 0$. The Berger-Sehgal model is an updated version of Rein-Sehgal model in order to valid for all Q^2 values. The total cross section predicted by the Berger-Sehgal model is reduced by a factor of 2 compared to the Rein-Sehgal model. The Berger-Sehgal model is implemented in NEUT since the version v5.4.0.

Deep inelastic scatterings

At a high energy of above 5GeV, the interaction is dominated by deep inelastic scattering (DIS) processes. In these processes, neutrino has enough energy to enter inside nucleus, interacts with quarks and produces hadrons in the final states:

+ CCDIS:

$$\nu_l + N \to l^- + N' + \text{hadrons},$$
$$\bar{\nu}_l + N \to l^+ + N' + \text{hadrons}. \tag{A.13}$$

+ NCDIS:

$$\nu_l + N \to \nu_l + N' + \text{hadrons},$$
$$\bar{\nu}_l + N \to \bar{\nu}_l + N' + \text{hadrons}. \tag{A.14}$$

A.0.3 Data set

WAGASCI-BabyMIND has started taking date since 2019. It collected 6.55×10^{20} POT in total. The accumulated data is summarized in Table A.1

A.0.4 Monte Carlo simulation

The simulation process is similar to INGRID. First, neutrino beam flux at B2

floor is simulated by JNUBEAM. Then the interactions between neutrinos and target materials are described by NEUT. Finally, a GEANT4-based package will simulate the detector response.

In our study we focus on the analysis of CC1π interaction which contains one pion in the final state. The interaction can be CC1π resonance or CC1π coherent (Eq.(A.5) and Eq.(A.9)). We can see that a CC1π event has at least two tracks, including muon track and the pion track. An event is defined as **signal** if vertex of the interaction is in a target detector (called **vertex detector**) and the vertex has more than two tracks, in which at least one track matches with other modules. There are three vertex detectors, including upstream wagasci (UWG), downstream wagasci (DWG), and Proton Module (PM), and three muon range detectors (called Wall-MRD) including North-MRD, South-MRD, and BabyMIND. In this study, we generated 984 MC files of muon neutrino and antineutrino beams in which each MC file is equivalent to 10^{21} POT. The MC fake data is then normalized to 5×10^{20} POT. The event selection follows similar steps as for the INGRID study in the section 2.2:

1. Time clustering: The signal is collected by scintillators, transmitted by WLS (wavelength shifting) fibers and detected by MPPCs. The signal is detected in terms of ADC counts or number of PE. Channels with ADC signals larger than 2.5 PE are defined as **hits**. A cluster is formed if there are more than three hits in which the difference between any two adjacent hits is less than 100 ns.

2. Two dimensional track reconstruction: The tracks in the XZ and YZ planes (see Fig. A.6 for coordinate system definition) are reconstructed by using the "cellular automaton" algorithm, which is described in Fig. 2.9 and Section 2.2.2.

3. Three-dimensional track reconstruction: The tracks are matched from vertex detector to BabyMIND or Wall-MRDs. The algorithm looks for clusters in either BabyMIND or WallMRD, then matches them with clusters in vertex detectors under matching conditions. Matching conditions are mainly divided into two parts: the angle between two clusters (see Table A.2), and the position difference between a cluster in an upstream detector and a cluster in a downstream detector (see Table A.3). If an event has clusters that satisfy matching conditions, it will proceed with three-dimensional track matching. The algorithm ensures that there is at least one pair of track matching in both views. It will check if both upstream edge position differences and downstream edge position differences satisfy a three-dimensional matching condition shown in Table A.4.

4. Vertexing: The vertex in the target detector will be reconstructed after three-dimensional track matching is finished. The positions of vertexes X and Y are taken from the start positions of the three-dimensional matching track, while the position of vertex Z is the minimum value of matching tracks in both views. Assume ΔZ and ΔXY respectively are differences in positions of Z vertex and X/Y vertexes

Upstream detector	Downstream detector	View	Threshold angle (°)
Vertex detector	BabyMIND	XZ	30
Vertex detector	BabyMIND	YZ	25
Vertex detector	WallMRD	XZ	25
Vertex detector	Vertex detector	XZ and YZ	25

Table A.2:   Threshold angles for matching tracks between detectors.

Upstream detector	Downstream detector	View	Threshold distance (mm)
UWG	BabyMIND	XZ	300
PM and DWG	BabyMIND	XZ	300
UWG	BabyMIND	YZ	300
PM and DWG	BabyMIND	YZ	250
Vertex detector	WallMRD	XZ	500
UWG	PM	XZ and YZ	200
UWG	DWG	XZ and YZ	300
PM	DWG	XZ and YZ	200

Table A.3:   Threshold distancs for matching tracks between detectors.

Detector	Threshold distance (mm)
Upstream edge vertex detector	150
Downstream edge vertex detector	200 (WallMRD) and 350 (BabyMIND)

Table A.4:   Three dimensional track matching conditions.

between clusters, the conditions for them to have the same vertex are

$$\Delta Z \leq 80 \ mm, \quad \Delta XY \leq 80 \ mm. \tag{A.15}$$

5. Fiducial volume cut: The fiducial volume cut is applied to remove backgrounds from outside detectors. The fiducial volume of a WAGASCI module is a cubic volume dimension $400mm \times 400mm \times 150mm$. For Proton Module the fiducial volume is of dimension $500mm \times 500mm \times 300mm$.

6. Charge identification and muon momentum determination: The charge of a particle is defined by Baby MIND. The particle will be bent upward or downward depending on its electric charge when it flies into the magnetic field region of Baby MIND. Muon produced by neutrino interaction with target nuclei will travel to Wall-MRD modules or Baby MIND. To select muon tracks and reject backgrounds from neutral current events, the longest track is required to penetrate more than one and five iron plates in Wall-MRD modules and Baby MIND, respectively. The muon momentum is then determined by requiring the longest track to stop in Wall-MRD modules or Baby MIND or penetrate all iron plates. The materials that the muon may penetrate are iron, scintillator, and water with corresponding densitites: $\rho = 7.874 \ g/cm^3$, $\rho = 1.032 \ g/cm^3$, and $\rho = 1.002 \ g/cm^3$. The energy loss is normalized to iron by the density ratio of iron to scintillator and water. The reconstructed muon momentum is calculated using the relationship between the mean energy loss rate in iron and muon momentum as shown in Fig. A.7.

In the following plots, the vertex detector is Upstream WAGASCI. Fig. A.8 displays the matching tracks with sub-detectors which vertexes are in the fiducial volume. The left plots correspond to track distribution versus track angle, while the right plots are versus track momentum. We can see that the track matching with Proton Module is less than 80°, while matching with Downstream WAGASCI or BabyMIND is less than 40°. The angles of track matching with Wall-MRD are mostly between 20° and 80°. For momentum distribution, we can see the energy peaks at Proton Module, Downstream WAGASCI, and BabyMIND are around 1 GeV, while at Wall-MRD they are around 0.5 GeV.

A.0.5 Conclusion

The section has provided a description of the WAGASCI BabyMIND experiment, neutrino cross section models, and how the cross section is measured at WAGASCI BabyMIND. The preliminary result is reported with 5×10^{20} POT, which is equivalent to the data taken in T2K run 10 with 4.77×10^{20} POT.
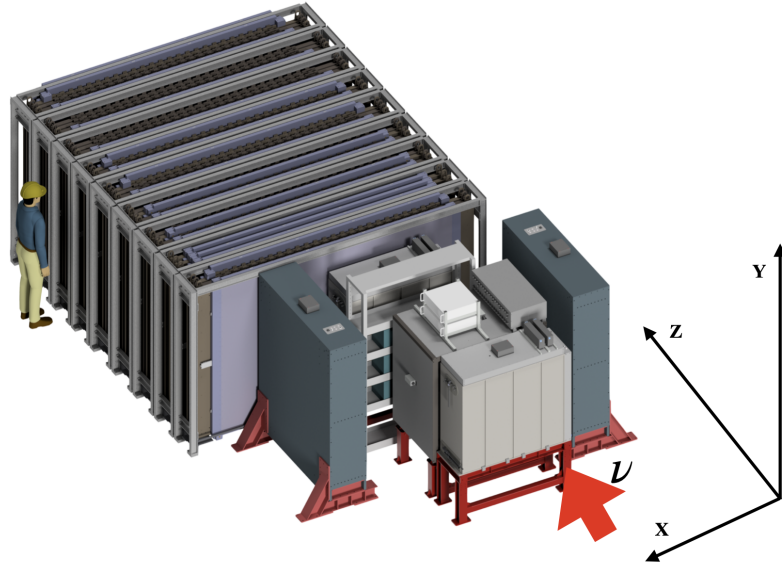
x

Figure A.6: Definition of XYZ coordinate system at WAGASCI-BabyMIND experiment. Z axis is along the neutrino beam, Y axis is perpendicular to the ground and pointed upward, X axis is perpendicular to both Y and Z axis.
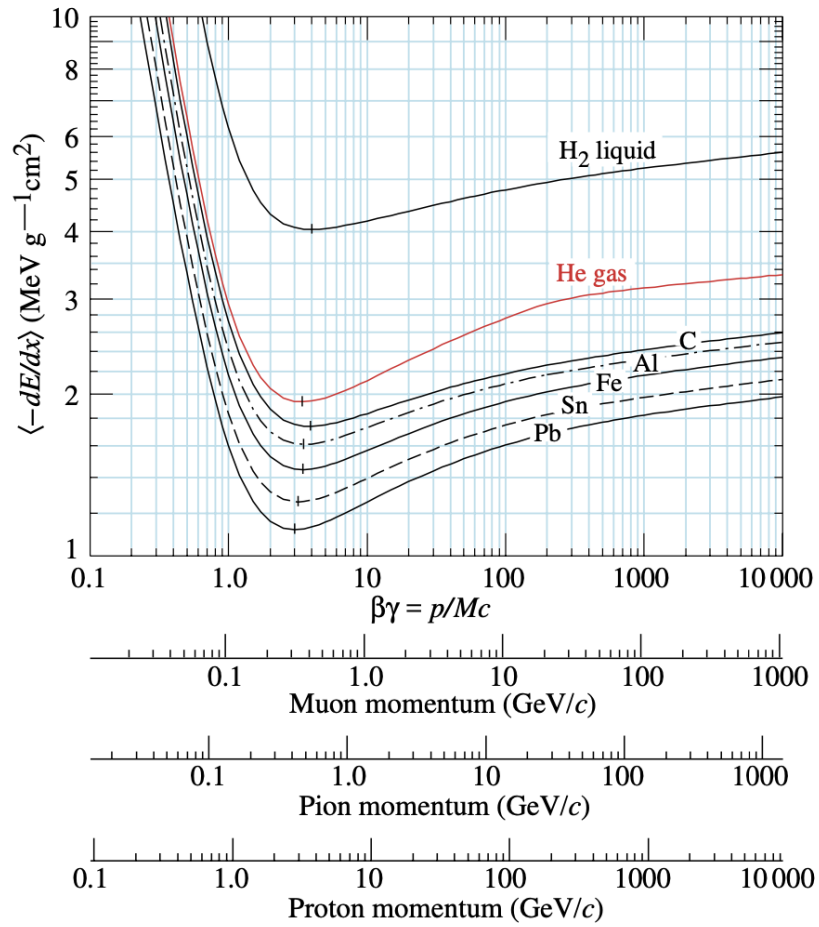

Figure A.7: Mean energy loss rate in liquid (bubble chamber) hydrogen, gaseous helium, carbon, aluminum, iron, tin, and lead. The plot is taken from Ref. [12].
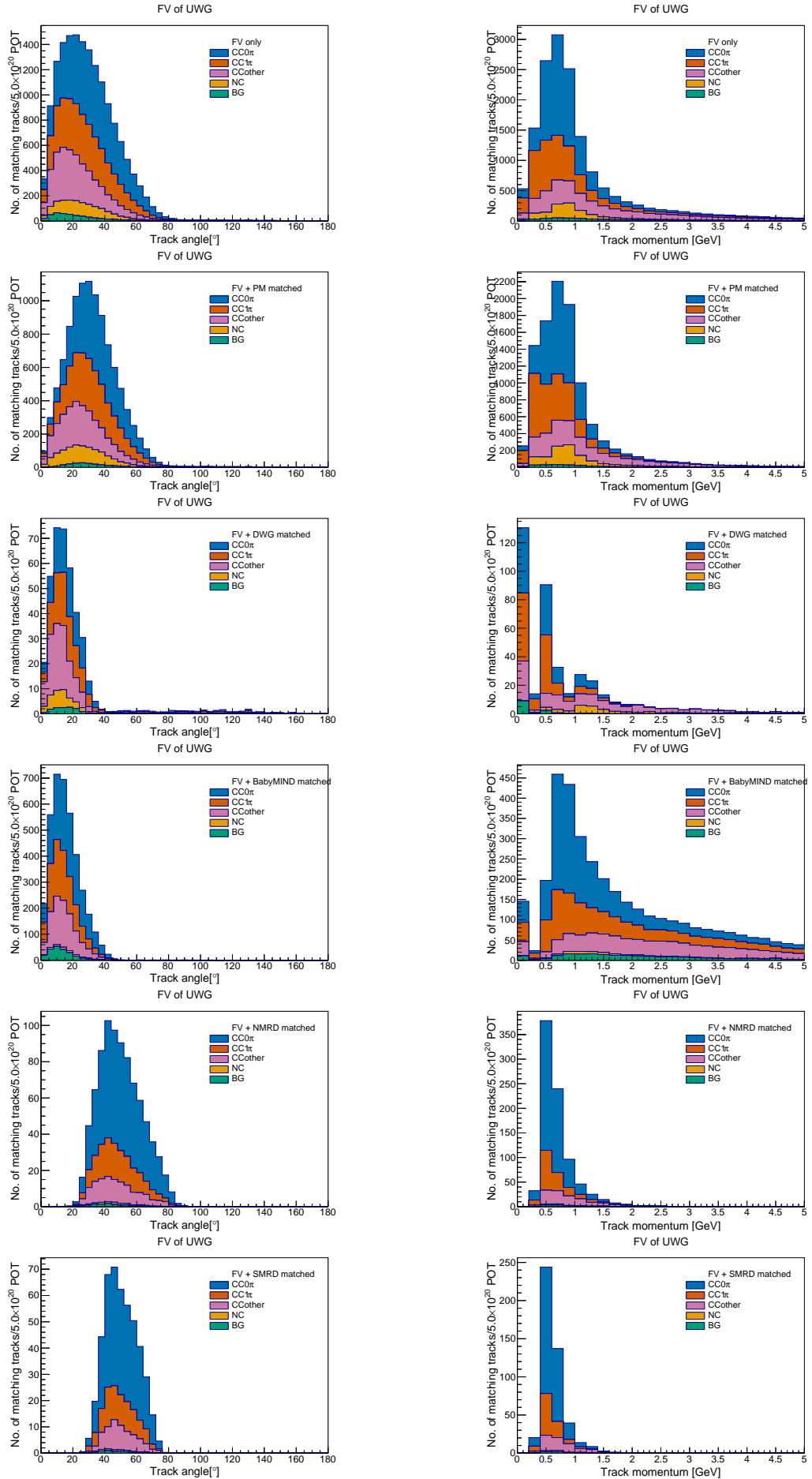
Figure A.8: Matching tracks with sub-detectors which vertexes are in the fiducial volume of upstream WAGASCI, left: versus track angle, right: versus track momentum.